Evaluating the E3SMv2-MPAS <u>Oo</u>cean-<u>Ssea <u>Fi</u>ce <u>Cc</u>oupled <u>Uu</u>nstructured <u>Mm</u>odel in the Arctic: Atlantification <u>Pp</u>rocesses and <u>Ssystematic Bbiases</u></u>

Xinyuan Lv¹, Huizan Wang¹, Yu Cao¹, Kaijun Ren¹, Yangjun Wang² and Hao Ding¹

¹College of Meteorology and Oceanology, National University of Defense Technology, Changsha, 410073, China ²College of Advanced Interdisciplinary Studies, National University of Defense Technology, Nanjing, 211101, China Correspondence to: Huizan Wang (wanghuizan@126.com) and Kaijun Ren (renkaijun@nudt.edu.cn)

Abstract. Advancing high-resolution Arctic ocean-sea ice modeling is critical for understanding polar amplification and improving climate projections but faces challenges from computational limits and cross-scale interactions. The simulation capabilities of the ocean-sea ice coupled model (E3SMv2-MPAS) from the Energy Exascale Earth System Model (E3SM) 2.1 for the Arctic-sea ocean-sea ice system are systematically evaluated using multi-source observational data-and-model outputs. The model employs aA latitudinally varying mesh, with resolution increasing from (60 km in the Southern Hemisphere to 10 km in the Arctic.) This design balances computational efficiency with the accurate integration of while integrating-low-latitude oceanic influences, while the Uunstructured meshes also enhances the geometric representation of Arctic straits, coupled with a suitable mesoscale eddy transport parameterization to establish Together, these features form a simulation framework capable of resolving processes from seasonal to decadal timescalesa multi-scale simulation framework. Numerical results demonstrate E3SMv2-MPAS's superior Arctic simulation performance: (1) Accurate reproduction of spatial heterogeneity in sea ice concentration, thickness, and sea surface temperature, including their 1995– 2020 trend patterns; (2) Faithful reproduction of both the freshwater content and transports through key Arctic gateways; (32) Successful reconstruction of three-dimensional thermohaline structures within the Atlantic Water layer, capturing Atlantic Water's decadal warming trends and accelerated Atlantification processes ____ specifically mid-layer shoaling, heat content amplification, and reduced heat transfer lag times in the Eurasian Basin. Persistent systematic biases are identified: 0.5-1 m sea ice thickness overestimation in the Canadian Basin compared to ICESat observations; Coordinated sea surface temperature/salinity underestimation and sea ice concentration overestimation in the Greenland and Barents Seas; Atlantic Water core temperature overestimation; Regional asymmetries in decadal thermohaline field evolution. These systematic biases may be attributed to three principal sources; inadequate representation of eddy dynamics, limitations in mixing parameterizations, and insufficient resolution of cross-scale interactions in key gateways (e.g., Fram Strait).

1 Introduction

30

35

45

60

The Arctic region has emerged as one of the most rapidly transforming areacomponents of the Earth system under contemporary climate change (Calvin et al., 2023). However, persistent gaps in oceanic observational networks, particularly the lack of systematic full-depth and pan-strait measurements across key Arctic gateways, have significantly constrained our understanding of Arctic oceanic transport dynamics. To address these observational limitations, numerical modeling has become an indispensable tool (Wang et al., 2023). Of particular scientific significance is the thermohaline transport through Fram Strait – the principal conduit for Atlantic Water (AW) intrusion into the Arctic basins (Fu et al., 2023; Karami et al., 2021; Long et al., 2024). Recent studies highlight the necessity to quantify both the spatiotemporal evolution of AW-derived heat distribution across Arctic marginal seas and the relative contributions of different vertical heat flux mechanisms (Carmack et al., 2015; Polyakov et al., 2020b). State-of-the-art global climate models (GCMs) provide critical insights into the evolving climate system under sustained global warming scenarios, enabling the investigation of multi-sphere interactions and their associated feedback mechanisms (Dörr et al., 2021; Hinrichs et al., 2021; Rieke et al., 2023; Shu et al., 2022) (Duarte et al., 2020; Hinrichs et al., 2021; Liang and Losch, 2018a; Tian et al., 2022; Wassmann et al., 2015).

While climate models remain indispensable tools for deciphering Earth system dynamics (Landrum and Holland, 2020), their representation of Arctic processes exhibits persistent uncertainties that challenge predictive capabilities (Pan et al.,

2023). Systematic biases plague the simulation of critical Arctic phenomena, including amplified warming rates, sea ice retreat patterns, and AW layer evolution (Heuzé et al., 2023; Khosravi et al., 2022; Muilwijk et al., 2023; Shu et al., 2019). These limitations persist across successive model generations, as evidenced by Coupled Model Intercomparison Project Phase 5 (CMIP5) and Phase 6 (CMIP6) revealing substantial errors in Arctic three-dimensional thermohaline structure reproduction (Khosravi et al., 2022; Shu et al., 2019). There are mainly four common biases of contemporary models in the Arctic include: (1) Overestimated AW layer thickness and depth. This systematic vertical structure misrepresentation persists across model generations, from early Arctic Ocean Model Intercomparison Project (AOMIP) simulations (Holloway et al., 2007) through the Coordinated Ocean-ice Reference Experiments, phase II (CORE-II; Ilicak et al. (2016)), toand the most widely used CMIP5/CMIP6 ensembles (Heuzé et al., 2023; Khosravi et al., 2022; Shu et al., 2019). Among 41 CMIP5 models evaluated by Shu et al. (2019), 22% failed basic AW identification criteria, while the remaining 32-model mean overestimated AW layer vertical extent compared to observational benchmarks. CMIP6 shows limited improvement, with multi-model mean AW upper boundaries erroneously positioned at ~400 m depth in the Nansen Basin – deeper than observed values – and excessive thickness extending to seafloor regions in some regions (Khosravi et al., 2022). (2) Cold bias in AW core temperatures. The Alfred Wegener Institute coupled climate model (AWI-CM1) exhibits thermal underestimation at 200–600m depths in Eurasian Basin simulations (Hinrichs et al., 2021), consistent with CMIP6's 0.4°C cold bias relative to hydrographic climatologies (Heuzé et al., 2023). (3) Failure to capture AW warming trends. CMIP5 models collectively underestimate observed decadal temperature variability, with no model replicating post-2000 acceleration in AW warming (Shu et al., 2019). (4) Underestimated "Atlantification" (referring to the Arctic Ocean water

properties becoming increasingly akin to the warmer and saltier <u>AWAtlantic water</u>). While models project gradual boreal water encroachment in the Barents Sea by 2100 (Wassmann et al., 2015), observational <u>analyzesanalyses</u> suggest this regime shifts is likely to occur at a faster pace (Lind et al., 2018). Discrepancies extend to sea ice thermodynamics, where Seasonal Forecast System 5 (SEAS5) simulations yield only 10–20 cm winter ice production decline (Polyakov et al., 2022), versus 78–93 cm observed losses (Polyakov et al., 2020b).

There are numerous and complex reasons that lead to the common deviations in models when simulating the AW. These challenges can be categorized into four primary domains: (1) Insufficient horizontal resolution (>50 km in most CMIP6 models) fails to resolve critical boundary currents and mesoscale eddies (Hinrichs et al., 2021); (2) Unrealistic Atlantic-Arctic exchange through Fram Strait (Hinrichs et al., 2021); (3) Parameterization deficiencies, including the incorrect representation of horizontal advection and vertical mixing (Lind et al., 2018); (4) Imperfect knowledge of ocean-sea ice-atmosphere triadic feedbacks, especially during winter convection events, hampers accurate simulation of AW ventilation processes (Heuzé et al., 2023). To advance model fidelity and reduce uncertainty sources, comprehensive investigations into systematic model biases are imperative (Hinrichs et al., 2021; Pan et al., 2023).

70

80

90

Current numerical simulations for polar regions are primarily based on structured grid models. However, the inherent limitations of structured grids, particularly the singularity at the North Pole and meridional convergence artifacts, fundamentally constrain their capacity to represent Arctic-specific physical processes (Liu et al., 2016). These geometric constraints not only distort parameterization schemes but also introduce systematic biases in both regional and decadal-scale simulations. While global high-resolution configurations could theoretically mitigate such issues, their prohibitive computational costs render them impractical for climate-scale applications (Golaz et al., 2019). This technological impasse has driven the development of two complementary approaches: (1) Nested grid systems: Though offering advantages in spatial temporal discretization flexibility and geometric simplification, their implementation introduces nontrivial challenges in mass conservation, interface coupling fidelity, and numerical noise suppression (Hoch et al., 2020). (2) Unstructured mesh: By enabling localized resolution enhancement in dynamically critical zones while maintaining coarse resolutions elsewhere, these meshes eliminate the need for explicit nesting procedures (Scholz et al., 2019). Their continuous spatial adaptability allows direct resolution of sub-mesoscale processes without compromising computational efficiency (Wang et al., 2018).

The application of variable-resolution models with a global unstructured meshes offers distinct advantages for Arctic Ocean studies. By employing high-resolution meshes over the Arctic region, these configurations enable accurate simulation of energy exchange processes across narrow critical channels (e.g., Fram Strait, Bering Strait, Barents Sea Opening and Davis Strait). Coarser resolutions in other domains maintain computational efficiency while preserving connectivity between the Arctic and extratropical regions (Wang et al., 2018). Among global implementations, two widely adopted models are the Finite-Volume Coastal Ocean Model (FVCOM; Chen et al. (2016)) and the Finite-Element Sea ice-Ocean circulation Model (FESOM; Danilov et al. (2017)). In Arctic studies, FVCOM predominantly operates as a regional model, as evidenced by its frequent implementation in localized domains (e.g., Zhang et al. (2016)). This regional focus aligns with FVCOM's original

design paradigm prioritizing coastal and shelf-sea dynamics through its finite-volume discretization scheme. In contrast, FESOM has been predominantly implemented as a global model in Arctic studies, where its implementation has demonstrated unprecedented skill in simulating Arctic intermediate water dynamics (Danilov et al., 2017; Wang et al., 2018; Wekerle et al., 2013). Notably, Wang et al. (2018) established that FESOM's (a relatively low resolution, ~24 km in the Arctic) outperforms a set of the then state-of-the-art structured-grid models evaluated by Ilıcak et al. (2016), particularly in correcting systematic AW core biases.

As a more recent modeling framework relative to FESOM and FVCOM, the Model for Prediction Across Scales (MPAS) remains in the nascent phase of Arctic performance evaluation (Huo et al., 2024; Ringler et al., 2013), particularly regarding its capacity to simulate intermediate water masses and Atlantification processes. The Energy Exascale Earth System Model (E3SM), evolved from the Community Earth System Model (CESM), incorporates MPAS-Ocean and MPAS-Seaice as its ocean and sea ice components. Initial assessments using E3SMv1's ocean-sea ice coupled configuration (60to10 km variable resolution) demonstrate promising skill in reproducing pan-Arctic freshwater budgets, gateway current exchanges, and vertical hydrographic profiles (Veneziani et al., 2022). Persistent errors in sea ice thickness (SIT) distribution and upper 100 m stratification emerge across resolutions, suggesting common structural models deficiencies rather than discretization artifacts. However, their diagnostic lack the rigorous validation metrics employed by Wang et al. (2018) for FESOM's AW representation. Existing assessments predominantly rely on pan-Arctic-basin-averaged diagnostics, obscuring critical vertical and regional heterogeneities in intermediate AW layer dynamics (Veneziani et al., 2022).

This study presents a tripartite evaluation framework for the coupled system of MPAS-Ocean and MPAS-Seaice in E3SM version 2 (E3SMv2-MPAS), which compares it with the observational datasets and reanalysis products and high resolution model outputs from CMIP6 and the Ocean Model Intercomparison Project Phase 2 (OMIP2) to systematically assess MPAS's capacity in simulating key Arctic processes to address persistent Arctic AW biases. In addition, we conduct a comprehensive assessment of Arctic sea ice dynamics, surface layer hydrographic properties, and three-dimensional thermohaline profile evolution (particular emphasis on the AW layer), as well as freshwater content and key gateway transports, with particular emphasis on their respective—The assessment highlights the model's strengths, identifies its limitations, and discusses potential sources of uncertainty. Innovatively, this work implements a multi-layer connectivity analysis examining cross-layer interactions between surface (10 m) and intermediate (400 m) depths.

The subsequent sections are structured as follows: Section 2 provides comprehensive documentation of the E3SMv2-MPAS configuration and validation datasets. Section 3 and Section 4 conduct rigorous multi-faceted analyzesanalyses of Arctic-specific simulations, employing both domain-wide diagnostics and sub-regional decomposition approaches. These sections also discuss remaining challenges in polar ocean-sea ice modeling, and proposes targeted development pathways for next-generation Earth system models. Section 5 discusses the potential advantages of higher resolution and unstructured meshes, summarizes simulated biases and their possible sources, and identifies limitations in our model design and configuration. Finally, Section 6 synthesizes the key findings and outlines broader implications. The concluding Section 5 synthesizes key findings.

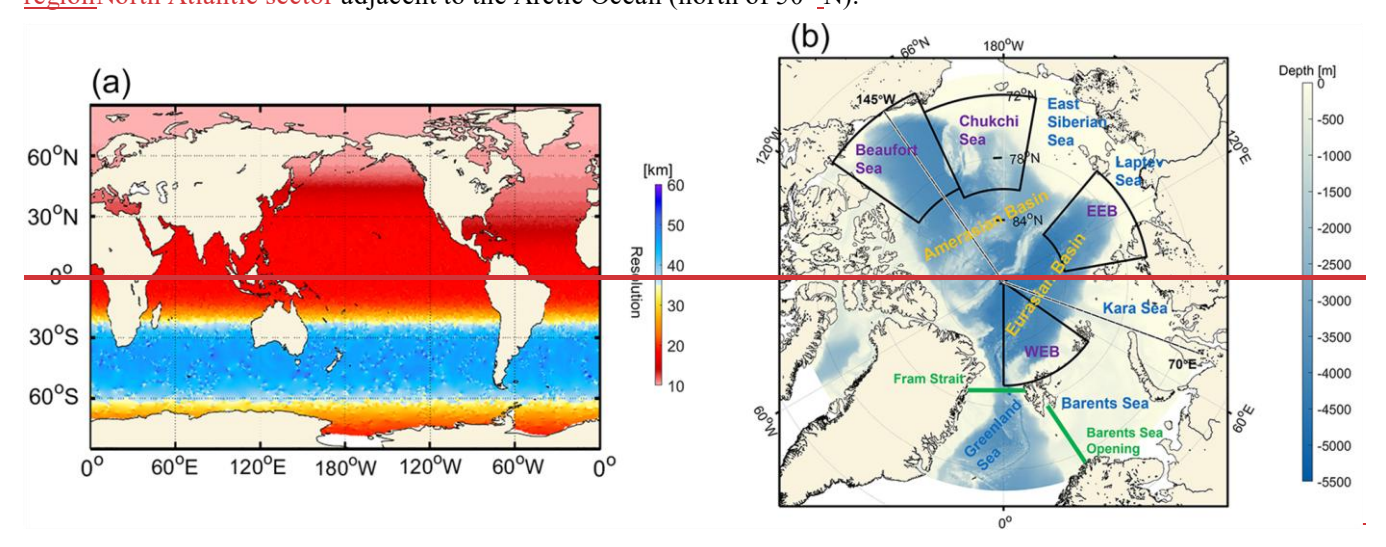
2 Model Configurations and Ddata

130 2.1 Model Configuration

135

140

Veneziani et al. (2022) demonstrated that refining mesh resolution from 10 km to 6 km triples computational costs without yielding significant improvements in simulation fidelity. Their findings suggest that resolving the local Rossby radius of deformation across most Arctic regions necessitates resolutions ≤3 km — a requirement currently constrained by prohibitive computational demands. The model configuration in this paper is described as follows. To address the trade-off between high-resolution requirements and computational constraints, our study employs a variable-resolution unstructured mesh featuring a meridional transition from 60 km resolution in the Southern Hemisphere to 10 km in the Arctic domain (hereafter 60to10 km, same as Veneziani et al. (2022); Fig. 1a). This adaptive meshing approach optimizes computational efficiency while resolving critical processes: (1) Antarctic coastal regions (80°_S-90°_S) maintain a 25 km resolution to capture fine-scale dynamics; (2) the The North Atlantic sector is strategically refined demonstrates strategically prioritized mesh refinement, transitioning from 20 km to 10 km resolution earlier than theits Pacific counterpart to guarantee at least 15 km resolution in the Gulf Stream extension region (~40°_N; Veneziani et al. (2022)); (3) the The North Pacific sector configuration maintains computational efficiency while achieving approximately 10 km resolution in its the subpolar region North Atlantic sector adjacent to the Arctic Ocean (north of 50° N).



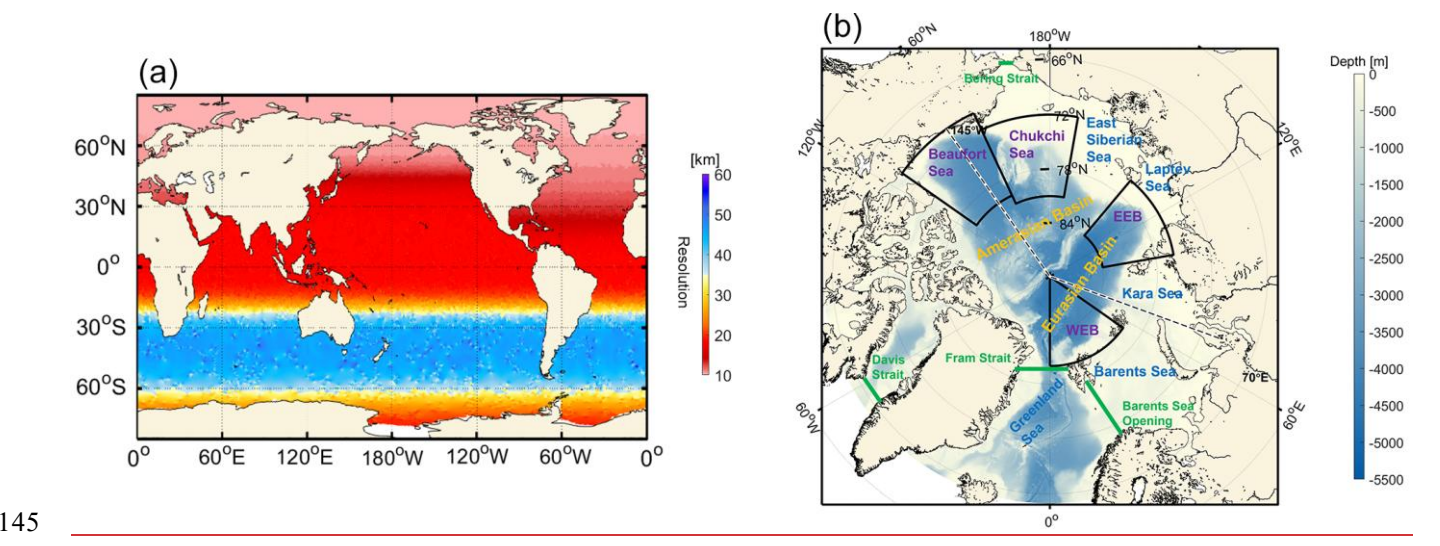


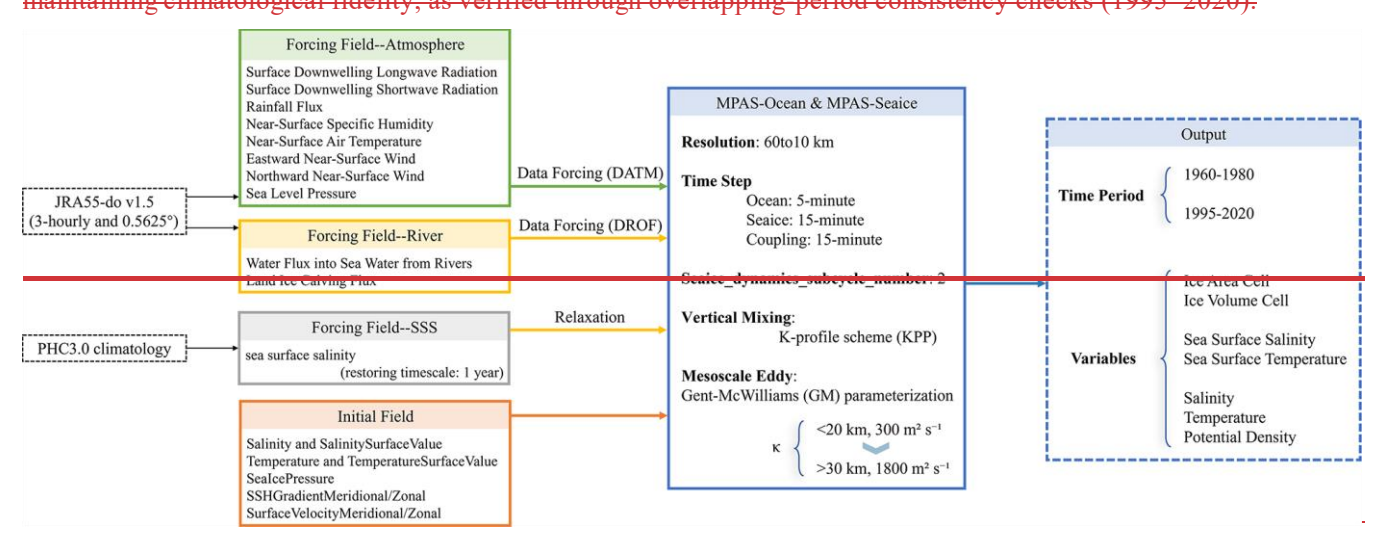
Figure 1. (a) Geographical distribution of grid cell size (km) of the E3SMv2-MPAS framework. (b) **B**bathymetry from the ETOPO 2022 and key basins/straits north of 60° N. EEB and WEB refer to the eastern and the western Eurasian Basin respectively. The black dashed transect along 70° E and 145° W (crossing the North Pole) denotes the location of the transect shown in Fig. 14.

155

160

Numerical stability wasis achieved through a 5-minute baroclinic time step for ocean dynamics. For sea ice, we employed a 15-minute dynamic time step and a 30-minute thermodynamic time step (a 2:1 ratio) and a 2:1 ratio of sea ice thermodynamic to dynamic time stepping. MPAS-Ocean adopts finite volume discretization of primitive governing equations within a staggered C-grid framework, incorporating hydrostatic, incompressible, and Boussinesq approximation assumptions (with a z-star vertical grid) (Golaz et al., 2019). Vertical mixing processes were are parameterized using the Kprofile scheme (KPP; Large et al. (1994)). For mesoscale eddy representation, similarly to what was done in Veneziani et al. (2022), we implemented a spatially varying Gent-McWilliams (GM) parameterization, incorporating both bolus advection and Redi isopycnal diffusion components (Gent and Mcwilliams, 1990). The eddy diffusivity coefficient (κ) exhibits was given a latitudinal dependence: 300 m² s⁻¹⁻¹ in high-resolution Arctic regions (<20 km grid spacing) to maintain moderate mixing intensity, transitioning linearly to 1800 m² s⁻¹⁻¹ in low-resolution zones (>30 km grid spacing) to compensate for unresolved eddy fluxes (Fig. 2). MPAS-Seaice builds upon the core numerical and physical framework of the Los Alamos Sea Ice Model (CICE). The dynamics are governed by the elastic-viscous-plastic (EVP) rheology, with the internal ice stress divergence operator adapted for MPAS's unstructured polygonal mesh (Turner et al., 2022). Sea ice and tracer transport are handled by an incremental remapping scheme (Lipscomb and Ringler, 2005), adapted for polygonal cells. The thermodynamics and vertical column physics remain consistent with CICE (Turner et al., 2022). The configuration includes the "mushy layer" thermodynamics for vertical heat transfer, the delta-Eddington shortwave radiation scheme, a level-ice melt pond parameterization, ice thickness distribution mechanics, and transport in thickness space (Petersen et al., 2019). The specific configurations of MPAS-Ocean and MPAS-Seaice within the E3SMv2, including their coupling mechanisms, have been comprehensively documented in Turner et al. (2022), and Golaz et al. (2022) and Huo et al. (2024).

In addition to the ocean and sea ice components, the atmospheric and river modules in E3SMv2-MPAS (see Fig. 2 for specific variables used) are—were forced by the JRA55-do (v1.5; Tsujino et al. (2018)) from the Japan Meteorological Agency (JMA). This dataset has high spatiotemporal resolution (3-hourly temporal and 0.5625° spatial resolution) and spans the period from 1958 to 2020. Sea surface salinity (SSS) is—was relaxed toward Polar science center Hydrographic Climatology (PHC) 3.0 climatology (Steele et al., 2001) with an annual restoring timescale. The initial conditions for the MPAS Ocean and MPAS Seaice components (including salinity, temperature, sea surface height gradients, and surface velocities) were sourced from the E3SMv2 predefined benchmark case files (specifically ocean.ARRM60to10.180715.nc). These fields were generated through a prior forward simulation of the MPAS Ocean model. This initial state is intrinsically consistent with E3SM's dynamical core, having undergone a spin-up process within the MPAS Ocean framework prior to being archived as a standard case. Following the configuration of forcing and initial conditions (see Fig. 2 for parameter details), E3SMv2-MPAS achieves rapid surface state alignment with observational benchmarks during initial integration (surface temperature anomalies <5% within the first month). The simulation periods explicitly configured in this study are 1960-1980 and 1995-2020. The exclusion of intermediate years (1981-1994) preserves computational resources while maintaining climatological fidelity, as verified through overlapping period consistency checks (1995-2020).



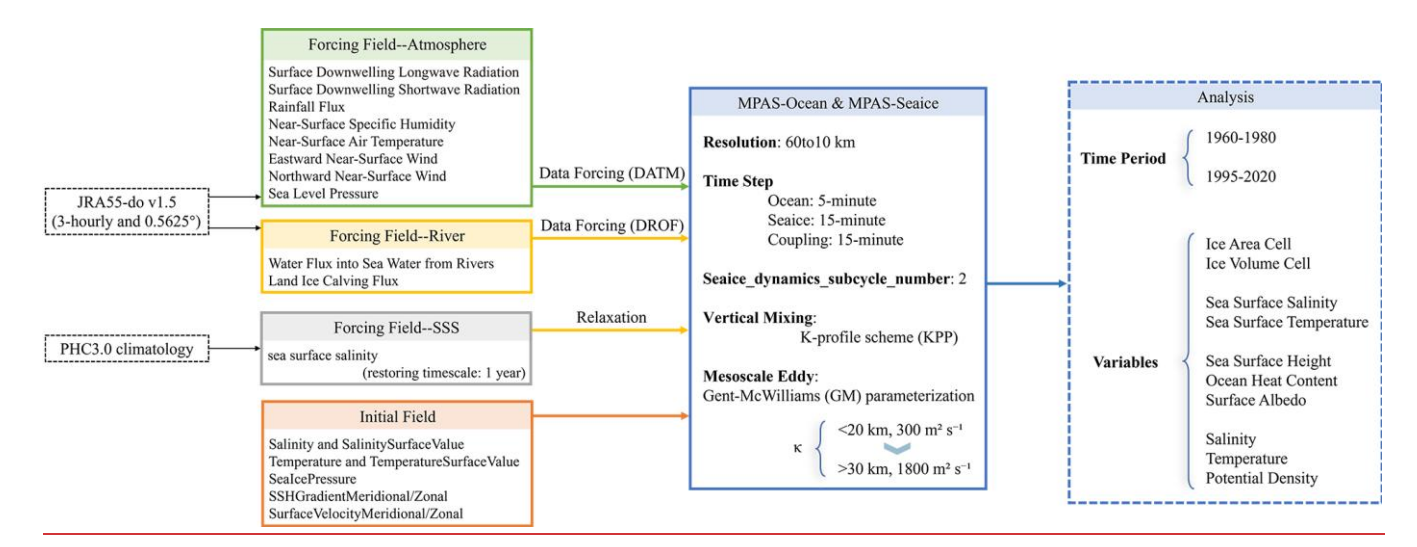


Figure 2. Configuration details for E3SMv2-MPAS: forcing/initial conditions, runtime settings, and output fields.

195

200

Given the prohibitive computational cost of a continuous high-resolution simulation from 1958 to 2020, we adopted a strategic two-period integration scheme to prioritize computational resources for our core analysis period (1995–2020). The model's climatological fidelity during this satellite era is verified using multi-source observational data, ensuring a reliable assessment of both sea ice and ocean variability.

The MPAS-Ocean component was initialized from a pre-processed state (ocean.ARRM60to10.180715.nc). This state was derived from a prior short-term (5-day) adjustment run of the standalone ocean model, which itself started from a state of rest with three-dimensional temperature and salinity fields prescribed from the PHC. Consequently, this initial condition provided a dynamically adjusted and physically consistent starting point for our coupled simulation, mitigating the initial shock that would otherwise occur from a purely cold start. In contrast, the MPAS-Seaice component was initialized from an idealized, uniform ice cover. A 1-meter thick ice layer with 100% concentration was prescribed on all ocean grid points between 60° S and 70° N, with zero initial snow depth and stationary ice velocity. This simple state allowed the sea ice cover to evolve self-consistently in response to the model's atmospheric forcing and ocean coupling from the beginning of the simulation. Following this spin-up phase, the full interannual JRA55 forcing was applied from 1958 to 1981.

To begin the simulation for our main analysis period (1995–2020), we used the model state from December 1981 as the initial conditions for January 1995. This 13-year gap (1982–1994) was a strategic choice to conserve computational resources while ensuring physical consistency in the key variables of interest. This computational strategy was motivated by the fact that, under forcings such as CORE-II or JRA55 and when initialized with PHC hydrography, upper-ocean and surface variables are known to reach quasi-equilibrium within a few decades, as demonstrated in several previous studies. For instance, Wang et al. (2018) reported that temperature and salinity in the upper 1000 m reached near-equilibrium within 20–30 years. Wekerle et al. (2013) began their analysis of surface variables and freshwater content in the 0–500 m layer after a 10-year initialization in a 1958–2007 simulation using FESOM under CORE-II forcing. Likewise, in the analysis of

multiple high-resolution the Ocean Model Intercomparison Project Phase 2 (OMIP2) models simulating the full 1958–2020 period under JRA55 forcing, Wang, Shu, Bozec, et al. (2024) focused their evaluation on the period 1971–2000 – commencing approximately 13 years after the model initialization. In our simulation, the 24-year spin-up from 1958 to 1981 is largely sufficient for the adjustment of surface fields (e.g., sea ice, surface temperature, and salinity) and AW layer (above 1000 m), which are the focus of this study. Although the deep ocean remains far from equilibrium, the targeted variables had largely stabilized by 1981.

From a physical perspective, the potential impact of this initialization approach for the 1995–2020 simulation is expected to be short-lived. The upper ocean and sea ice (the primary focus of this study), adjust much more rapidly than the deep ocean, and their evolution is predominantly governed by contemporaneous atmospheric forcing rather than by the initial conditions.

- Therefore, the disequilibrium introduced by the initial condition from 1981 would be rapidly overwritten and adjusted by the realistic, synchronous atmospheric forcing applied from 1995 onward.
 - Therefore, initializing the 1995 run from the 1981 output allows a computationally efficient hot start and ensures that the model is in an appropriate state for evaluating the 1995–2020 period.
- 220 period, further supporting the validity of this approach. The temporal evolution of key diagnostic variables including sea surface temperature (Fig. 8d) and sea ice-related variables (Fig. 7) shows that the simulation quickly aligns with the observed/reanalysis trajectory after 1995, with no persistent systematic bias. Spatial distributions of these variables are also in good agreement with evaluation datasets (Figs. 3–5, 8a–c), and the long-term trends from 1995 to 2020 closely match those in the references (Fig. 7). These results, which will be discussed in detail in the following sections, indicate that the initialization from 1981 did not adversely affect the simulation of central climate features during the study period.

Accordingly, our primary evaluation focuses on the performance of E3SMv2-MPAS during the period 1995–2020. In addition, a comparative assessment of the 1960–1980 period is also included to briefly examine the decadal variability of key ocean and sea ice variables and to verify the model's capability under distinctly different climatic backgrounds.

2.2 Evaluation **D**datasets

210

215

230 2.2.1 Sea Lice Concentration, extent, and Tthickness, and volume

To comprehensively evaluate sea ice concentration (SIC) performance, both the observations and reanalysis data were adopted for validation. SIC datasets used here include: (1) Passive microwave remote sensing data: Sourced from the National Oceanic and Atmospheric Administration (NOAA) / National Snow and Ice Data Center (NSIDC) Climate Data Record (Version 4; Meier et al. (2021)) with a spatial resolution of 25 km × 25 km; (2) HadISST1 data: Provided by the UK Met Office Hadley Centre (Rayner et al., 2003) at 1° × 1° resolution; (3) ERA5 reanalysis: Generated by the European Centre for Medium-Range Weather Forecasts (ECMWF; Hersbach et al. (2020)) at 0.25° × 0.25° resolution.

For sea ice thickness (SIT) validation, we utilize four key datasets: (1) Pan-Arctic Ice-Ocean Modeling and Assimilation System (PIOMAS; Zhang and Rothrock (2003)): This reanalysis product, extensively validated against satellite and in situ observations, provides reliable Arctic SIT spatial distributions and long-term trends (Laxon et al., 2013; Schweiger et al., 2011; Stroeve et al., 2014). (2) PIOMAS-20C reanalysis (Schweiger et al., 2019): Driven by ECMWF's atmospheric reanalysis of the 20th century (ERA-20C) and calibrated with historical in situ/aircraft measurements, this dataset enables analysis of pre-satellite-era SIT variability (1960–1980). (3) CS2SMOS gridded product: developed by the Alfred Wegener Institute (AWI) and the University of Hamburg (Ricker et al., 2017), it combines CryoSat-2 and SMOS satellite observations using an Optimal Interpolation method. The data cover the period from October to April each year, when the sea ice is more stable, thereby minimizing signal interference from summer melt ponds and enhancing the reliability and accuracy of the dataset. Ice, Cloud, and Land Elevation Satellite 1 (ICESat-1; 2003-2008): Equipped with the Geoscience Laser Altimeter System (GLAS; Zwally et al., 2002), enabling pioneering lidar-based SIT retrievals. (4) ICESat-2 (2018-2020): Employing the Advanced Topographic Laser Altimeter System (ATLAS; Petty et al., 2020) to acquire high-resolution three-dimensional SIT measurements, significantly enhancing small-scale ice monitoring capabilities.

For sea ice extent (SIE), the evaluation dataset was obtained from the NSIDC (Fetterer, 2017). Sea ice volume (SIV) was assessed using outputs from the PIOMAS and PIOMAS-20C reanalysis.

2.2.2 Sea Surface Temperature and Salinity

Sea surface temperature (SST) validation dataset is NOAA's 1/4° Daily Optimum Interpolation Sea Surface Temperature (OISST; Huang et al. (2021)) datasest, represents a long-term climate data record integrating multi-platform observations from satellites, ships, buoys, and Array for real time geostrophic oceanography (Argo) floats. Spatially continuous global SST fields are reconstructed using optimal interpolation to fill data gaps.

For open-water sea surface salinity (SSS) validation (SIC<15%), the National Aeronautics and Space Administration (NASA) sponsored Optimum Interpolation Sea Surface Salinity (OISSS; Melnichenko et al. (2016)) datasest was applied. The product integrates multi-satellite observations from Aquarius, Soil Moisture Active Passive (SMAP), and Soil Moisture and Ocean Salinity (SMOS) through optimal interpolation. Continuous 2011-present data are generated through cross-satellite bias correction and spatial filtering, with SMOS data filling SMAP gaps.

2.2.3 Three-Dimensional Thermohaline

260

265

The World Ocean Atlas 2023 (WOA23; Locarnini et al. (2024); Reagan et al. (2024)) served as the primary validation dataset for three-dimensional thermohaline properties. WOA23 produces high-resolution global climatological temperature and salinity fields via interpolation of historical observations (Argo floats, ship-based measurements, satellite data), covering three periods in this study: 1991–2020, 1995–2004, and 2005–2014.

To assess long-term thermohaline evolution (1960–1980 vs. 2000–2020), the UK Met Office's EN.4.2.2 datasest (Good et al., 2013) was combined. EN.4.2.2 assimilates multi-source in situ data (ship observations, Argo floats, Conductivity

Temperature Depth (CTD) profilers, moored buoys), applies rigorous quality control, and reconstructs 1° × 1° gridded temperature/salinity fields spanning 0–5500 m depth from 1900 onward.

Furthermore, annual mean temperature and salinity profiles (1970–2017) over the Ecast Eurasian Basin, the Wwest Eurasian Basin, the Chukchi Sea, and the Beaufort Gyre from Muilwijk et al. (2023) were included. These data derive from Russian, American, Canadian, and European expeditions, including ship/aircraft surveys, manned drifting stations, autonomous buoys, and submarine measurements.

To evaluate E3SMv2-MPAS performance among models, comparisons were made against CMIP6's 13 high resolution models (Muilwijk et al., 2023) and five high low resolution model pairs from OMIP2 (Wang et al., 2024), covering 1995—2014 and 1958—2018, respectively (see Table 1 and references for details).

Table 1. Numerical implementations of E3SMv2-MPAS, E3SM-Arctic-OSI (Veneziani et al., 2022), 13 CMIP6 models (Muilwijk et al., 2023), and 5 OMIP2 model pairs (Wang et al., 2024), detailing grid type, horizontal resolution in Arctic, and vertical grid.

	Model	Grid type	Horizontal resolution in Aretic (km)	Vertical grid (No. of levels)
E3SMv2	E3SMv2-MPAS	Unstructured	10	z (80)
E3SMv1	E3SM-Aretic OSI	Unstructured	10	z (80)
	BCC-CSM2-MR	Tripolar	5 4	z (40)
	CAMS-CSM1-0	Tripolar	5 4	z (50)
	CESM2	Rotated	41	z (60)
	CanESM5	Tripolar	50	z (45)
	GFDL-CM4	Tripolar	9	p-z* (75)
	GFDL-ESM4	Tripolar	18	p-z* (75)
CMIP6	IPSL-CM6A-LR	Tripolar	49	z* (75)
	GISS-E2-1-H	Regular	46	ρ-z-σ (32)
	MIROC6	Tripolar	39	z-σ (62)
	MPI-ESM1-2-HR	Tripolar	36	z (40)
	MRI-ESM2-0	Tripolar	39	z* (60)
	NorESM2-LM	Tripolar	38	p-z (53)
	UKESM1-0-LL	Tripolar	50	z* (75)
OMIP2	ACCESS-MOM_3.6km	Tripolar	3.6	z* (70)
	ACCESS-MOM_9km	Tripolar	9	z* (50)

AWI-FESOM_4.5km	Unstructured	4.5	z (47)
AWI-FESOM_24km	Unstructured	24	z (47)
CMCC-NEMO_3.2km	Tripolar	3.2	z (98)
CMCC-NEMO_51km	Tripolar	51	z (50)
FSU-HYCOM_3.6km	Tripolar	3.6	ρ-z-σ (36)
FSU-HYCOM_32km	Tripolar	32	ρ-z-σ (41)
IAP-LICOM_6.8km	Tripolar	6.8	η (55)
IAP-LICOM_72km	Tripolar	72	η (30)

Additionally, three dimensional thermohaline outputs from E3SMv1 (60to10 km resolution; 2005–2016 climatology; Veneziani et al., 2022) were analyzed. Golaz et al., (2022) explicitly confirm that the oceanic component MPAS Ocean in E3SMv2 contains no substantial improvements over its E3SMv1 predecessor. Key differences between E3SM Arctic OSI (Veneziani et al., 2022) and E3SMv2 MPAS involve GM eddy diffusivity coefficient (κ) settings. E3SM Arctic OSI disables GM parameterization (κ=0) in Arctic regions, while E3SMv2 MPAS maintains moderate mesoscale diffusion. Though GM deactivation enhances frontal sharpness (e.g., ice-edge zones and thermal gradients), most Arctic regions feature first baroclinic Rossby radii <10 km (Nurser and Bacon, 2014). At 10 km resolution, unresolved mesoscale eddies may cause transport deficiencies, non-physical gradients, and circulation distortions (e.g. anomalous sea ice distributions and systematic thermohaline circulation biases).

2.2.4 Sea surface height, ocean heat content, and surface albedo

280

300

Sea surface height (SSH) evaluation data were derived from the Ocean Reanalysis System 5 (ORAS5), produced by ECMWF (Zuo et al., 2019). ORAS5 integrates multivariate observations via assimilation into the Nucleus for European Modelling of the Ocean (NEMO) ocean model coupled with the Louvain-la-Neuve sea ice model (LIM). The primary assimilated data include altimetry-based sea level anomalies from the AVISO DT2014 product, incorporating an updated mean dynamic topography. The reanalysis has a horizontal resolution of 0.25°, enhanced to approximately 9 km in the polar regions.

Ocean heat content (OHC) evaluation data were sourced from the gridded product developed by the Institute of Atmospheric Physics (IAP), Chinese Academy of Sciences (Cheng et al. 2017, 2020, 2024). It combines multi-source in situ observations – including Argo floats, CTD profiles, ship-based measurements, and moored buoys – on a 1° × 1° horizontal grid. An adaptive Optimal Interpolation method is applied to minimize bias. The dataset covers the period from 1940 to present, supporting analysis of long-term oceanic changes.

Surface albedo evaluation data were obtained from the CLARA-A3 (Karlsson et al., 2023). Observations originate from multiple versions of the Advanced Very High Resolution Radiometer (AVHRR) spaceborne optical imagers employ

intercalibrated radiances to mitigate intersensor discrepancies (Heidinger et al., 2010). The dataset spans from January 1979 to present, provided on a 0.25° global grid, with a 25 km equal-area grid for the polar regions.

305 2.2.54 Atlantic Water Core

310

320

325

330

Observed Atlantic Water (AW) core temperature and depth data were sourced from Richards et al. (2022), comprising 55,841 profiles (1977–2018). AW core was defined as the warmest layer within salinity >34.7 PSU profiles. To ensure accuracy, only profiles exceeding 500 m depth with sampling starting above 100 m were retained. Raw profiles were smoothed using an 80 m vertical moving average (40 m window) to remove spikes caused by thermohaline intrusions and eddies while preserving overall thermal structure.

Wang et al. (2024)'s OMIP2 dataset includes AW core temperature (defined as maximum temperature in water columns over seafloor depths >150 m; 2006–2017) from five high-low resolution model pairs. This dataset is employed to benchmark E3SMv2-MPAS's AW core temperature simulations against multi-model ensembles.

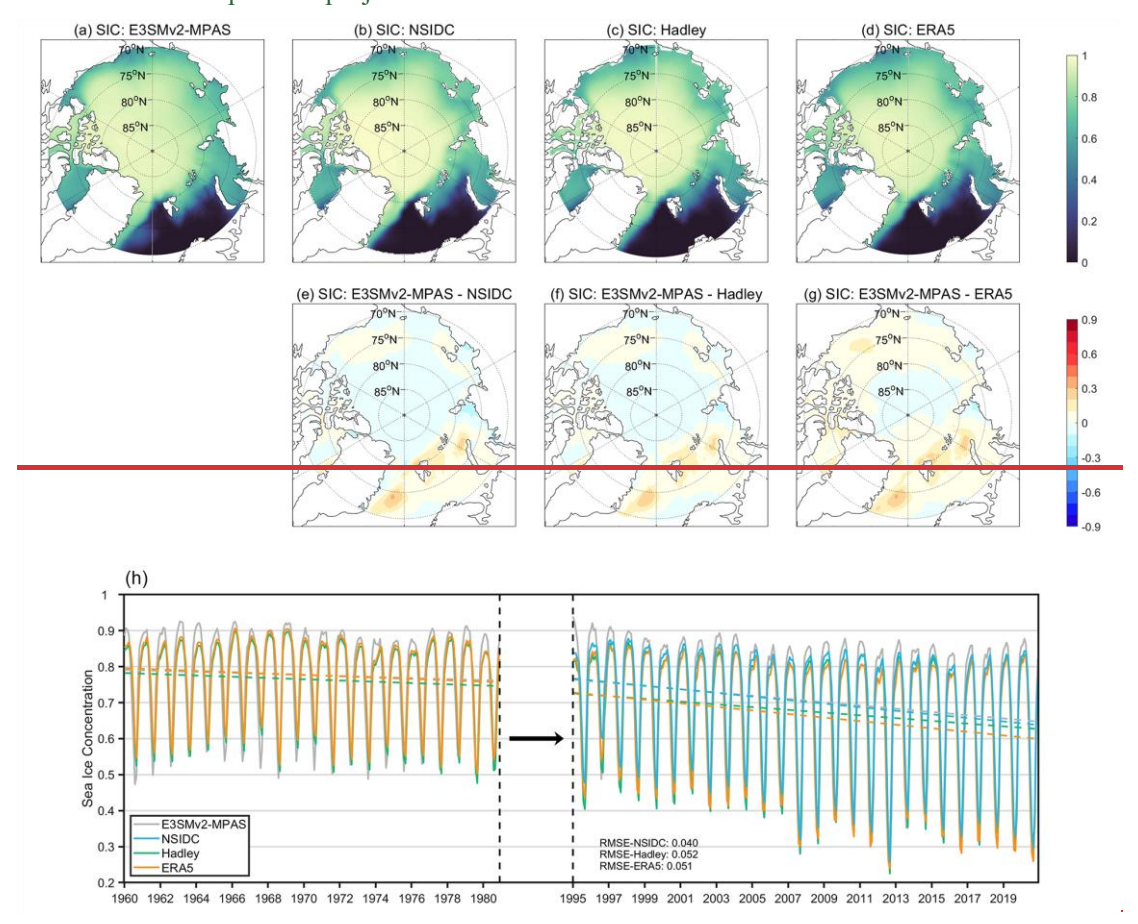
3 Arctic Pphysical Ssystem Sstates

3.1 Sea Hee Ccharacterization

This study focuses on the Arctic region, systematically evaluating the simulation performance of the E3SMv2-MPAS coupled model for sea ice concentration (SIC), sea ice thickness (SIT), SIE and SIVsea surface temperature (SST), and sea surface salinity (SSS) at first. Through comparisons with multi-source observational datasets and reanalysis products, combined with climate-state analysis (1995–2020) and trend diagnostics across two periods (1960–1980 and 1995–2020), model strengths and limitations in polar environmental simulations are identified.

Multi-dataset validation using NSIDC satellite remote sensing (Meier et al., 2021), Hadley in situ assimilation (Rayner et al., 2003), and ERA5 reanalysis (Hersbach et al., 2020) demonstrates that E3SMv2-MPAS effectively captures spatial heterogeneity in Arctic SIC climatology in both winter and summer (Figs. 3 and 4a-g). In winter, Consistent spatial bias patterns are observed across datasets, with persistent positive bias centers (ΔSIC>0.3) identified along the southwestern Greenland Sea shelf margin and the northern Barents Sea slope (Fig. 3e-g). During summer, comparisons with NSIDC and Hadley reveal predominant positive biases in the northern Barents Sea and widespread negative biases across the central Arctic Ocean (Fig. 4e and f). In contrast, the comparison with ERA5 shows negligible underestimation in the central Arctic basin, while positive biases are observed not only in the northern Barents Sea but also in the Beaufort Sea (Fig. 4g). Notably, E3SMv2 MPAS exhibits superior performance relative to CMIP6 ensemble members, demonstrating smaller spatial bias magnitudes than most models (Long et al., 2021). E3SMv2 MPAS successfully reproduces SIC seasonal cycles and interannual variability, maintaining root mean square errors (RMSE) values of 0.040, 0.052, and 0.051 against NSIDC, Hadley, and ERA5 datasets respectively (Fig. 3h). This validates the dynamic framework's effectiveness in capturing sea ice-atmosphere coupling mechanisms. However, the asymmetric seasonal biases in E3SMv2 MPAS are identified, which shows:

systematic winter overestimation contrast with moderate summer underestimation (primarily compared with NSIDC), suggesting potential improvements needed in simulating ice-albedo feedback and melt pond dynamics. Trend analysis confirms the model's climate response capability. During the rapid decline period (1995–2020), E3SMv2-MPAS accurately captures accelerated SIC reduction trends, showing better agreement with NSIDC observations than Hadley and ERA5 products. For the weak trend period (1960–1980), the model reproduces quasi-stable sea ice coverage characteristics while maintaining overestimated seasonal variability amplitudes. The accelerated SIC decline in the recent period compared to historical decades highlights the model's ability to replicate trend amplification under intensified forcing, thereby bolstering confidence in its scenario-dependent projections.



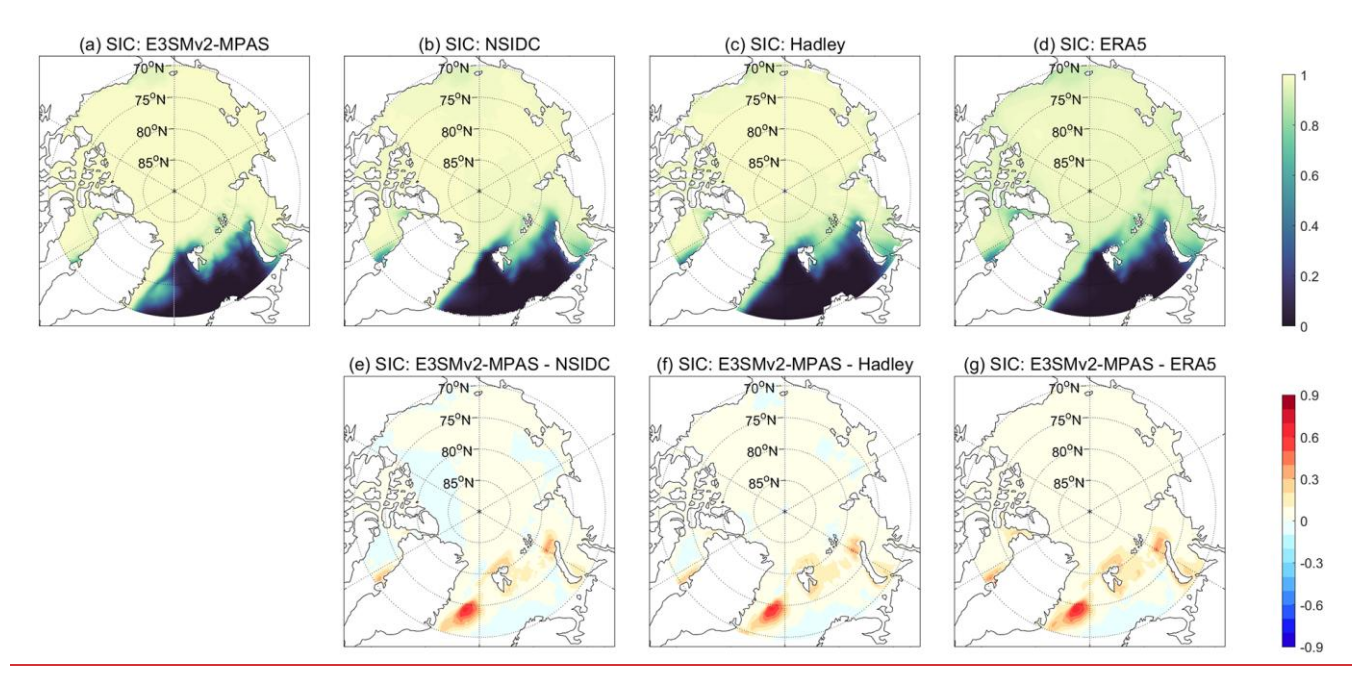


Figure 3. <u>During winter (December-February)</u>, (a-d) 1995-2020 climatological mean <u>sea_ice_concentration</u> (SIC) spatial distributions: (a) E3SMv2-MPAS simulations, (b) NSIDC observational product, (c) Hadley Centre HadISST data, (d) ERA5 reanalysis. (e-g) SIC bias fields: (e) E3SMv2-MPAS vs. NSIDC, (f) E3SMv2-MPAS vs. Hadley, (g) E3SMv2-MPAS vs. ERA5. (h) Pan Arctic (70°N 90°N) mean SIC time series for 1960-1980 and 1995-2020, with dashed lines indicating linear trends (E3SMv2-MPAS: gray; NSIDC: blue; Hadley; green; ERA5; orange) derived from least-squares regression.

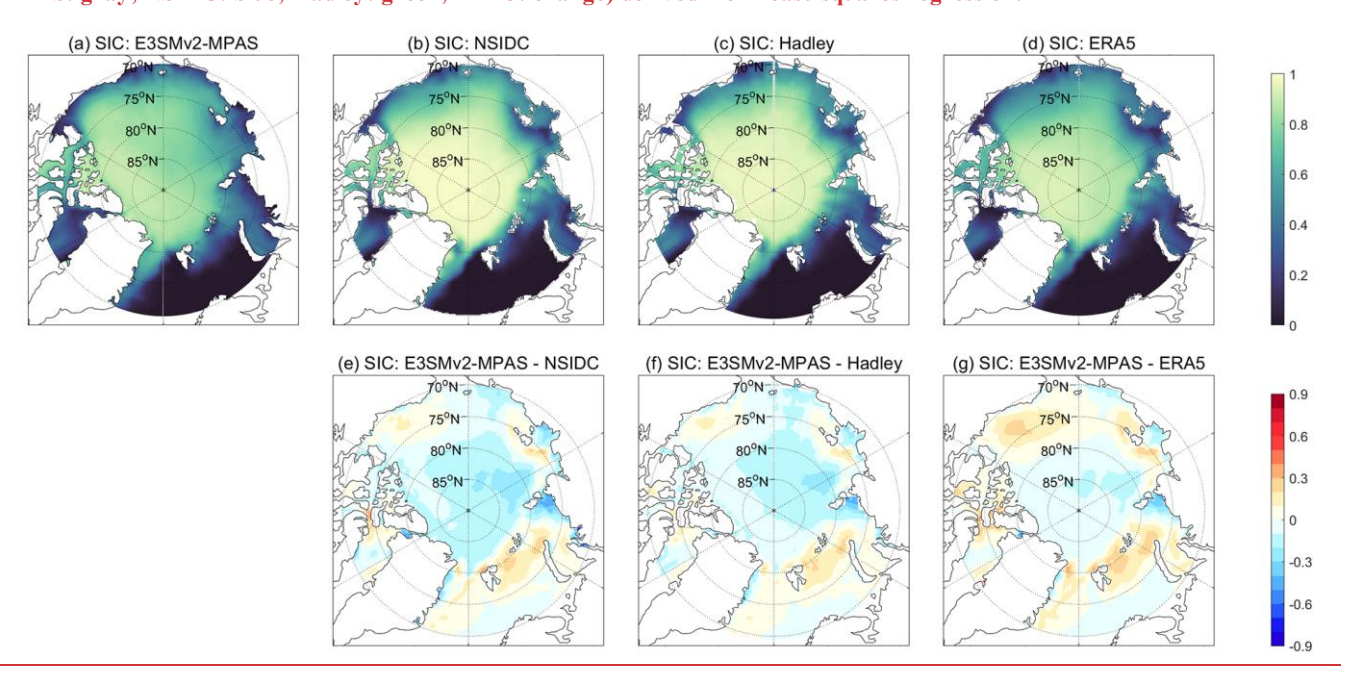
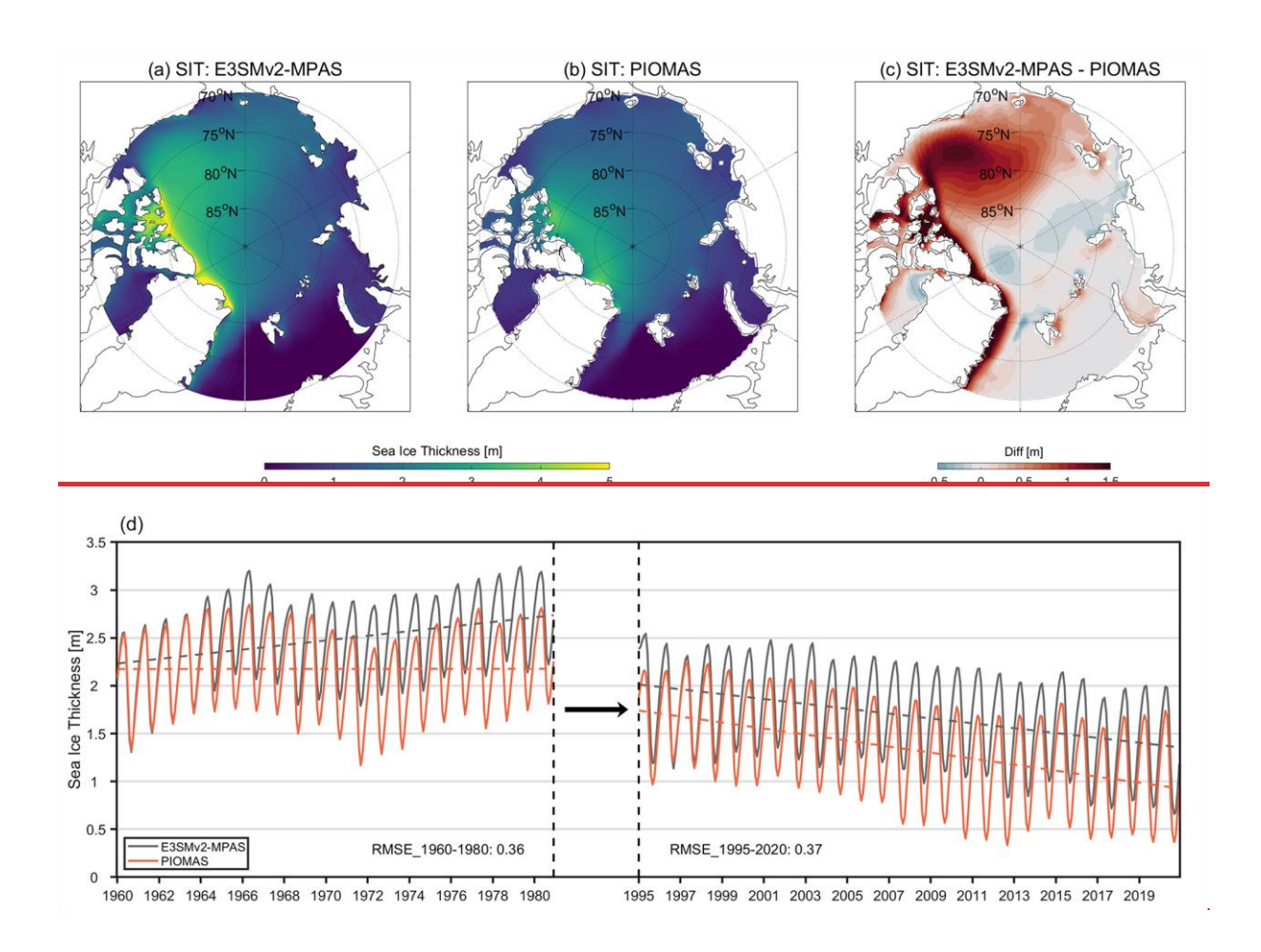


Figure 4. The same as Fig. 3, but during summer (June-August).

Beyond SIC, SIT serves as a critical parameter governing sea ice dynamics, with its simulation accuracy directly modulating the spatiotemporal heterogeneity of ice volume. We systematically quantify E3SMv2-MPAS's capability in reproducing spatial distribution of SIT spatiotemporal evolution during both in winter and summer (Fig. 54). Overall, the model captures the climatological spatial gradient of Arctic SIT, characterized by a gradual thickening from the Barents Sea toward the central Arctic Basin and the northern Canadian Archipelago in both seasons. The model realistically represents the seasonal reduction in SIT over the continental shelf regions along the Arctic margin in summer compared to winter. However, pronounced zonal positive biases (\Delta SIT > 1.5 m) are present in both seasons, particularly along the eastern and northern shelf of the Greenland Sea, the region north of the Canadian Archipelago, and the southern Canadian Basin and Beaufort Sea (Fig. 5c and f). Comparative analysis demonstrates the model effectively captures Arctic SIT spatial gradients (Fig. 4a-c). Although the model generally overestimates SIT, the time series analysis successfully simulates continuous thinning from ~1.8 m to ~1.3 m during 1995 2020 (Fig. 4d). Notably, however, the simulated thinning rates remain slightly lower than PIOMAS results. Stable RMSE values (~0.37) throughout this period confirm robust simulation of long-term SIT evolution. For the pre-satellite era (1960-1980), evaluation using PIOMAS-20C shows E3SMv2-MPAS reproduces the 6-year evelic "increase decrease increase" SIT fluctuations during 1960-1978 (Fig. 4d). While PIOMAS-20C shows no statistically significant SIT trend during 1960–1980, E3SMv2-MPAS simulates a pronounced thickening trend in this period, potentially linked to its systematic overestimation of regional ice thickness in areas like the Beaufort Sea (Fig. 4c). Nevertheless, across the multi-decadal scale (1960-2020), this counted system demonstrates a reasonable representation of Arctic sea ice responses to climate forcing.

355

360



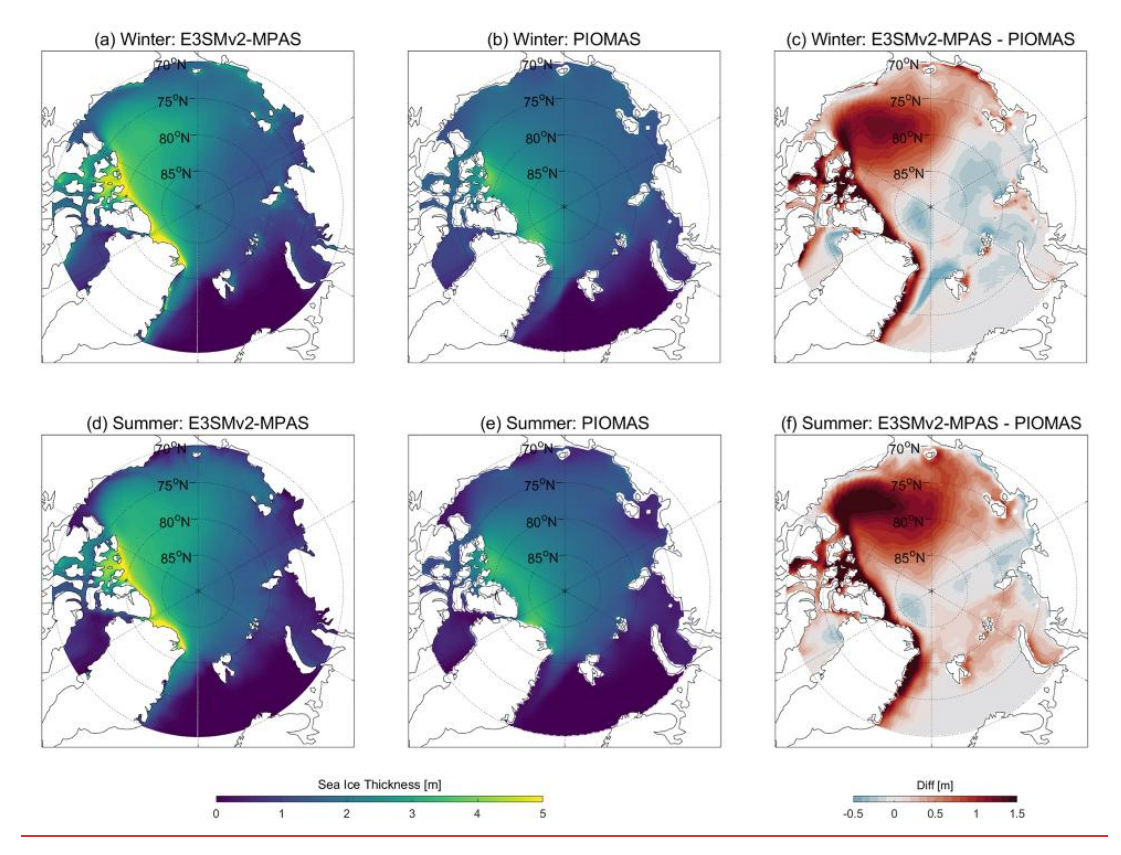


Figure 54. During (a-c) winter (December-February) and (d-f) summer (June-August), (a-b_and d-e) 1995-2020 climatological mean sea ice thickness (SIT) spatial distributions: (a and d) E3SMv2-MPAS, (b and e) PIOMAS. (c and f) SIT bias field: E3SMv2-MPAS vs. PIOMAS. (d) Pan Arctic (70°N-90°N) mean SIT time series for 1960-1980 and 1995-2020, with dashed lines indicating linear trends (E3SMv2-MPAS: black; PIOMAS: red) derived from least-squares regression.

Spatial analysis identifies significant zonal positive biases (ASIT>1.5 m) along the eastern and northern Greenland Sea shelf and the Canadian Archipelago (Fig. 4e). Considering PIOMAS's known limitations in overestimating thin ice while underestimating thick ice (Laxon et al., 2013; Schweiger et al., 2011), additional validation using CS2SMOSICESat altimetry data (Ricker et al., 2017) is conducted (Fig. S15). Consistent with previous findings, PIOMAS exhibits underestimation in regions with thicker sea ice, such as north of the Canadian Archipelago and east of Greenland (Fig. S1e). Similarly, E3SMv2-MPAS shows pronounced positive biases relative to CS2SMOS in areas including the northern Canadian Archipelago, the southern Canadian Basin, and the Beaufort Sea (Fig. S1d), aligning with the bias pattern identified in comparisons with PIOMAS (Fig. 5c), thereby corroborating the spatial reliability of PIOMAS-indicated biases. Case studies of specific months (February 2005, October 2005, October 2006, March 2007, March 2019, October 2019) show improved agreement with ICESat observations in the Canadian Archipelago and Greenland coastal regions compared to PIOMAS. The spatial pattern of maximum positive bias in E3SMv2-MPAS remains consistent across seasons (Fig. 5c and f). This bias is also evident in the model's annual mean SIT distribution relative to PIOMAS (Fig. S2). Previous studies based on CMIP5 models have established a strong correlation between inaccuracies in simulating the Beaufort Gyre and SIT distribution

(Stroeve et al., 2014). Since the SSH field serves as a key proxy for evaluating the fidelity of Beaufort Gyre simulations (Wang et al., 2018), we analyze differences in SSH between E3SMv2-MPAS and the ORAS5 reanalysis (Fig. 6a–c). The model overestimates SSH in the Beaufort Sea, suggesting an erroneously enhanced ice convergence. Additionally, the simulated OHC in the 0–100 m layer is underestimated in this region (Fig. 6d–f), which may further contribute to the positive SIT bias. Thus, the pPersistent 0.5–1 m positive biases in the Beaufort Sea Canadian Basin interior is are hypothesized to originate from an overestimated intensity of the Beaufort Gyre and associated upper-ocean thermal biases in E3SMv2-MPAS, which then may impede the realistic export of sea ice through the north of Canadian Archipelago and east of Greenland.potentially enhancing sea ice convergence processes.

390

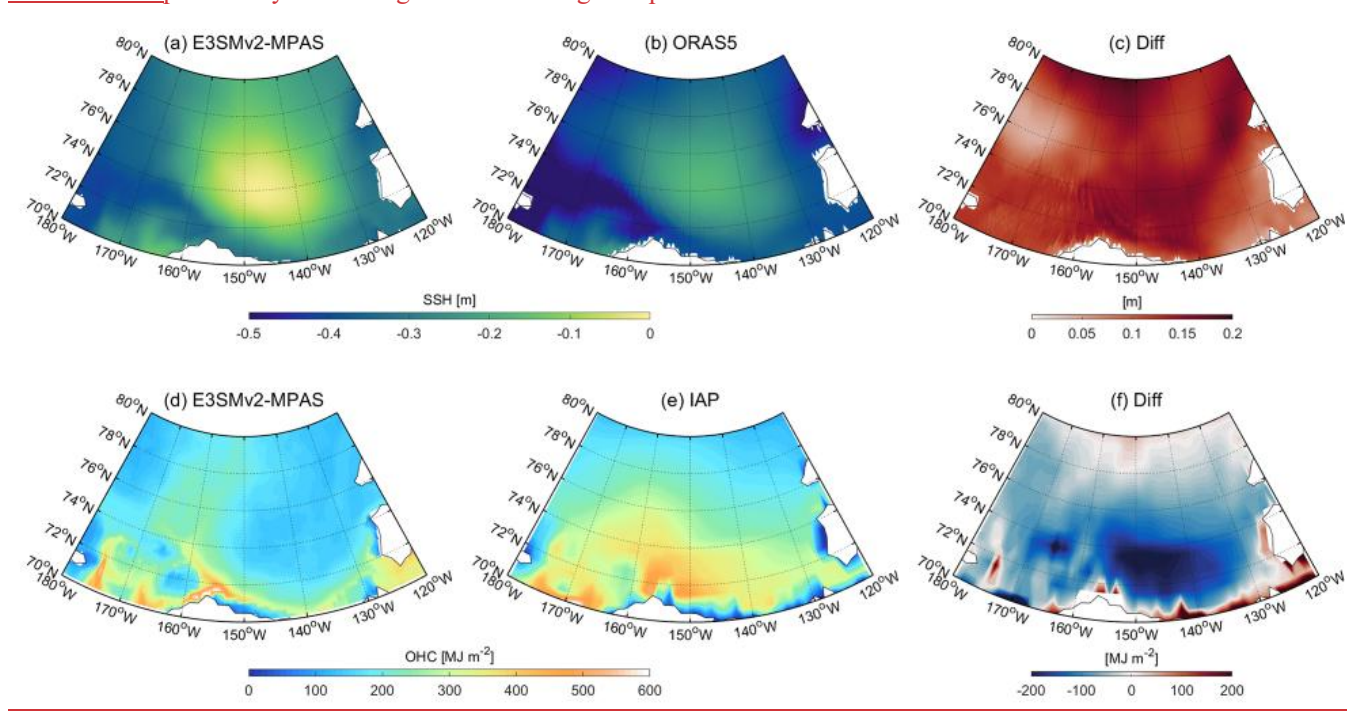


Figure 6. Climatological mean spatial distributions for the period 1995–2020. (a-c) SSH: (a) E3SMv2-MPAS, (b) ORAS5. (c) Bias in SSH between E3SMv2-MPAS and ORAS5. (d-f) OHC in the upper 100 m: (d) E3SMv2-MPAS, (e) IAP. (f) Bias in OHC between E3SMv2-MPAS and IAP.

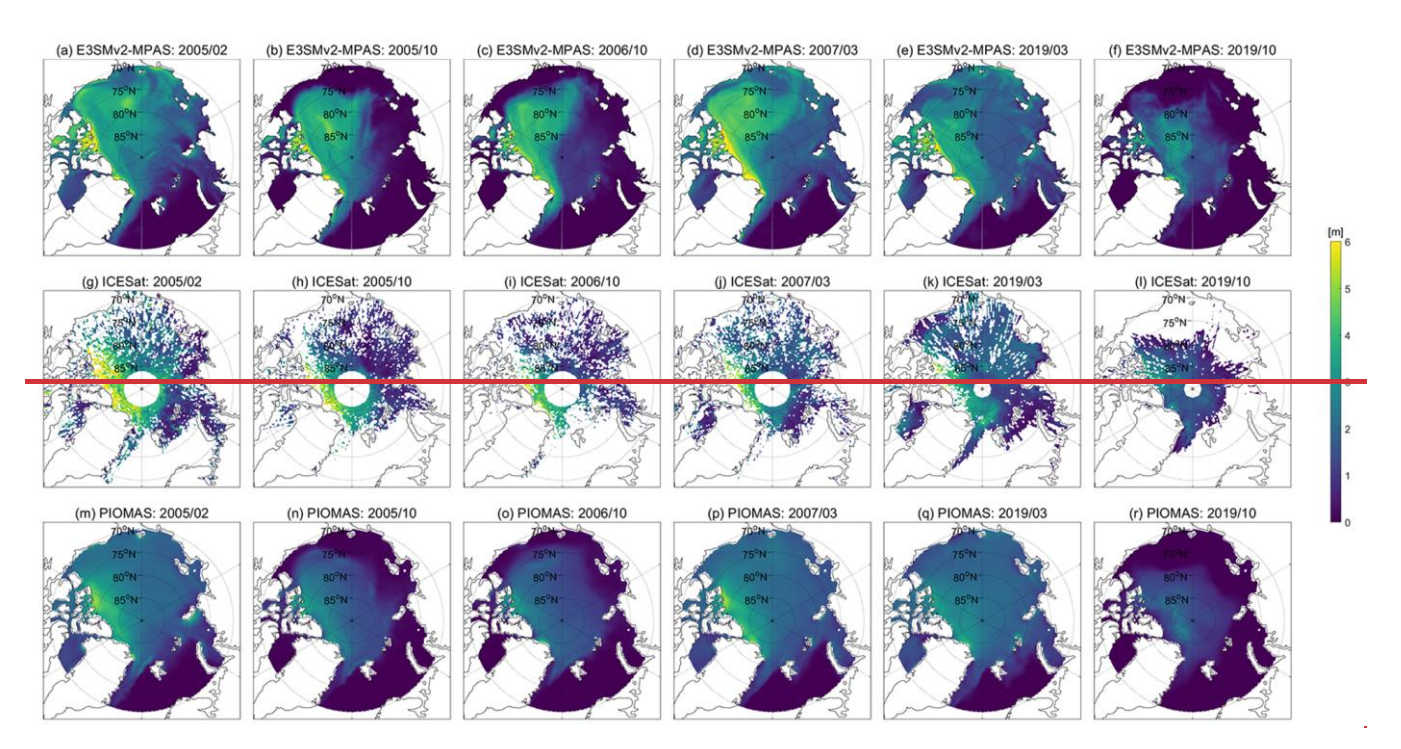


Figure 5. Seasonal sea ice thickness spatial distributions. Rows: (1) E3SMv2 MPAS, (2) ICESat, (3) PIOMAS. Columns: (1) February 2005, (2) October 2005, (3) October 2006, (4) March 2007, (5) March 2019, (6) October 2019.

To further analyze long-term trends in sea ice-related variables, including interannual and decadal variability, time series of SIC, SIT, SIE, and SIV are examined over the periods 1960–1980 and 1995–2020 (Fig. 7).

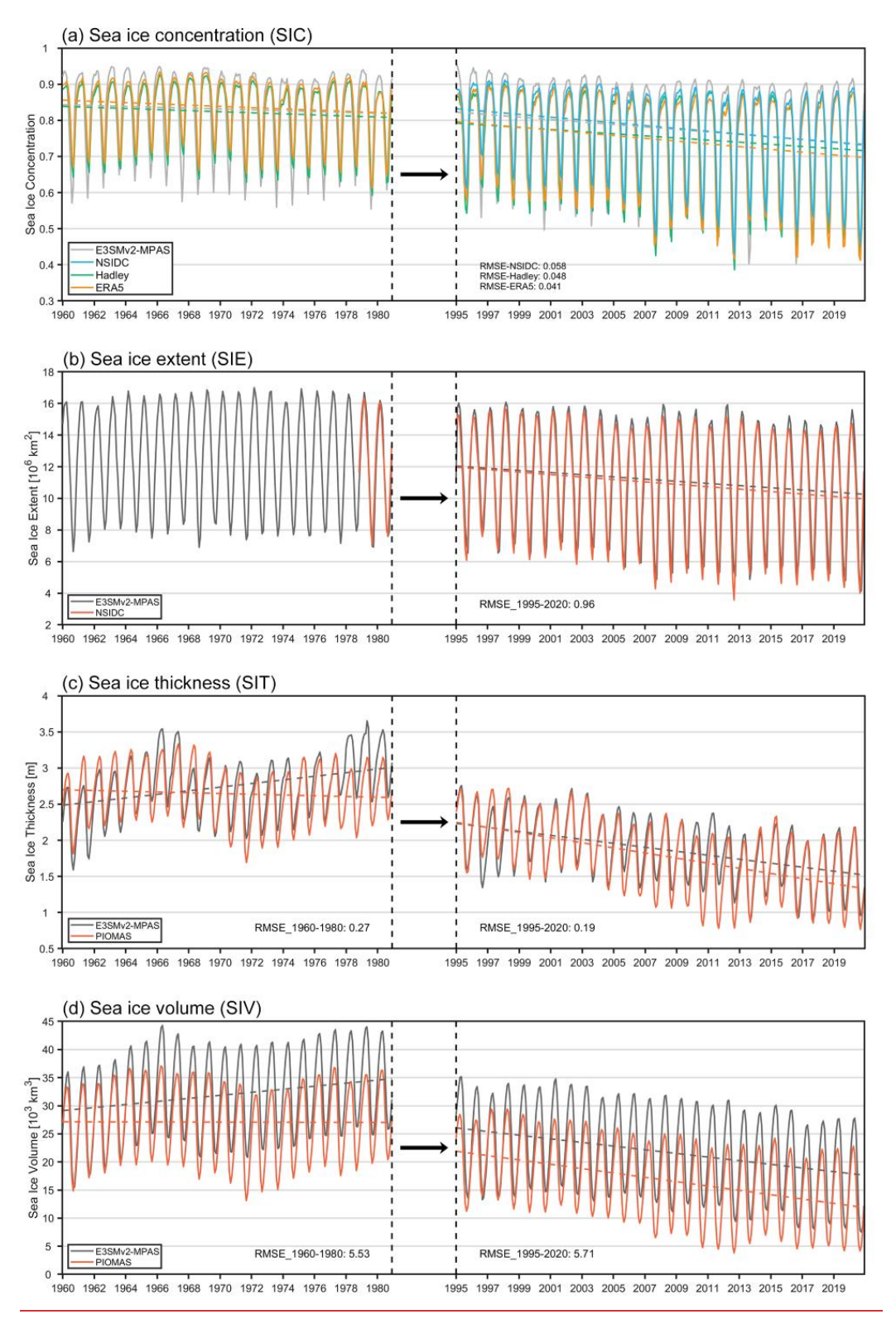


Figure 7. Time series and linear trends of sea ice properties from 1960–1980 and 1995–2020. (a) SIC of pan-Arctic (70°–90°N) for E3SMv2-MPAS (gray), NSIDC (blue), Hadley (green), and ERA5 (orange). (b) SIE for E3SMv2-MPAS (black) and NSIDC (red). (c) SIT of pan-Arctic (70°–90° N) for E3SMv2-MPAS (black) and PIOMAS (red). (d) SIV for E3SMv2-MPAS (black) and PIOMAS (red). Dashed lines denote linear trends based on least-squares regression.

410

415

420

430

435

E3SMv2-MPAS successfully reproduces SIC seasonal cycles and interannual variability during 1995–2020, maintaining root mean square errors (RMSE) values of 0.040, 0.052, and 0.051 against NSIDC, Hadley, and ERA5 datasets respectively (Fig. 7a3h). This validates the dynamic framework's effectiveness in capturing sea ice-atmosphere coupling mechanisms. However, the asymmetric seasonal biases in E3SMv2-MPAS are identified, which shows: systematic winter overestimation contrast with moderate summer underestimation (primarily compared with NSIDC), suggesting potential improvements needed in simulating ice-albedo feedback and melt pond dynamics. Trend analysis confirms the model's climate response capability. During the rapid decline period (1995–2020), E3SMv2-MPAS accurately captures accelerated SIC reduction trends, showing better agreement with NSIDC observations than Hadley and ERA5 products. For the weak-trend period (1960–1980), the model reproduces quasi-stable sea ice coverage characteristics—while maintaining overestimated seasonal variability amplitudes. The accelerated SIC decline in the recent period compared to historical decades (1960–1980) highlights the model's ability to replicate trend amplification under intensified forcing, thereby bolstering confidence in its scenario-dependent projections. Similarly, the model effectively captures the interannual and decadal variability of SIE (Fig. 7b; RMSE: 0.96).

Consistent with NSIDC, simulated SIC and SIE exhibit certain seasonal biases. The systematic winter overestimation, attributable to positive SIC biases in the southern Greenland Sea and southward-expanded ice cover in the Barents Sea (Fig. 3e), coinciding with pronounced cold SST biases in these regions (Fig. S3). During summer, E3SMv2-MPAS overestimates the seasonal minimum (Fig. 7a–b), particularly in the Greenland Sea, Barents Sea, East Siberian-Laptev Seas, and Beaufort Sea (Fig. 4e). These regions also exhibit elevated surface albedo values (Fig. S4), reducing absorbed shortwave radiation and contributing to the sea ice overestimation.

Although the model generally overestimates SIT (Figs. 5 and S2), the time series analysis successfully simulates continuous thinning from ~1.8 m to ~1.3 m during 1995–2020 (Fig. 7c4d). Notably, however, the simulated thinning rates remain slightly lower than PIOMAS results. Stable RMSE values (~0.37) throughout this period confirm robust simulation of long-term SIT evolution. Similarly, compared to PIOMAS, the simulated SIV is consistently underestimated throughout the period, though the declining trend during 1995–2020 is well captured (Fig. 7d). For the pre-satellite era (1960–1980), evaluation using PIOMAS-20C shows E3SMv2-MPAS reproduces the 6-year cyclic "increase-decrease-increase" SIT fluctuations during 1960–1978 (Fig. 7c4d). While PIOMAS-20C shows no statistically significant SIT trend during 1960–1980, E3SMv2-MPAS simulates a pronounced thickening trend in this period, potentially linked to its systematic overestimation of regional ice thickness in areas like the Beaufort Sea (Fig. 5c and f, Fig. S2c4e). Nevertheless, across the multi-decadal scale (1960–2020), this coupled system demonstrates a reasonable representation of Arctic SIT and SIV sea ice responses to climate forcing.

3.2 Surface **Tthermohaline Ssignatures**

SST and SSS engage in complex bidirectional coupling with the atmosphere-ice system through ice/atmosphere-ocean interfacial energy-mass exchange processes. This section evaluates the spatiotemporal co-variability of SST/SSS to elucidate E3SMv2-MPAS's representation of ocean-sea ice-atmosphere interaction mechanisms.

OISST-based validation demonstrates E3SMv2-MPAS accurately reproduces key Arctic SST spatial patterns: (1) temperature gradients decreasing from shelves to central basins, and (2) warm-core features in southern Barents Sea open waters (Fig. 86a-c). Systematic regional biases are identified: the cold biases in the Greenland Sea (ΔSST≈-2–0°C) spatially correlate with an overestimation of SIC in the same region, while positive deviations (ΔSST≈0–2°C) occur near Svalbard's western coast and the Eurasian continental margins. Notably, continental coastal biases are spatially decoupled from Atlantic inflow pathways, with formation mechanisms likely associated with inaccurate vertical mixing processes stemming from stratification stability biases in shelf regions. E3SMv2-MPAS successfully captures Arctic SST warming trends during the 1995–2020 period, showing high consistency with OISST in accelerated trend characteristics (Fig. 86d). Seasonal cycle and interannual variability simulations remain within acceptable error ranges (RMSE=0.24), confirming appropriate responses to surface thermal forcing. Furthermore, the model accurately captures both the pronounced SST increase and accelerated decadal warming trend during 1995–2020 relative to the 1960–1980 baseline period. These simulated changes show a strong coupling with the accelerated decline in SIC, SIE, SIT, and SIVT concurrently (Figs. 73h, 4d).

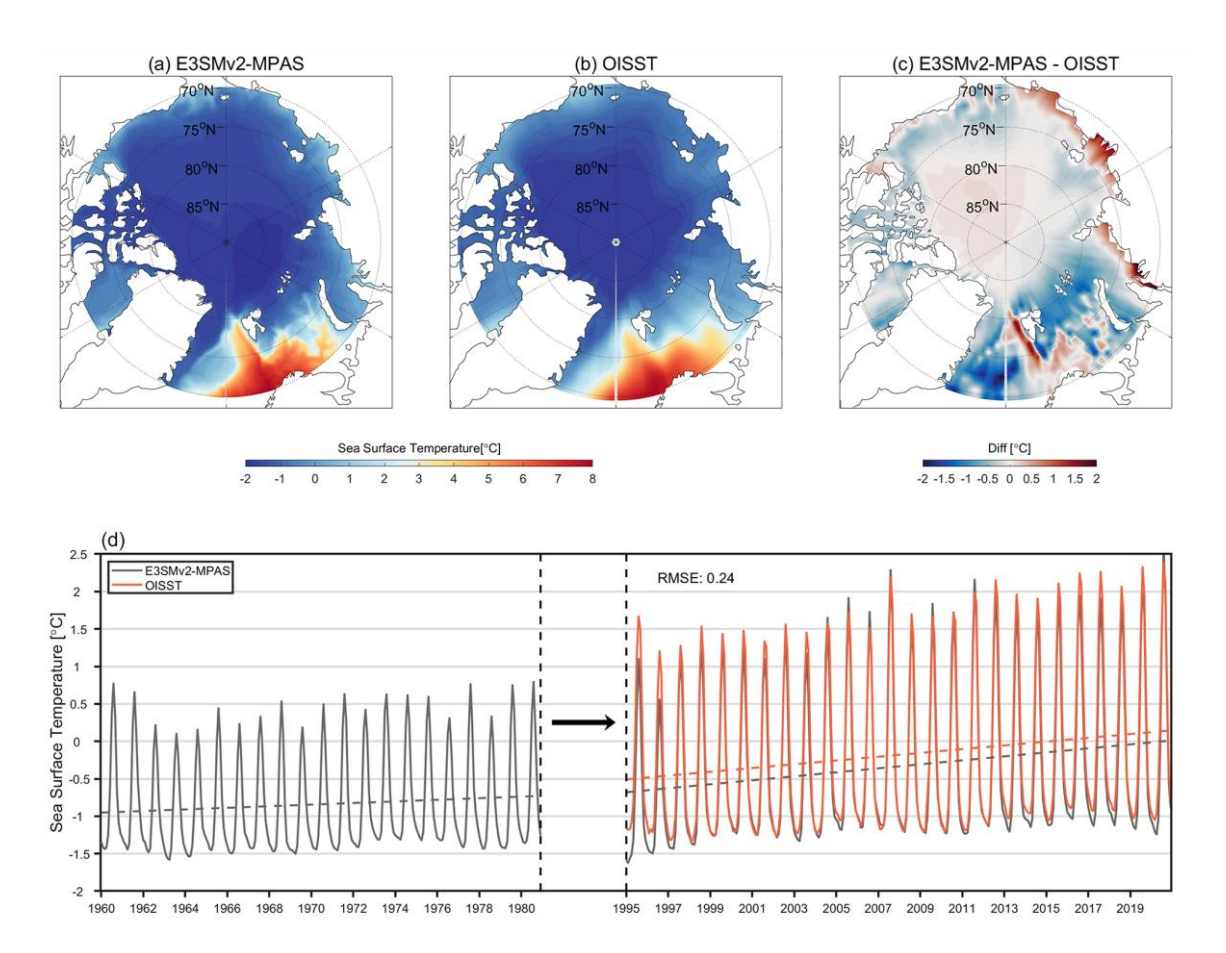
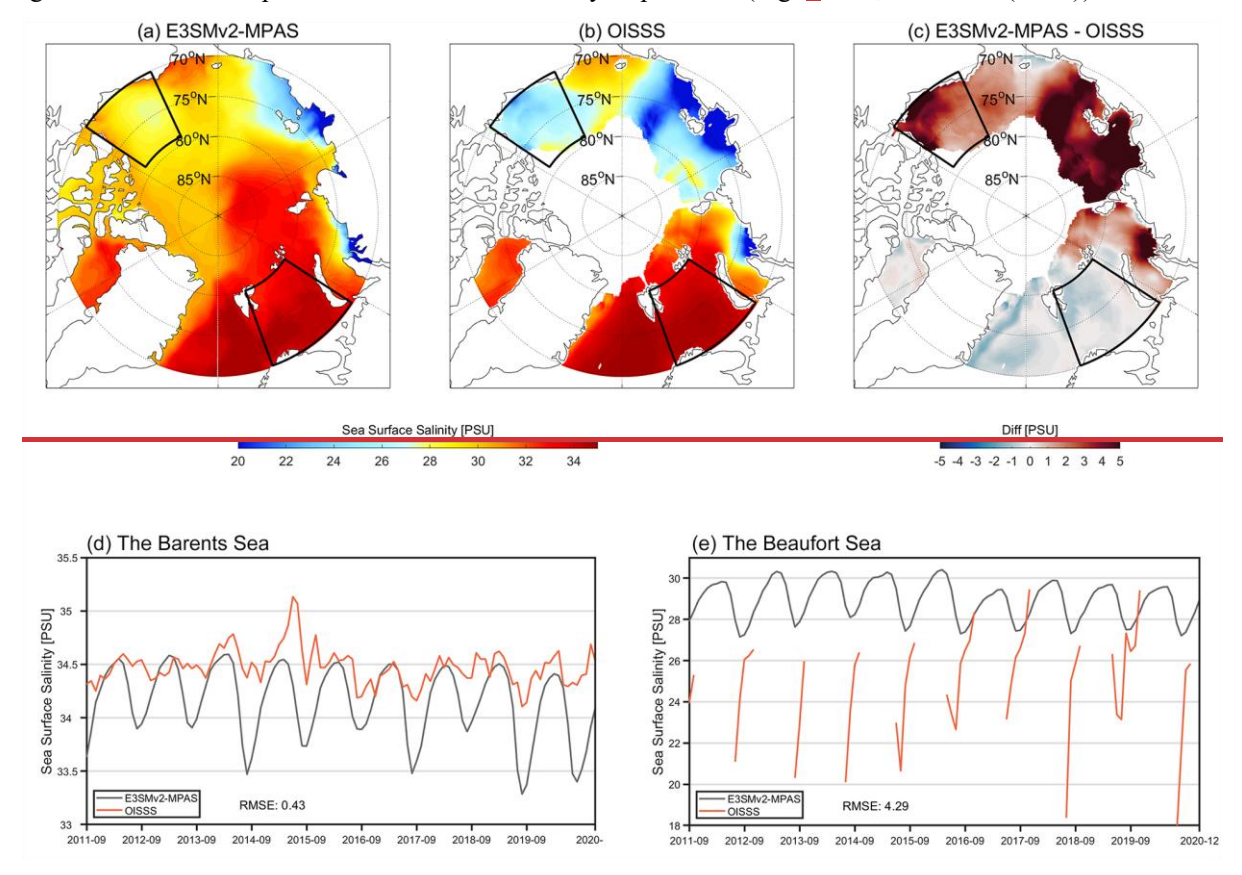


Figure 86. (a-b) 1995-2020 climatological mean sea surface temperature (SST) spatial distributions: (a) E3SMv2-MPAS, (b) OISST. (c) SST bias field: E3SMv2-MPAS vs. OISST. (d) Pan-Arctic (70°_N-90°_N) mean SST time series for 1960-1980 and 1995-2020, with dashed lines indicating linear trends (E3SMv2-MPAS: black; OISST: red) derived from least-squares regression.

E3SMv2-MPAS demonstrates comparatively weaker performance in SSS simulation versus sea ice and SST variables. Spatially heterogeneous biases are observed: negative deviations (ΔSSS=-0-1 PSU) in the Barents and Greenland Seas contrast with pronounced positive biases (ΔSSS=2-5 PSU) in the Beaufort Sea and the Kara-Beaufort shelf regions (Fig. 97a-c). The 3 PSU overestimation in the Beaufort Sea aligns with advanced assimilation model (such as HYCOM and GLORYS12) biases reported by Hall et al. (2021), suggesting common limitations in Arctic shelf freshwater transport representation. Specifically, inadequate parameterization of surface freshwater budgets and associated processes (e.g., precipitation-evaporation fluxes, river discharge, and ice-ocean interactions) may constrain freshwater cycle simulations (Wang et al., 2024). The Beaufort Sea SIT overestimation identified previously (Fig. 54a-e) potentially exacerbates salinity biases through reduced freshwater release (Kelly et al., 2019). If the intensity of the Beaufort Gyre is overestimated (as discussed in Section 3.1), enhanced freshwater retention could impede westward shelf transport to the Kara Sea, potentially driving salinity overestimation in the Kara-Beaufort shelf. Despite spatial biases, E3SMv2-MPAS demonstrates credible

465

simulation of seasonal cycle phasing and amplitude in the Barents Sea SSS, while the temporal variations in the Beaufort Sea show agreement levels comparable to mainstream reanalysis products (Fig. 97d–e; Hall et al. (2021)).



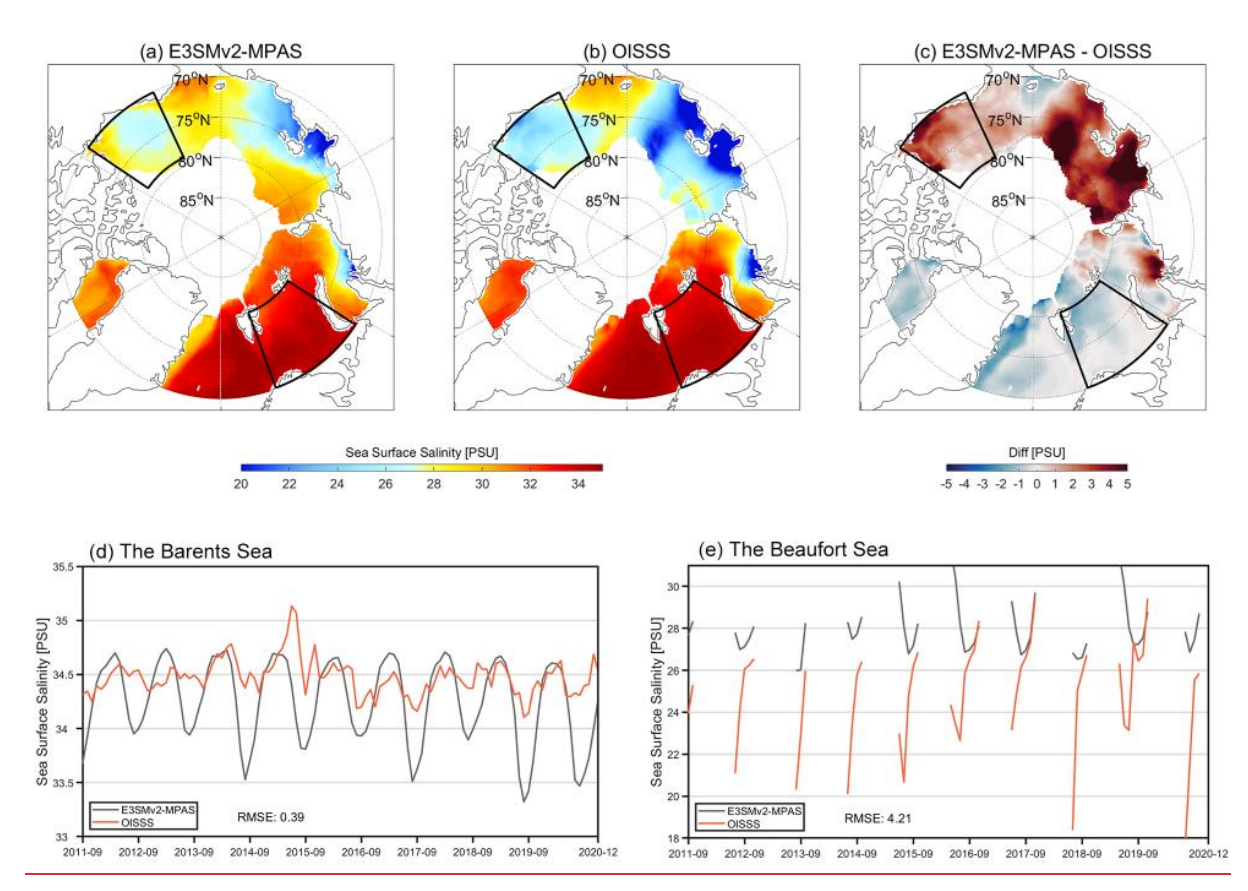


Figure 97. (a-b) September 2011–December 2020 climatological mean sea surface salinity (SSS) spatial distributions: (a) E3SMv2–MPAS, (b) OISSS. (c) SSS bias field: E3SMv2–MPAS vs. OISSS. (d–e) Regional SSS time series in (d) the Barents Sea and (e) the Beaufort Sea (black boxes in a–c; E3SMv2–MPAS: black; OISSS: red).

In the Greenland and Barents Seas, systematic underestimation of SST and SSS (Figs. 86a-c_and, 97a-c) coincides with overestimation of SIC (Figs. 3a_and_4g). Three dimensional thermohaline profile analysis (1995-2014, with WOA23, figure omitted) reveals satisfactory mid depth salinity simulations but overestimation of temperature in the Barents Sea subsurface layers. This indicates effective capture of AW inflow (characterized by high temperature and salinity) through the Barents Sea Opening (BSO), albeit with slight thermal influence overestimation. Surface thermohaline underestimation may originate from insufficient representation of subsurface to surface vertical mixing processes: reduced surface heat/salt fluxes caused by underestimated mixing efficiency could enhance sea ice maintenance mechanisms, thereby amplifying overestimation of SIC. These regions are situated within the marginal ice zone, where strong surface wind stress facilitates the transfer of energy to deeper ocean layers through the excitation of near-inertial oscillations and associated turbulent mixing processes (D'Asaro, 1985). This discrepancy may be attributed to the model's potential overestimation of this downward energy transfer. Similarly, Zhu et al. (2022) reported that in the equatorial Pacific cold tongue region, the KPP scheme overestimates downward turbulent heat flux, leading to a cold bias in both upper-ocean and sea surface temperatures.

A primary reason for these biases lies in the scheme's reliance on a single Richardson number (Ri) relationship for parameterization. Although this approach captures instability conditions in stratified shear flows, it is insufficient to uniquely determine turbulent states and mixing intensities (Zhu et al., 2022), thus limiting its performance in complex dynamic environments. These vertical process biases, combined with surface freshwater transport limitations, constitute key uncertainty sources in regional climate simulations.

3.3 Three-Ddimensional Tthermohaline Sstructure

495

500

505

510

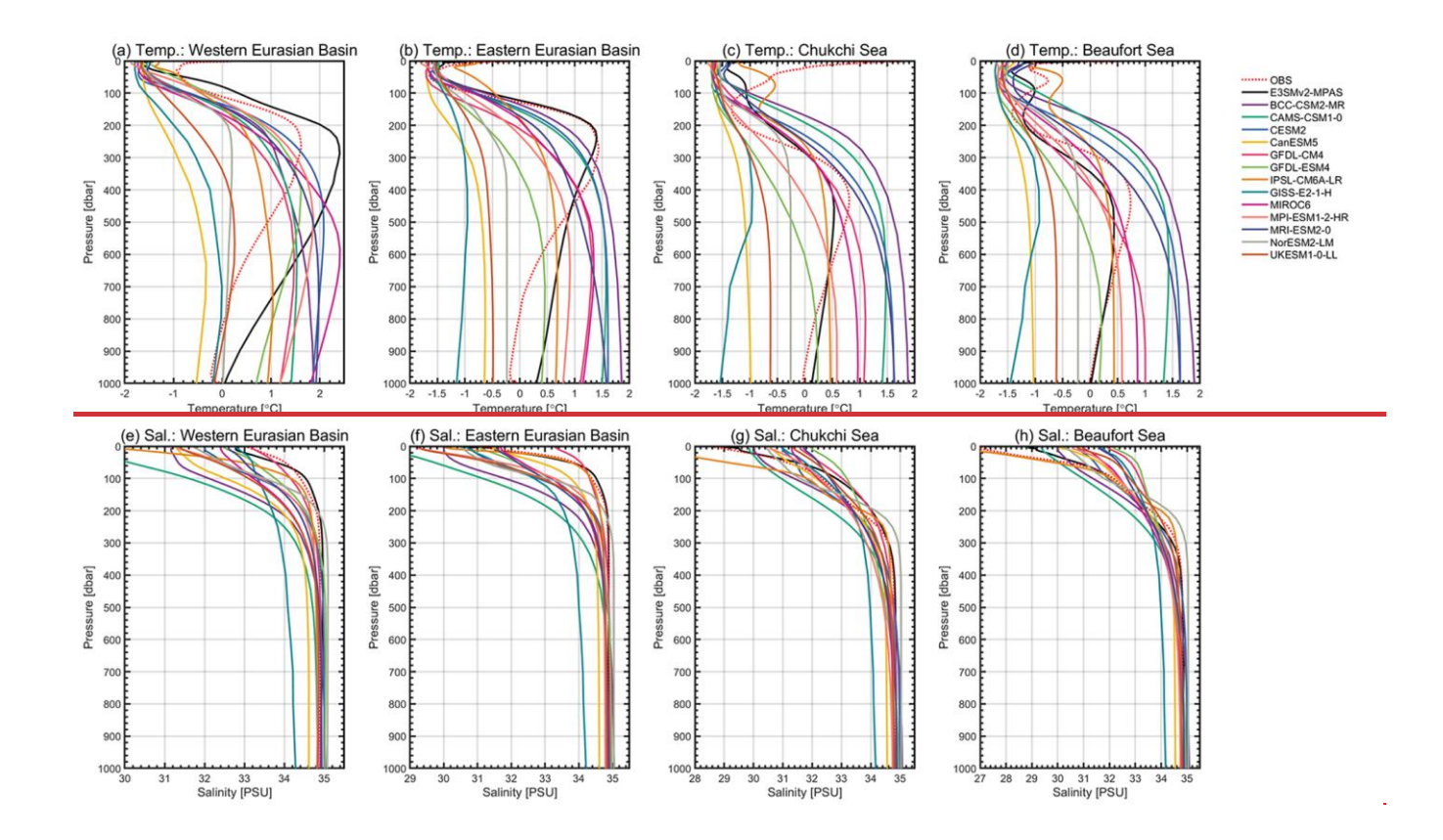
515

520

Accurate simulation of three-dimensional thermohaline fields remains a core technical challenge in ocean model development, directly determining model capability in representing Arctic multi-sphere coupling processes (ocean-ice-atmosphere). While preliminary evaluations of key sea ice properties (including concentration, extent, thickness, and volume)sea ice thickness concentration—and surface thermohaline diagnostics have validated E3SMv2-MPAS's capacity to simulate Arctic shallow-layer thermal states, subsurface-to-deep thermohaline structure biases may still induce circulation distortions, material transport deviations, cross-basin exchange inaccuracies, and climate feedback misrepresentations. A multi-dimensional verification framework including spatial heterogeneity diagnostics, temporal evolution analysis and three-dimensional dynamical validation is established to assess E3SMv2-MPAS's three-dimensional thermohaline simulation performance comprehensively.

Using the 1995–2014 climatological mean profiles, systematic comparisons are conducted between E3SMv2-MPAS, and observational data (Muilwijk et al., 2023), and 13 high-resolution CMIP6 models (horizontal resolution <60 km; Muilwijk et al., 2023; see Table 1) across four regions: the western Eurasian Basin, the eastern Eurasian Basin, the Chukchi Sea, and the Beaufort Sea. Thermohaline profile characteristics (0–1000 m depth) are evaluated through vertical structure evolution and regional variability analyzes analyses.

Although the CMIP6 models have relative high resolution, they exhibit systematic biases in AW core characterization as follows: (1) Substantial underestimation of core temperatures (e.g., <0°C in CanESM5 and GISS E2 1 H), and (2) Overestimated AW layer thickness with obviously downward shifted core depths. These challenges are particularly pronounced in the western Eurasian Basin influenced by the Fram Strait branch (one of two primary AW inflow pathways) compared to the eastern Eurasian Basin and the Amerasian Basin sector. Observational data reveal maximum temperatures (1.65°C) at 250 m depth in the western Eurasian Basin, decreasing to 0°C at 800 m (Fig. 108a). However, all CMIP6 models show structural biases with temperature maxima averaging 500 m depth and underestimated vertical temperature gradients. In contrast, E3SMv2-MPAS can successfully reproduces observed vertical temperature structure, matching the observed 250 m temperature maximum depth and maintaining temperature decline to 0°C at 1000 m depth. Despite a ~1°C core temperature overestimation and 200 m layer thickness bias, its temperature profile RMSE is (0.448) significantly outperforms other CMIP6 models.



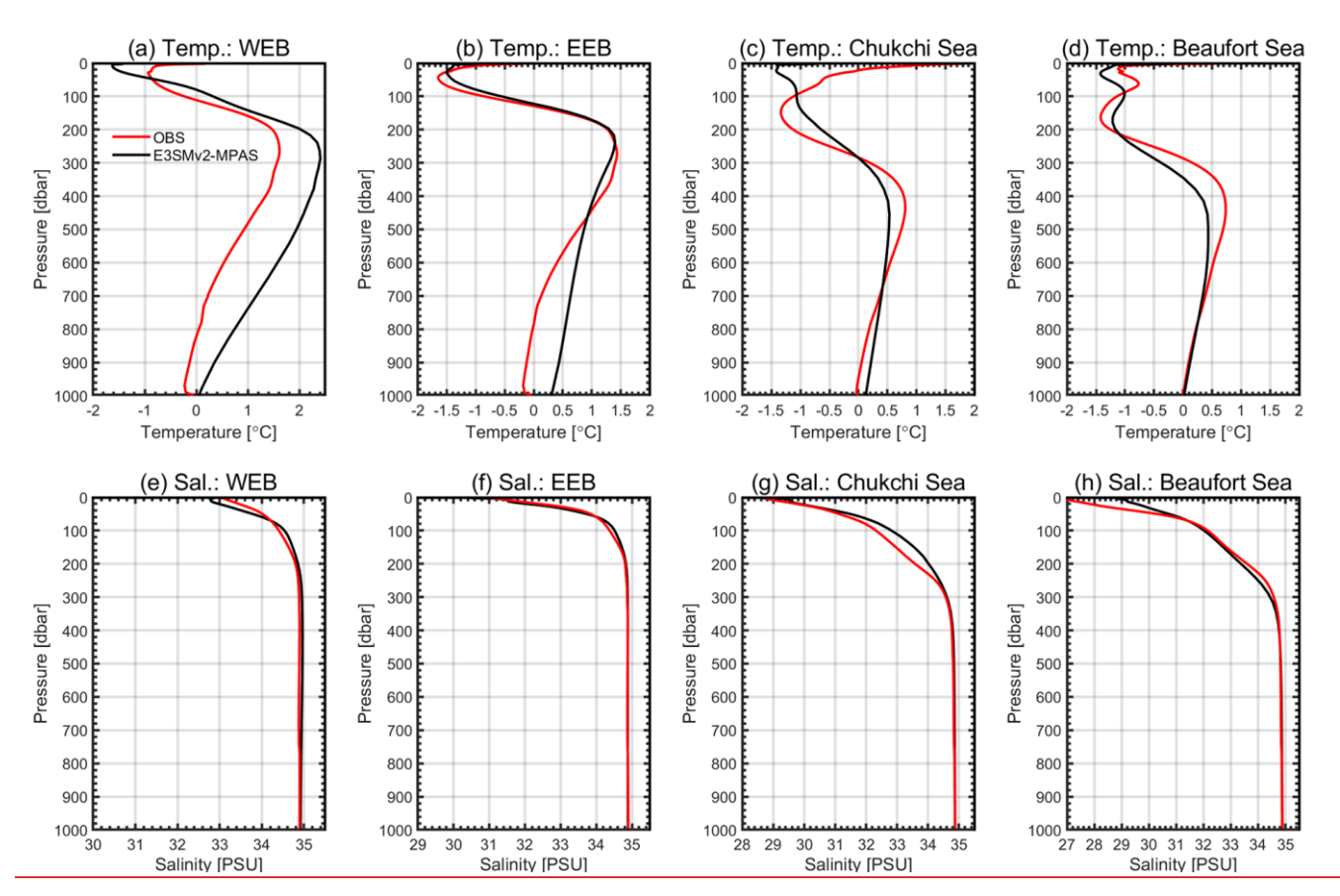


Figure 108. (a-d) 1995-2014 climatological mean temperature profiles from observations (Muilwijk et al., 2023), and E3SMv2-MPAS, and the 13 models of CMIP6 (Muilwijk et al., 2023). (e-h) The same as panels (a-d) but for salinity profiles. Basins: the Wwestern Eurasian (WEB; a/e), the Eeastern Eurasian (EEB; b/f), the Chukchi Sea (c/g), the Beaufort Sea (d/h).

530

Observational spatial heterogeneity shows progressive temperature core reductions (1.6°C \rightarrow 1.4°C \rightarrow 0.87°C \rightarrow 0.76°C) and deepening core depths (250 m \rightarrow 290 m \rightarrow 400 m \rightarrow 420 m) from the western Eurasian Basin to the Beaufort Sea (Fig. 108a-d). CMIP6 models fail to capture these spatial gradients, exhibiting homogeneous vertical structures. E3SMv2-MPAS maintains systematic temperature overestimation (\sim 1°C in the western Eurasian Basin, \sim 0.3°C in the Chukchi Sea and the Beaufort Sea-0.5°C average) while successfully reproducing spatiotemporal evolution of vertical thermal structures. In salinity simulations, systematic underestimation is observed across CMIP6 models within the upper 500 m (Fig. 8e-h). E3SMv2-MPAS demonstrates optimal salinity profile fitting capability through observational agreement starting from 200–300 m depth, as evidenced by the western Eurasian Basin RMSE of 0.204.

Regional evaluations confirm E3SMv2-MPAS's optimal performance across key metrics: the western Eurasian Basin (temperature RMSE=0.448, salinity RMSE=0.204; Table 2), the eastern Eurasian Basin (0.344, 0.356), the Chukchi Sea (0.686, 0.302), and the Beaufort Sea (0.349, 0.811). Notably, IPSL-CM6A-LR marginally outperforms E3SMv2-MPAS in

the eastern Eurasian Basin and the Beaufort Sea salinity simulations, primarily due to surface salinity overestimation in E3SMv2-MPAS.

540

Table 2. Root mean square errors (RMSE) for temperature (Temp.; °C) and salinity (Sal.; PSU) in 0–1000 m vertical profiles from E3SMv2 MPAS and 13 CMIP6 models (Muilwijk et al., 2023), evaluated against observation (Muilwijk et al., 2023) in four regions: the Western Eurasian Basin, the Eastern Eurasian Basin, the Chukehi Sea, and the Beaufort Sea. Performance ranking: * indicates lowest RMSE per basin/variable, underlined values denote second-lowest.

	Western Eurasian Basin		Eastern Eur	asian Basin	Chukchi Sea		Beaufort Sea	
	Temp.	Sal.	Temp.	Sal.	Temp.	Sal.	Temp.	Sal.
E3SMv2-MPAS	0.448*	0.204*	0.344*	<u>0.356</u>	0.686*	0.302*	0.349*	0.811
BCC-CSM2-MR	0.742	1.711	0.700	1.842	1.088	0.784	0.996	0.922
CAMS-CSM1-0	0.692	2.276	0.635	2.263	0.913	1.094	0.916	1.007
CESM2	0.804	0.717	0.672	1.027	<u>0.784</u>	<u>0.635</u>	0.760	0.958
CanESM5	1.497	1.389	1.317	0.698	1.254	0.739	1.047	1.307
GFDL-CM4	0.875	0.296	0.903	1.226	0.941	1.206	0.730	2.135
GFDL-ESM4	0.641	0.449	0.827	0.787	1.011	1.389	0.705	2.195
IPSL-CM6A-LR	<u>0.620</u>	1.389	<u>0.584</u>	0.256*	0.830	1.873	<u>0.485</u>	0.562*
GISS E2 1 H	1.320	0.795	1.365	1.119	1.381	1.075	1.183	1.946
MIROC6	1.070	0.790	0.780	0.890	0.905	1.054	0.606	1.642
MPI-ESM1-2-HR	0.795	0.856	0.687	1.200	0.833	0.693	0.564	1.309
MRI-ESM2-0	0.839	0.556	0.768	0.930	0.913	1.198	0.701	1.817
NorESM2-LM	0.745	0.819	0.904	1.040	0.884	0.694	0.625	1.220
UKESM1-0-LL	1.022	1.134	1.102	1.076	1.278	1.444	0.883	2.122

545

550

Comprehensive analysis of higher-resolution CMIP6 models reveals common thermohaline simulation biases (Fig. 8). To evaluate resolution sensitivity in Arctic Intermediate Water simulations, the assessment framework is extended to five resolution-matched model pairs from OMIP2 (Wang et al., 2024; see Table 1). Thermohaline profile characteristics in the Eurasian and Amerasian Basins are systematically compared between high/low-resolution model pairs (solid/dashed lines), E3SMv2-MPAS, and WOA23 data (Locarnini et al., 2024; Reagan et al., 2024) to clucidate ocean model grid configuration impacts (Fig. 9). Low-resolution models exhibit persistent CMIP6 systematic biases, while their high-resolution counterparts (excluding IAP-LICOM-6.8km) demonstrate improved intermediate water core temperature and vertical structure

simulations. High-resolution models successfully reproduce observed zonal gradients showing temperature maxima decreasing from the Eurasian Basin (1.3°C@250 m) to the American Basin (0.7°C@400 m), confirming resolution enhancement benefits for occanic frontal processes. In the Eurasian Basin where simulation biases are most pronounced, the majority of high-resolution models — with the exception of E3SMv2-MPAS (10 km) and FESOM variants (4.5/24 km) — continue to exhibit overestimated AW layer thickness. WOA23 observations indicate temperature decline to 0°C at 800 m depth, whereas most models maintain —0.5°C at 1000 m (Fig. 9a). This persistent discrepancy demonstrates that resolution enhancement alone remains insufficient to fully resolve key technical bottlenecks in Arctic Intermediate Water simulations. Notably, E3SMv2 MPAS and FESOM models exhibit breakthrough performance (Table 3). Despite comparable resolutions to other high-resolution models (e.g., ACCESS MOM 9 km, FSU HYCOM 32 km), unstructured mesh configurations enable refined representation of key hydrographic gateways like the Fram Strait. Compared to tripolar grid models suffering numerical dissipation near complex constlines, variable mesh designs achieve reduced the Eurasian Basin temperature errors under equivalent computational resources. Model grid type and computational efficiency exhibit nonlinear relationships. Unstructured meshes (FESOM/MPAS) permit dynamic optimization through localized refinement in critical regions (e.g., AW intrusion pathways). This targeted refinement strategy provides new technical approaches for Arctic ocean modeling, particularly under accelerating Atlantification processes.

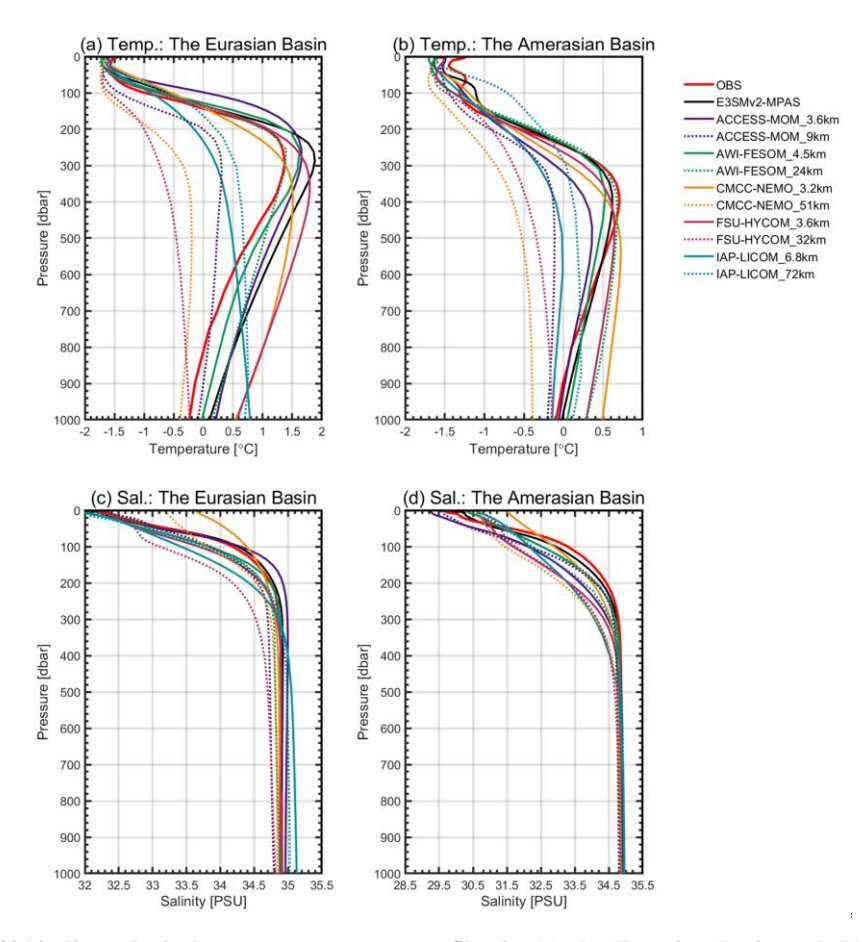


Figure 9. (a-b) 1995-2014 climatological mean temperature profiles in (a) the Eurasian Basin and (b) the Amerasian Basin570 Observations (WOA23; red), E3SMv2-MPAS (black), OMIP2 models (Wang et al., 2024; dashed: low-resolution, solid: highresolution), (e-d) The same as panels (a-b) but for salinity profiles.

Table 3. Root mean square errors (RMSE) for temperature (Temp.; °C) and salinity (Sal.; PSU) in 0-1000 m vertical profiles from E3SMv2-MPAS and 5 OMIP2 model pairs (Wang et al., 2024), evaluated against WOA23 in the Eurasian Basin and the Amerasian Basin. Performance ranking: * indicates lowest RMSE per basin/variable, underlined values denote second-lowest.

	Eurasia	n Basin	Amerasian Basin		
	Temp.	Sal.	Temp.	Sal.	
E3SMv2-MPAS	0.223*	0.130*	0.143*	0.219*	
ACCESS-MOM_3.6km	0.437	0.202	0.217	0.663	
ACCESS-MOM_9km	0.583	0.208	0.423	0.557	
AWI-FESOM_4.5km	0.236	0.205	0.207	<u>0.390</u>	
AWI-FESOM_24km	0.230	0.187	0.253	0.397	

CMCC-NEMO_3.2km	0.453	0.762	0.276	1.055
CMCC-NEMO_51km	0.869	0.600	0.558	0.875
FSU-HYCOM_3.6km	0.409	0.240	0.186	0.719
FSU-HYCOM_32km	1.012	0.442	0.485	0.797
IAP-LICOM_6.8km	0.716	0.457	0.346	0.882
IAP-LICOM_72km	0.435	0.319	0.456	0.716

Following systematic benchmarking against CMIP6/OMIP2 multi-resolution models, we investigate parameterization sensitivity within the same coupled framework (E3SM). By comparing mesoscale eddy parameterization schemes between E3SMv1 and v2 (as detailed in Section 2.2.3), we dissect their impacts on simulation fidelity and elucidate underlying mechanism. Comparative assessments of E3SM Arctic OSI (E3SMv1; Veneziani et al., 2022) and E3SMv2 MPAS (both 60to10 km) are performed across the Eurasian Basin, the Amerasian Basin, and sub-regions (Fig. 10). E3SMv2 MPAS demonstrates improved temperature vertical structure simulations (Fig. 10a-f), reducing Eurasian Basin core temperature overestimation from 13°C to 0.5°C and correcting 100 m core depth shoaling. Optimized mesoscale transport parameterization better represents turbulent mixing effects on water mass structure. For salinity, E3SM Arctic OSI exhibits 0.7 PSU biases above 200 m in the Eurasian Basin, reduced to -0.13 PSU in E3SMv2-MPAS (Fig. 10g). This enhancement likely stems from the refined vertical mixing scheme in E3SMv2-MPAS, which better captures Arctic halocline dynamics. Notably, E3SM Arctic OSI outperforms E3SMv2 MPAS in simulating sub-maximum temperature gradients (500–1000 m layer), with the Eurasian Basin RMSE reduced by 65% (0.17 vs. 0.49 in v2). This regression is attributed to excessive subsurface gradient smoothing in E3SMv2-MPAS caused by persistent moderate diffusion at 10 km Arctic resolution.

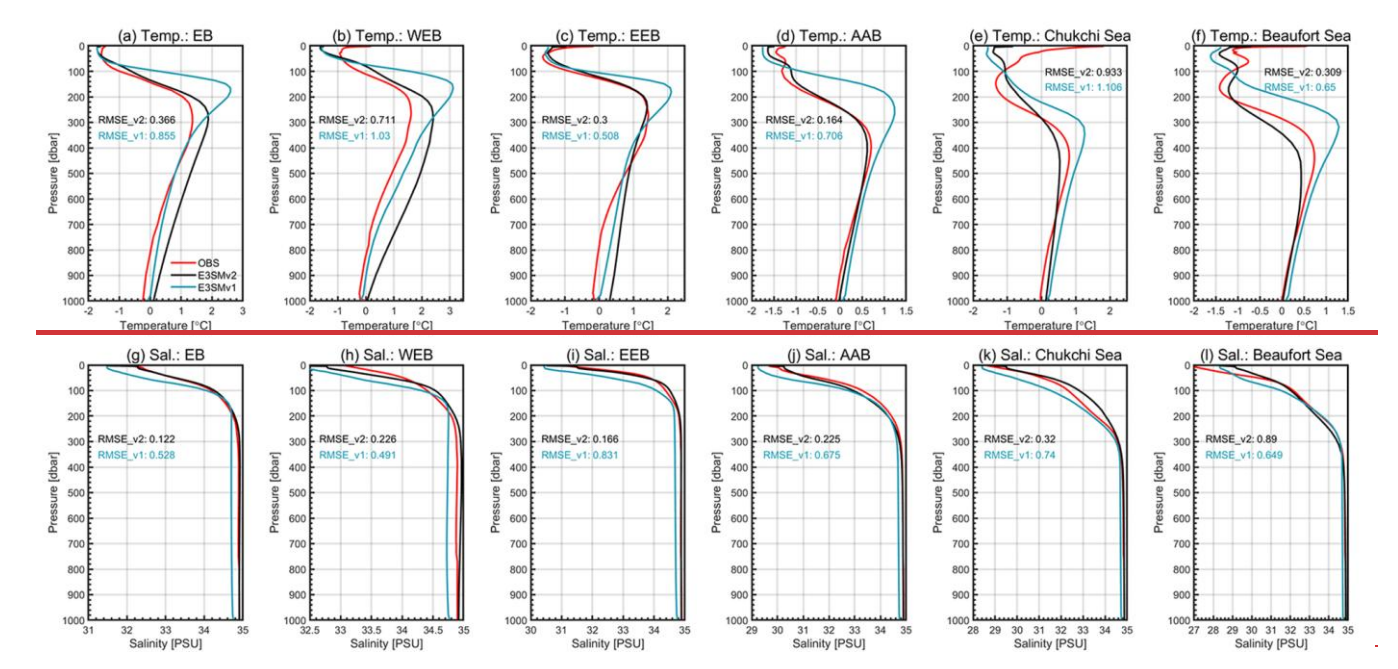


Figure 10. (a f) 2005-2014 climatological mean temperature profiles: Observations (WOA23 for EB/AAB; observation from Muilwijk et al., 2023 for WEB/EEB/Chukehi/Beaufort; red lines), E3SMv2-MPAS (black lines), E3SM-Aretic OSI (Veneziani et al., 2022; blue lines). (g l) The same as panels (a f) but for salinity profiles. Basins: the Eurasian Basin (EB, a/g), the Western Eurasian Basin (WEB, b/h), the Eastern Eurasian Basin (EEB, e/i), the Amerasian Basin (AAB, d/j), the Chukehi Sea (e/k), the Beaufort Sea (f/l).

600

605

Physical parameterization upgrades and resolution enhancement demonstrate synergistic effects. E3SMv2 MPAS addresses CMIP6/OMIP2 intermediate water simulation challenges through improved subgrid parameterization and the inherent advantages of unstructured meshes. The fundamental limitation of traditional eddy parameterization in variable resolution meshes is revealed: complete GM deactivation (κ=0) causes structural distortions, while moderate diffusion (κ=300 m² s⁻¹) induces over smoothing. FESOM_4.5km's superior temperature depth relationships suggest potential solutions through MPAS resolution increases or parameterization optimization via neural networks. Opposing regional biases (Eurasian overestimation/Amerasian underestimation) indicate current parameterizations lack universality across Arctic dynamical regimes, highlighting critical development pathways for next-generation models.

In order to systematically assess model capabilities in representing multi-scale Arctic thermal variations, an inter-decadal three-dimensional thermohaline evolution framework is established. Depth-time section comparisons between E3SMv2-MPAS and EN.4.2.2 (Good et al., 2013) are conducted to analyze spatiotemporal heterogeneity in Arctic oceanic thermal structures (Fig. 11).

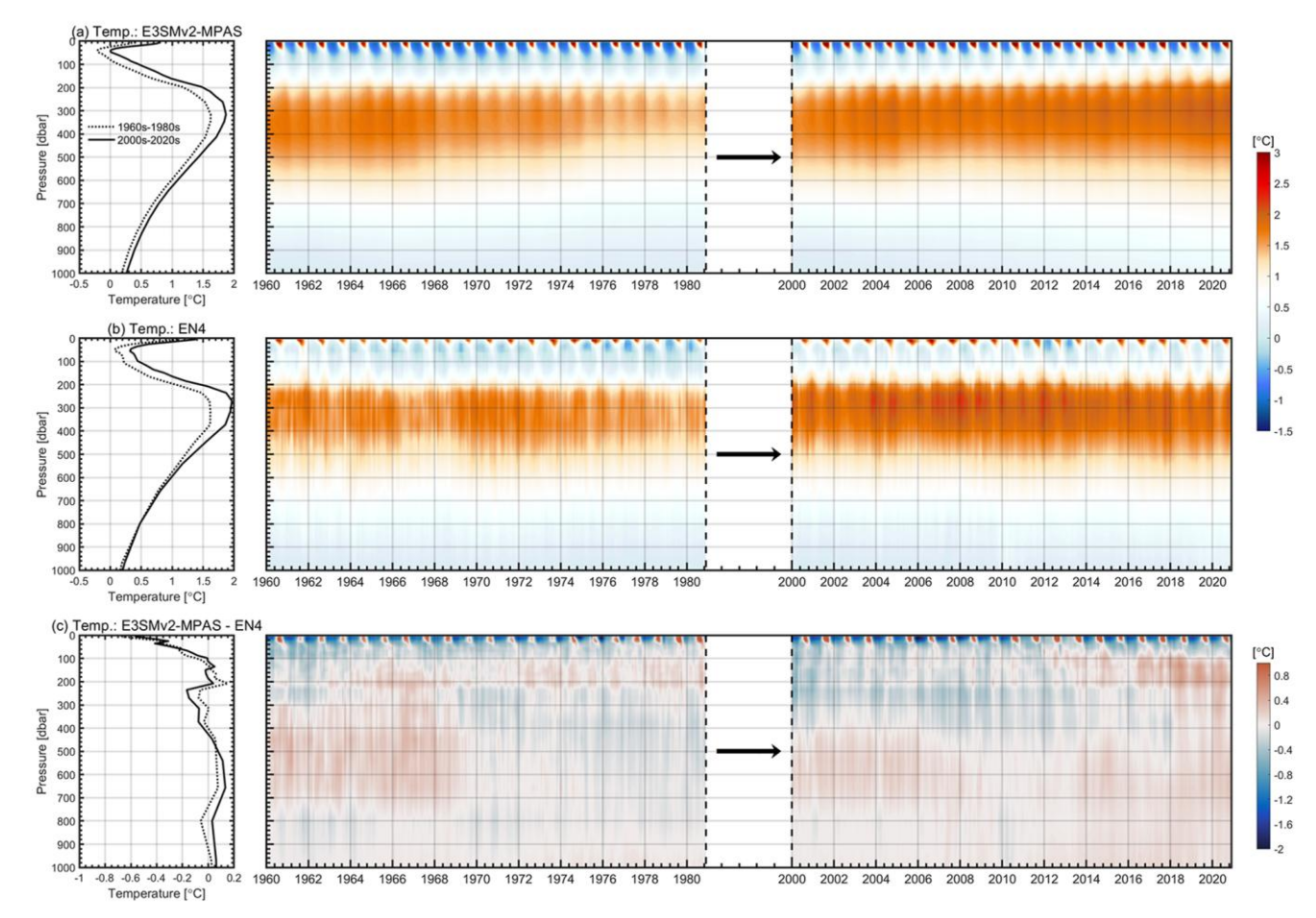


Figure 11. For the Arctic Basin, (a) E3SMv2-MPAS simulated temperature profiles (0–1000 m): 1960–1980 climatology (dashed) vs. 2000–2020 climatology (solid). Right: Hovmöller diagram of depth-time evolution (1960–1980 and 2000–2020). (b) The same as 610 panel (a) but for EN.4.2.2. (c) The same as panel (a) but for E3SMv2-MPAS minus EN.4.2.2 differences.

E3SMv2-MPAS successfully reproduces the solar radiation-driven seasonal thermal cycle observed in EN.4.2.2 (Fig. 11). Monthly thermohaline profiles (depth-month coordinates) in the upper 500 m of the Eurasian Basin better illustrate radiation-dominated seasonal characteristics: summer (June–August) surface temperature peaks coincide with salinity minima from meltwater inputs, while winter (December–February) shows sub-freezing temperatures (<-1.8°C) and salinity recovery (Fig. 12). These core seasonal features are accurately captured, validating high-precision surface flux representation.

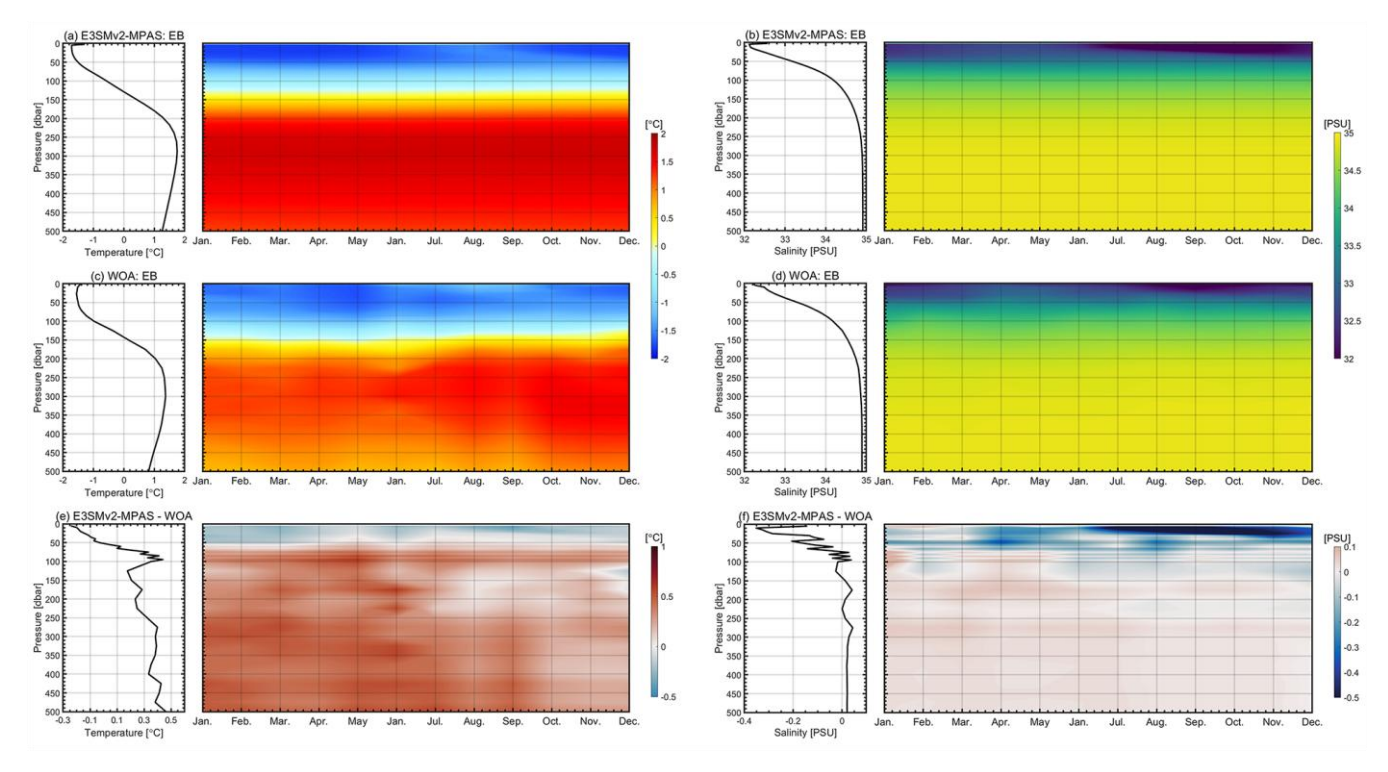


Figure 12. (a-b) E3SMv2-MPAS simulated 1995-2020 climatological mean (left) temperature and (right) salinity profiles (0-500 m) in the Eurasian Basin (EB), with Hovmöller diagrams of monthly variability. (c-d) The same as panels (a-b) but for WOA23. (e-f) The same as panels (a-b) but for model-observation differences (E3SMv2-MPAS minus WOA23).

E3SMv2-MPAS demonstrates exceptional multi-temporal simulation capabilities for AW dynamics (Fig. 11). Observations reveal stable AW core temperatures (~1.6°C) during 1960–1980, increasing to ~2°C in 2000–2020 with core shallowing from 350 m to 300 m in the whole Arctic Basin (Fig. 11b). E3SMv2-MPAS accurately reproduces both the ~0.4°C warming magnitude and ~50 m vertical migration (Fig. 11a). However, regional-specific biases emerge in seasonal variability simulations (Fig. 12). EN.4.2.2 identifies semi-annual signals in the 200–500 m layer of the Eurasian Basin (September–November peaks at ~1.5°C; Fig. 12c), linked to winter Atlantification intensification. E3SMv2-MPAS fails to capture this seasonality, producing persistent warm biases in 200–400 m layers with overestimated spring–summer core temperatures (0.5–0.8°C; Fig. 12e). This discrepancy may be attributed to the GM parameterization scheme, which models mesoscale eddy effects on heat and salt redistribution through bolus advection and Redi diffusion. In general, the Arctic winter features greater mixed layer depth and weaker stratification due to brine rejection during sea ice formation and wind-driven stirring (Peralta-Ferriz and Woodgate, 2015). These processes promote eddy penetration, increasing the efficiency of vertical heat transport. In contrast, strengthened stratification in summer restricts the vertical scale of eddies and reduces heat transfer. However, the GM scheme employs a fixed diffusion coefficient, which prevents it from capturing the seasonal variability modulated by stratification changes. A systematic validation framework uncovers the multi-tiered optimization characteristics of E3SMv2-MPAS, demonstrating superior surface layer accuracy alongside relatively excellent

intermediate depth representations. Nevertheless, inherent constraints of current parameterization schemes under polar stratification conditions lead to persistent model-data discrepancies, particularly manifested in seasonal phase mismatches. This finding highlights the need to develop improved turbulence models based on energy transfer principles (Canuto et al., 2001; Smagorinsky, 1963), which would better connect processes across different scales.

We further investigate the decadal-scale thermohaline variability across Arctic basins. The results reveal regional heterogeneity in temperature and salinity trends (Fig. 13), likely modulated by differential ocean ice feedbacks and cross-basin transport dynamics. Inter-decadal comparisons (1970s vs. 2000s–2020s; Muilwijk et al. (2023)) reveal pan-Arctic synchronous warming across the Eurasian Basin sectors and the Amerasian sub-regions (Fig. 13e–h). However, E3SMv2-MPAS underestimates the warming in the Amerasian Basin (0.1–0.5°C biases; Fig. 13c–d and g–h), indicating limitations in AW transport pathways and heat redistribution.

640

645

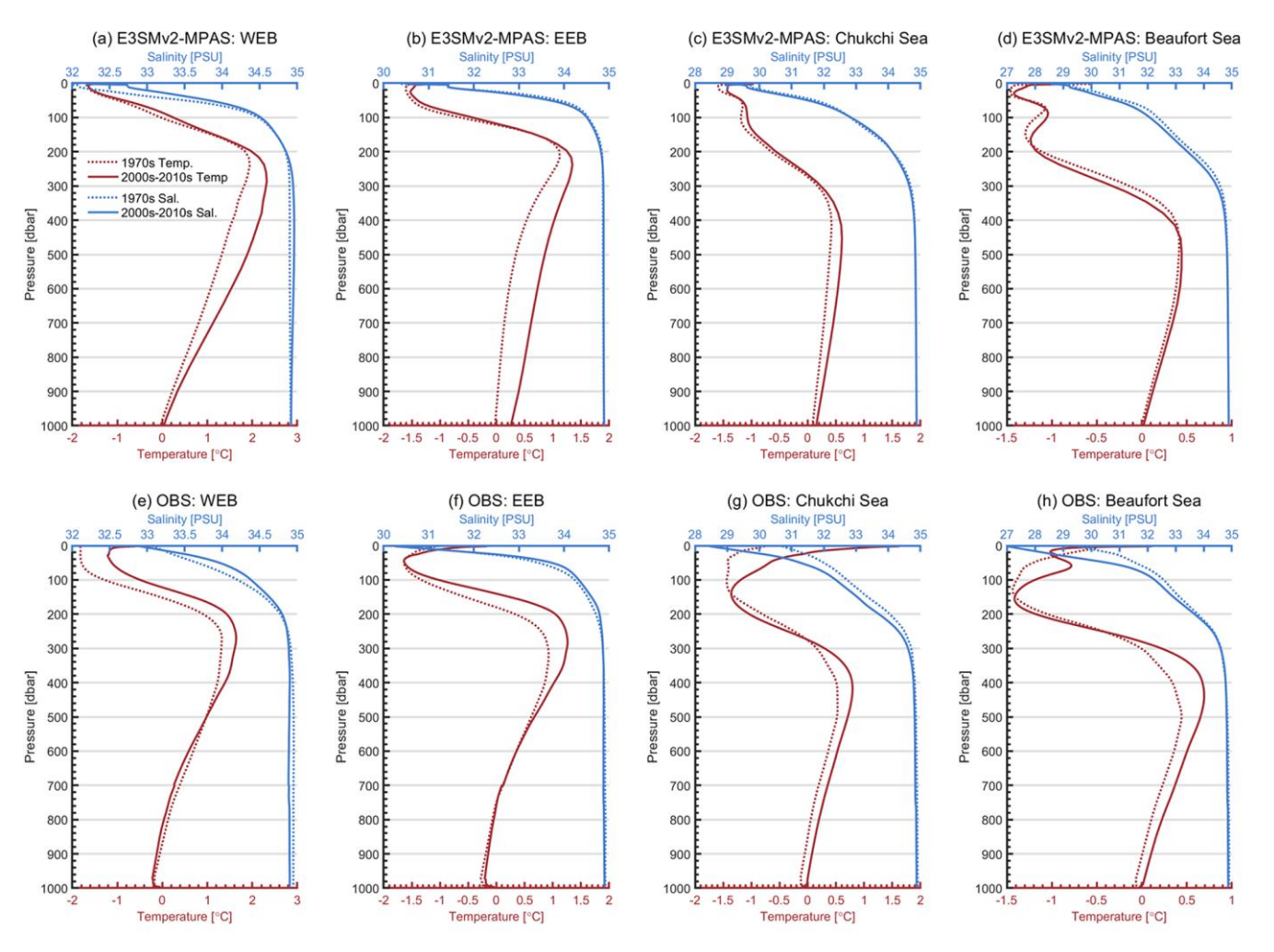


Figure 13. (a-d) Vertical profiles of climatological mean temperature (red curves) and salinity (blue curves) in the <u>Ww</u>estern Eurasian Basin (WEB₂₇ a), the <u>Ee</u>astern Eurasian Basin (EEB₂₇ b), the Chukchi Sea (c), and the Beaufort Gyre (d) from E3SMv2-

MPAS: dashed lines denote 1970s (1971–1979), solid lines represent 2000s–2010s (2001–2019). (e-f) Corresponding observational profiles from Muilwijk et al. (2023) with identical temporal averaging.

In the Eurasian Basin upper layers (~100–450 m; Fig. 13a–b and e–f), observations show dual-mode thermal evolution: shallow warming above temperature cores (100–250 m) contrasts with systematic warming below (250–450 m). Model simulations exhibit spatial heterogeneity: 0.2±0.1°C underestimation of shallow warming contrasts with excessive vertical response ranges (250–1000 m vs. observed 250–450 m). Notably, simulated AW layer thickening in the eastern Eurasian Basin during 2000s–2010s lacks observational support (Fig. 13b and f). These discrepancies may be partly attributed to biases in the representation of vertical processes. As indicated by sensitivity experiments such as those of Liang & Losch (2018), enhanced vertical mixing could promote upward heat transport from AW, potentially causing cooling at intermediate depths (200–900 m). Our model uses a relatively low background diffusivity (1.0×10-5 m² s-1), which remains constant across time periods despite evidence that Arctic amplification and Atlantification in the 2000s–2010s (Polyakov et al., 2017, 2025; Rantanen et al., 2022; Richards et al., 2022; Shu et al., 2022) may have strengthened vertical mixing compared to the 1970s. The model's failure to represent this temporal increase in mixing efficiency might have limited upward heat transfer, confining warming mainly to intermediate and deeper layers – consistent with the underestimation of shallow warming and exaggerated deep response seen in our simulations.

In the Chukchi Sea-Amerasian Basin side, observations indicate basin-wide warming from core layers to AW bottom (~1000 m), with the Chukchi Sea-showing ΔT=0.2±0.1°C (Fig. 13c-d and g-h). While successfully reproducing Chukchi thermal trends, E3SMv2-MPAS-the model exhibits systematic Beaufort Sea deviations. Salinity changes primarily occur in the upper 300 m of the Amerasian Basin (the Chukchi and Beaufort Seas; observed ΔS=-0.3±0.2 PSU), with the model failures in capturing the freshening of the Chukchi Sea and underestimation of trends in the shallow-layer (<80 m) of the Beaufort Sea. The simulated salinity biases may be related to the use of an inappropriately high and constant isopycnal diffusion coefficient (κ=300 m² s⁻1) in the GM parameterization. This high diffusion coefficient likely results in excessively strong along-isopycnal mixing, which oversmooths horizontal salinity gradient fronts formed by freshwater accumulation (e.g., from melting ice and increased runoff). During the 1970s, when background freshwater signals were relatively weak, the effect of strong diffusion was less pronounced. However, under the strongly increased freshwater input in the 2000s-2010 (Polyakov et al., 2013; Wang et al., 2019), the persistently high κ value continuously and excessively diffused the simulated upper-layer low-salinity anomalies, hindering their realistic accumulation and maintenance in the basin upper layer. As a result, the model significantly underestimates the magnitude of decadal freshening observed in the region.

E3SMv2 MPAS demonstrates significant regional dependence in simulating interdecadal thermohaline structure changes across Arctic basins. Systematic biases persist between model outputs and observational data, particularly in AW layer thickness evolution, vertical extent of subsurface warming processes, and strength of surface freshening signals. These discrepancies likely originate from suboptimal parameterization schemes for key physical processes such as mesoscale eddy activities and shelf basin interactions.

AW demonstrates systematic cooling and freshening (temperature and salinity reduction) during its transport from the Eurasian to the Amerasian Basin (Fig. 108), a transformation likely modulated by baroclinic adjustment processes in the inter-basin transition zone. These processes known to govern cross-basin material-energy exchange (Aksenov et al., 2016). necessitate a three dimensional thermohaline diagnostic approach. To this end, we'We analyze coordinated meridional sections along 145° W in (the Amerasian Basin) and 70° E in (the Eurasian Basin) to, constructing a unified framework to evaluate spatiotemporal variability in access variability in AW properties across space (Fig. 14). WOA23-based comparisons confirm E3SMv2-MPAS's capability in reproducing inter-basin gradient characteristics through three key aspects: (1) AW thermal attenuation: Successful simulation of core temperature decreases from the Eurasian to the -Amerasian Basin, replicating thermodynamic dissipation processes; (2) Stratification depth displacement: Realistic representation of westwarddecreasing upper boundary depths matching slope current adjustments; (3) Surface freshwater transport effects: Accurate reproduction of the surface salinity depression in the Amerasian Basin relative to the Eurasian Basin, validating appropriate parameterization of Pacific-origin freshwater influx mechanisms. Persistent thermal biases in the Eurasian Basin emerge in 145° W sections, with maximum +2°C warm deviations in 100-500 m core layers (Fig. 14e). These discrepancies may originate from overestimation of the Fram Strait heat fluxes or inadequate parameterization of mesoscale mixing. Despite absolute temperature biases, maintained meridional heat transport gradients confirm fundamental physical framework validity for large-scale advection processes.

685

690

695

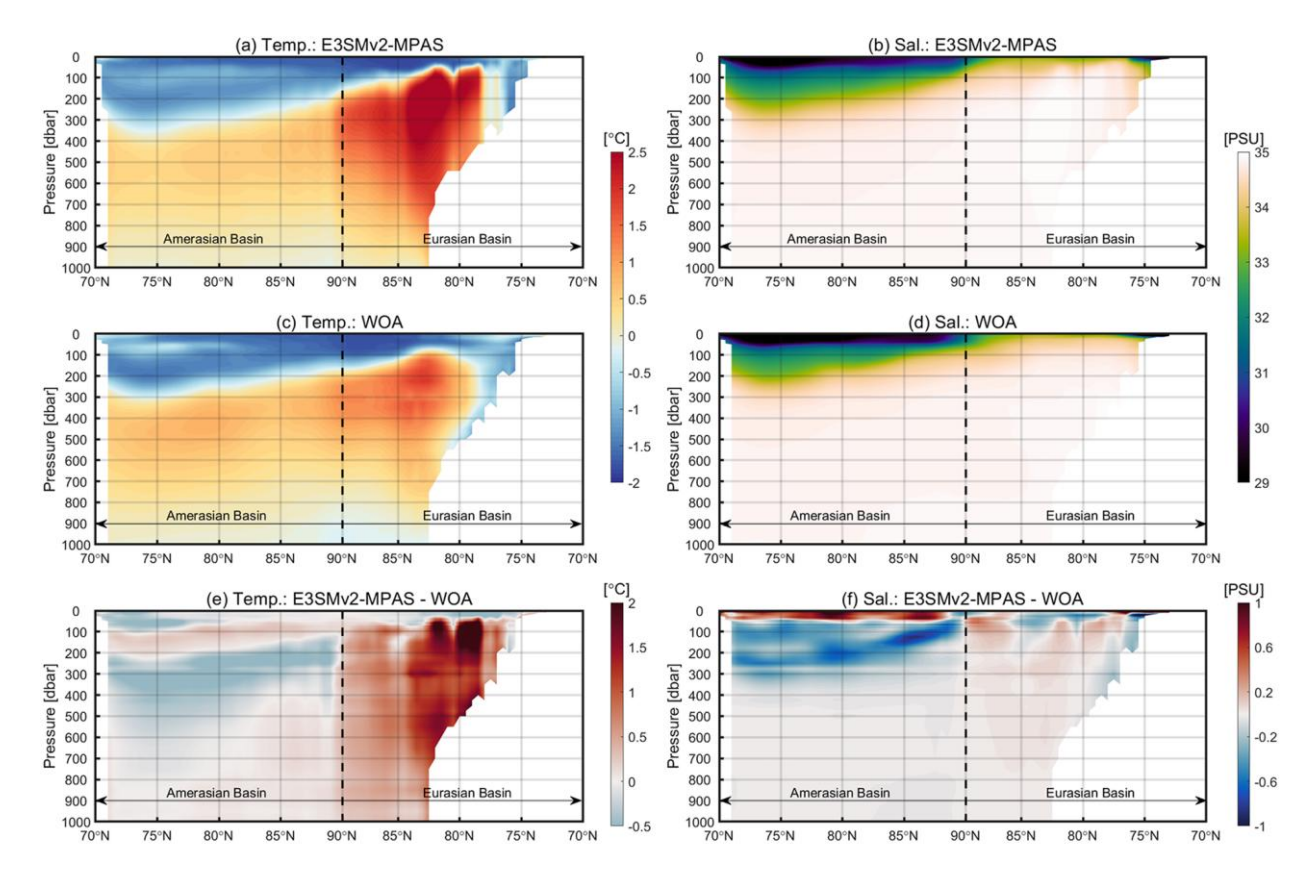


Figure 14. (a-b) E3SMv2-MPAS simulated 1995-2020 climatological (left) temperature and (right) salinity distributions along the 145°_W-70°_E transect (location mapped in Fig. 1b). (c-d) The same as panels (a-b) but for WOA23. (e-f) The same as panels (a-b) but for the model-observation differences (E3SMv2-MPAS minus WOA23).

3.4 Freshwater content spatiotemporal variability

705

710

The Arctic Ocean constitutes a major freshwater reservoir within the global climate system. Since the mid-1990s, the freshwater content (FWC) in the Arctic Ocean has exhibited a marked increasing trend, primarily driven by persistent anticyclonic atmospheric forcing over the Beaufort Gyre region (1997–2018) and the reduction of Arctic sea ice (Proshutinsky et al., 2019; Wang et al., 2024). This excess freshwater is exported into the North Atlantic through Fram Strait and Davis Strait (Wang et al., 2019), eventually reaching convection regions in the Labrador and Greenland–Iceland–Norwegian Seas. These areas are critical for the formation of global deep waters, which act as a key driver of large-scale ocean circulation systems, including the Atlantic Meridional Overturning Circulation (AMOC) (Arzel et al., 2007). The southward transport of freshwater may influence circulation dynamics by reducing seawater density and suppressing vertical mixing (Haine et al., 2023). Furthermore, Arctic freshwater variability significantly influences ecosystem structure and function (Proshutinsky et al., 2019). Therefore, accurately assessing the freshwater content in the Arctic Ocean represents a central challenge in physical oceanography and climate dynamics, with major implications for understanding both climate variability and long-term change (Haine et al., 2023).

The FWC is defined as follows (Wang et al., 2024):

$$FWC = \int_{H}^{0} \frac{S_{ref} - S}{S_{ref}} dz, \tag{1}$$

where S denotes salinity, S_{ref} is the reference salinity – set to 34.8 psu, the mean Arctic Ocean salinity according to Aagaard and Carmack (1989) – and H represents the depth at which salinity equals S_{ref} .

Based on this formulation, we evaluate the spatial distribution of the multi-year mean (1995–2020; Fig. 15a–b) and decadal differences (2005–2014 vs. 1995–2004; Fig. 15c–d) of FWC as simulated by E3SMv2-MPAS, in comparison with observational data from WOA23. Additionally, we analyze the basin-wide averaged time series of FWC across the Arctic Ocean (Fig. 15e).

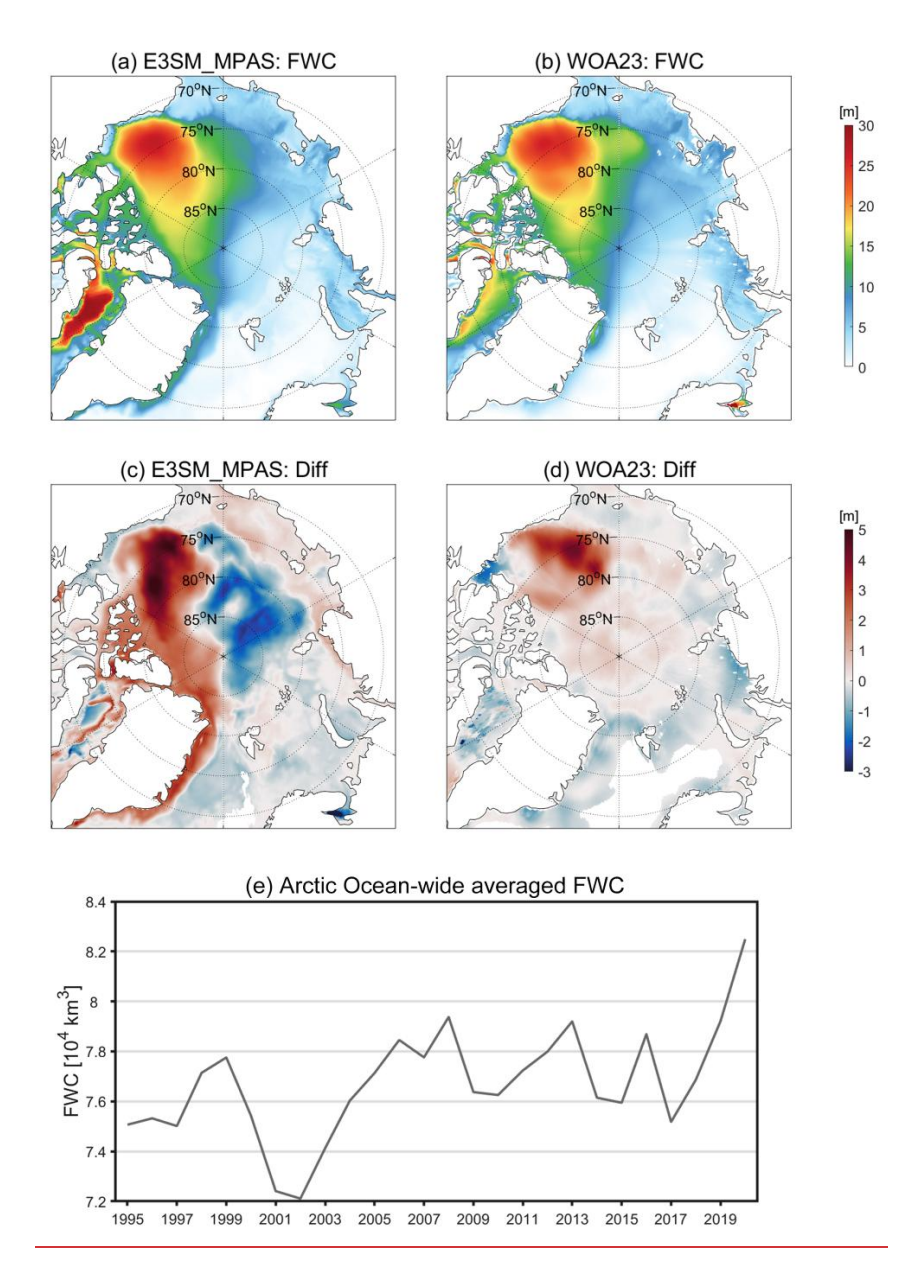


Figure 15. Spatial distribution and temporal evolution of FWC (in meters) in the Arctic Ocean. (a-b) Multi-year mean (1995–2020) FWC from (a) E3SMv2-MPAS and (b) WOA23. (c-d) Decadal difference in FWC (2005–2014 minus 1995–2004) from (c) E3SMv2-MPAS and (d) WOA23. (e) Time series of the Arctic Ocean-wide averaged FWC from E3SMv2-MPAS for the period 1995–2020.

As shown in Fig. 15a-b, E3SMv2-MPAS generally captures the spatial characteristics of Arctic FWC, such as the increase from the Eurasian Basin toward the Amerasian Basin and the maximum values located in the Beaufort Sea. However, the model overestimates FWC in the vicinity of Baffin Bay.

Observational results from WOA23 indicate a pronounced strengthening of FWC in the Beaufort Sea during 2005–2014 compared to 1995–2004. The model successfully reproduces this decadal change in that area (Fig. 15c–d). Nonetheless, E3SMv2-MPAS erroneously simulates a significant decrease in FWC across the Eurasian and Makarov Basins, where WOA23 shows a slight increase. Moreover, the model overestimates the increase in FWC along a pathway extending from the east of Greenland to the northern Canadian Archipelago and into the Canada Basin.

The time series of the total Arctic FWC (Fig. 15e) exhibits a fluctuating upward trend from 1995 to 2020. Polyakov et al. (2013) reported a notable acceleration in Arctic FWC accumulation during the 2000s, particularly between 2003 and 2010 – a trend that aligns with the sharp rise simulated by E3SMv2-MPAS between 2002 and 2008. Furthermore, Wang et al. (2019) noted a levelling off of the FWC growth trend after 2010, which is also captured by the model.

3.5 Gateway transports: volume, heat, and freshwater

735

760

Over the past decades, the Arctic climate system has undergone rapid changes, including shifts in sea ice, atmosphere, and ocean conditions (Landrum and Holland, 2020; Polyakov et al., 2005; Shu et al., 2022). These rapid changes are closely linked to the lateral exchanges of heat and freshwater across the boundaries of the Arctic (Von Schuckmann et al., 2020). The Arctic Ocean's connections to other oceans are defined by four major gateways (from east to west): Bering Strait, Fram Strait, Barents Sea Opening, and Davis Strait (Tsubouchi et al., 2024). These critical gateways not – as discussed in the previous section – serve as major pathways for freshwater export from the Arctic, which in turn influences global deepwater formation, large-scale circulation, and ecosystems, but also subject Arctic sea ice and ocean conditions to strong influences from Atlantic and Pacific water inflows. These impacts include modulating sea ice cover (Årthun et al., 2012, 2019; Docquier and Koenigk, 2021), ocean stratification (Veneziani et al., 2022), ecosystem (Woodgate and Peralta-Ferriz, 2021), ocean temperature (Barton et al., 2018), and freshwater content (Woodgate, 2018). Therefore, the accurate simulation of volume, heat, and freshwater transports through these four major gateways – including their interannual and decadal variability – is crucial. In this section, we evaluate the performance of the E3SMv2-MPAS in simulating these key exchanges through comparison with multi-source observational data.

The oceanic net volume transport (VT), heat transport (HT), and freshwater transport (FWT) through the key gateways—

Bering Strait, Fram Strait, Barents Sea Opening, and Davis Strait—are calculated as follows (Karpouzoglou et al., 2022; Shu et al., 2022; Wang et al., 2024):

$$VT = \int_{-H(\lambda)}^{0} \int_{\lambda_1(z)}^{\lambda_2(z)} V d\lambda dz, \tag{2}$$

$$HT = \rho_o c_p \int_{-H(\lambda)}^0 \int_{\lambda_1(z)}^{\lambda_2(z)} V(T - T_{ref}) d\lambda dz, \tag{3}$$

$$FWT = \int_{-H(\lambda)}^{0} \int_{\lambda_1(z)}^{\lambda_2(z)} V \frac{(S_{ref} - S)}{S_{ref}} d\lambda dz, \tag{4}$$

Here, V, T, and S denote velocity, potential temperature, and salinity, respectively; ρ_o is the seawater density; and c_p represents the specific heat capacity of seawater. The reference temperature T_{ref} is set to 0 °C, and the reference salinity S_{ref}

is defined as 34.8, corresponding to the mean salinity of the Arctic Ocean (Aagaard and Carmack, 1989). The integration is performed over the full depth H – defined as the bathymetry along the transect – and across the lateral extent λ of each strait. Units for VT, HT, and FWT are Sverdrup (Sv; 1 Sv=10⁶ m³ s⁻¹), Terawatt (TW), and km³ year⁻¹, respectively.

3.5.1 Bering Strait

765

Observational data from the Bering Strait between 2000 and 2018 (Woodgate and Peralta-Ferriz, 2021) reveal significant increasing trends in volume, heat, and freshwater transports (Fig. 16a–c). However, E3SMv2-MPAS fails to reproduce these overall trends. The discrepancies in volume and freshwater transports may be attributed to biases in the JRA55 reanalysis and river runoff forcing data (Wang et al., 2024). Although the model does not capture the increasing trends in volume and freshwater transports during 2000–2012, it successfully simulates the upward trends from 2012 to 2018, including interannual variability, with deviations generally within 0.2 Sv and 500 km³ year¹ (Fig. 16a and c). The similar interannual and decadal variability between simulated volume and freshwater transports indicates that the model accurately represents the mechanism whereby increased freshwater transport is primarily driven by volume transport (Woodgate and Peralta-Ferriz, 2021). For heat transport, the model also captures the rapid increasing trend observed after 2012 (Fig. 16b).

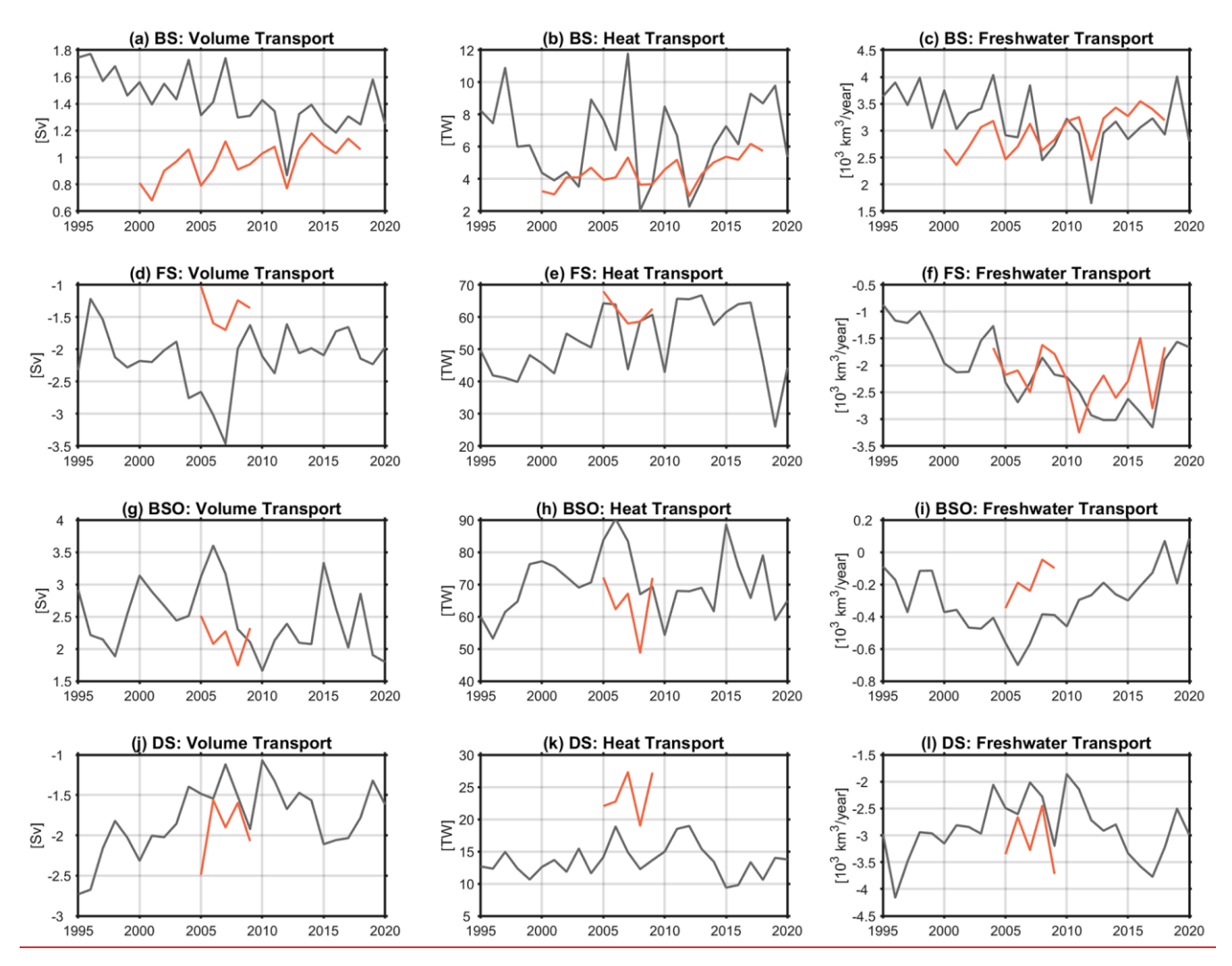


Figure 16. Time series of net (a, d, g, j) volume, (b, e, h, k) heat, and (c, f, i, l) freshwater transport through the (a-c) Bering Strait (BS), (d-f) Fram Strait (FS), (g-i) Barents Sea Opening (BSO), and (j-l) Davis Strait (DS) from 1995 to 2020. Black and red lines denote simulated results from E3SMv2-MPAS and observational estimates, respectively. Positive values represent transport into the Arctic Ocean, while negative values denote transport out of the Arctic Ocean. Observational data are from Woodgate and Peralta-Ferriz (2021) for BS; Tsubouchi et al. (2024) for volume and heat transport in FS; Karpouzoglou et al. (2022) for freshwater transport in FS; and Tsubouchi et al. (2024) for BSO and DS. The locations of the four straits are highlighted in green in Fig. 1b.

3.5.2 Fram Strait

780

785

A study by Schauer et al. (2004) show annual mean net volume transport through the Fram Strait between -4±2 Sv and -2±2 Sv during 1997–2000. Schauer et al. (2008) further indicate values of -2±5.9 Sv (1997–2002) and -2±2.7 Sv (2002–2006). Despite considerable uncertainties in observations, these estimates confirm that the simulated volume transport by E3SMv2-MPAS falls within a plausible range (Fig. 16d). Results from Tsubouchi et al. (2024) for 2005–2009 show that, although the model generally overestimates southward volume transport, it reproduces the interannual variability reasonably well (Fig.

16d). Observations indicate that the annual mean net heat transport increased from 16±12 TW in 1997 to 41±5 TW in 1999 (Schauer et al., 2004). In comparison, the model overestimates heat transport in 1997 but accurately captures both the pronounced increasing trend during 1997–1999 and the value in 1999 (Fig. 16e). Compared to observational data from 2005–2009 (Tsubouchi et al., 2024), the simulated heat transport values agree well in magnitude, and the model largely reproduces the initial decrease followed by an increase during this period. Moreover, the model successfully captures both the increasing trend and the magnitude of the observed southward freshwater transport through the Fram Strait from 2004 to 2017 (Karpouzoglou et al. (2022); Fig. 16f).

3.5.3 Barents Sea Opening

Between 2000 and 2009, the annual mean net volume and heat transports through the Barents Sea Opening were reported as 2.3 Sv and 70±5 TW, respectively (Smedsrud et al., 2013), which are generally consistent with the model simulations (Fig. 16g-h). E3SMv2-MPAS also successfully reproduces the decreasing trends in both volume and heat transport during 2005–2008, albeit with slight systematic overestimation. Observations indicate a pronounced decreasing trend in freshwater export through the Barents Sea Opening during 2005–2009 (Tsubouchi et al., 2024). While the model captures this trend, it overestimates the magnitude (Fig. 16i). Additionally, the mean freshwater transport through the Barents Sea Opening between 2000 and 2010 was -90±90 km³ year-1 (Haine et al., 2015), further supporting the model's tendency to overestimate freshwater export in this region.

3.5.4 Davis Strait

810

Observations from 2004 to 2010 report annual mean net volume and freshwater transports through the Davis Strait as -1.6±0.5 Sv and -2,900±190 km³ year¹, respectively (Curry et al., 2014). E3SMv2-MPAS simulations agree well with these values during the same period (Fig. 16j and l). The model accurately captures the increased freshwater export through the Davis Strait in the mid-to-late 2010s (particularly 2015–2017), which is influenced by Arctic-external atmospheric forcing affecting sea level variability (Wang et al. (2022); Fig. 16l). According to Wang et al. (2022), the freshwater export through the Davis Strait increased by over 1500 km³ year¹ between 2010 and 2017, a magnitude quantitatively reproduced by E3SMv2-MPAS. However, the simulated heat transport ranges from 13 to 19 TW during 2005–2009, underestimating the observed range of 19–27 TW (Tsubouchi et al. (2024); Fig. 16k).

5 4 Atlantic Water Llaver Sstates

4.1 Parametric Ccharacterization of Atlantic Water Ccore

As demonstrated in Section 3, model biases predominantly manifest in two critical parameters: AW core temperature (AWCT) and depth (AWCD). These metrics, defined as the maximum temperature within 150–900 m depth and its corresponding depth (Khosravi et al., 2022; Shu et al., 2022; Wang et al., 2024), are employed to evaluate E3SMv2-MPAS's

performance in reproducing spatiotemporal features of AW (Fig. <u>1745</u>). Observational AWCT/AWCD datasets from Richards et al. (2022) reveal successful model reproduction of baseline spatial gradients: decreasing AWCT and increasing AWCD from the Eurasian to the Amerasian Basin, though with marked regional heterogeneity (Fig. <u>15a17a</u>–d). Systematic overestimation of AWCT (+0.5°C) is identified in the western Eurasian Basin off-shelf regions (high-latitude sectors), potentially linked to biased inflow heat flux allocation in the Fram Strait. while Similar negative positive deviations (±_0.5°C) occur in the Beaufort Sea—maybe suggest inadequate Pacific inflow mixing parameterization. AWCD simulations demonstrate higher accuracy, with minor underestimation (ΔZ<100 m) in the eastern Eurasian Basin.

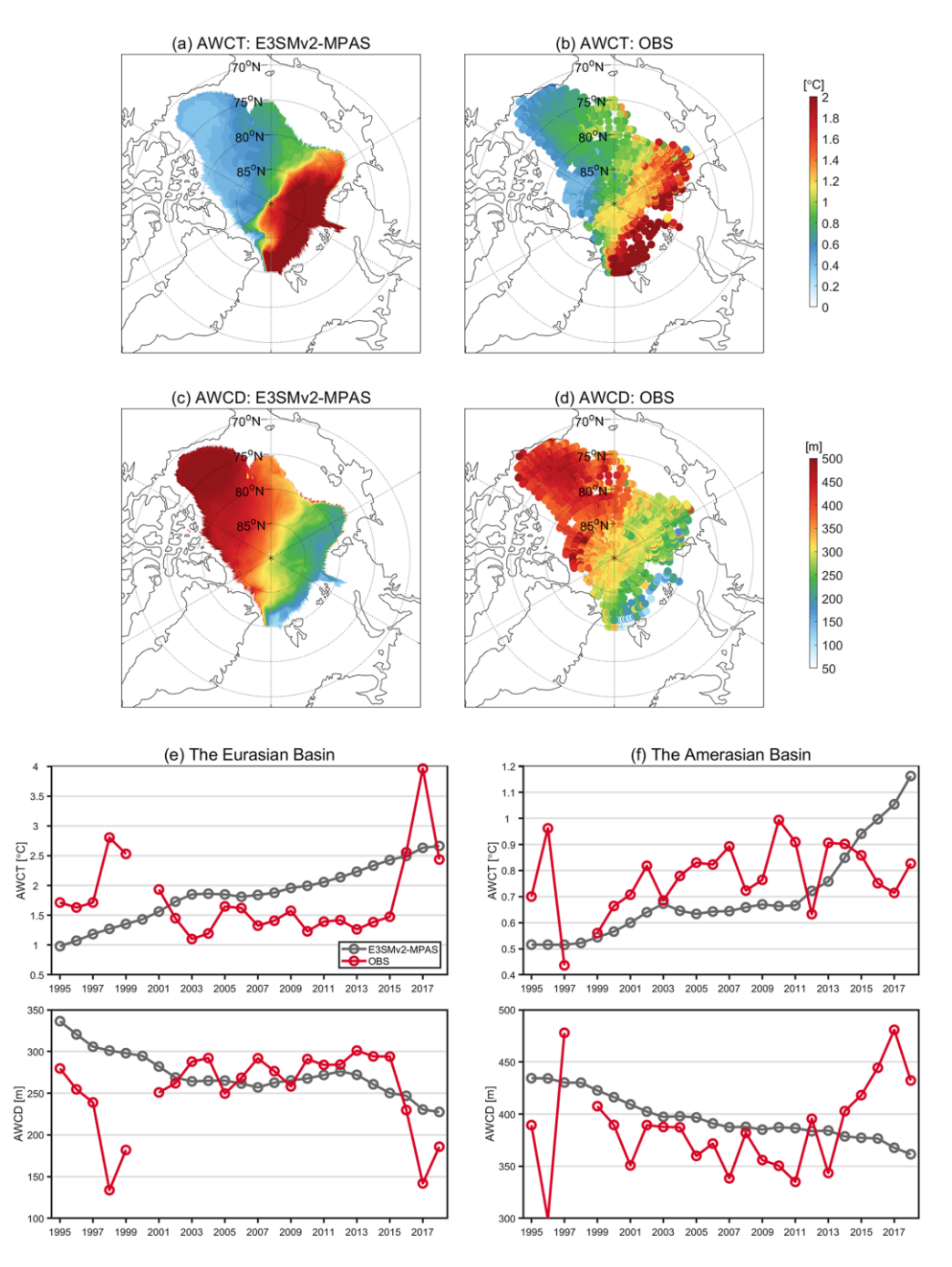


Figure 1715. (a-b) 1995-2018 climatological mean Atlantic Water Core Temperature (AWCT) spatial distributions: (a) E3SMv2-MPAS vs. (b) observation from Richards et al. (2022). (c-d) The same as panels (a-b) but for Atlantic Water Core Depth (AWCD). (e-f) Temporal evolution of basin-averaged AWCT (top row) and AWCD (bottom row) in the Eurasian Basin (e) and the Amerasian Basin (f): E3SMv2-MPAS (black) versus observations (red).

Interannual variability (1995–2018) is adequately captured through basin-averaged AWCT/AWCD magnitudes (Fig. <u>1745e-f</u>). <u>E3SMv2-MPAS successfully reproduces AWCT warming trends in both basins, AWCD shoaling in the Eurasian Basin, and 1995–2013 AWCD declines in the Amerasian Basin. However, post-2013 increases in AWCD in the Amerasian Basin remain unresolved. While demonstrating credibility in long-term trend simulations, model responsiveness to decadal-scale climatic shifts requires <u>boundary condition dynamization and mixing process</u>—<u>further</u> optimization — critical for predicting nonlinear Atlantification trajectories.</u>

835

840

845

Cross validation under the OMIP2 framework (Wang et al., 2024) reveals that among five resolution-varied model groups, only FESOM_4.5km, MOM_3.6km, and HYCOM_3.6km demonstrate high AWCT spatial pattern simulation skills (Fig. 16). FESOM_4.5km outperforms E3SMv2-MPAS (10 km) in representing the western Eurasian Basin shelf-basin gradients, but underperforms in the Amerasian Basin (Fig. 16b-c). Low-resolution models exhibit a systematic underestimation of AWCT, with FESOM_24km being the exception, reaffirming unstructured meshes' polar ocean modeling advantages (Fig. 16b-1).

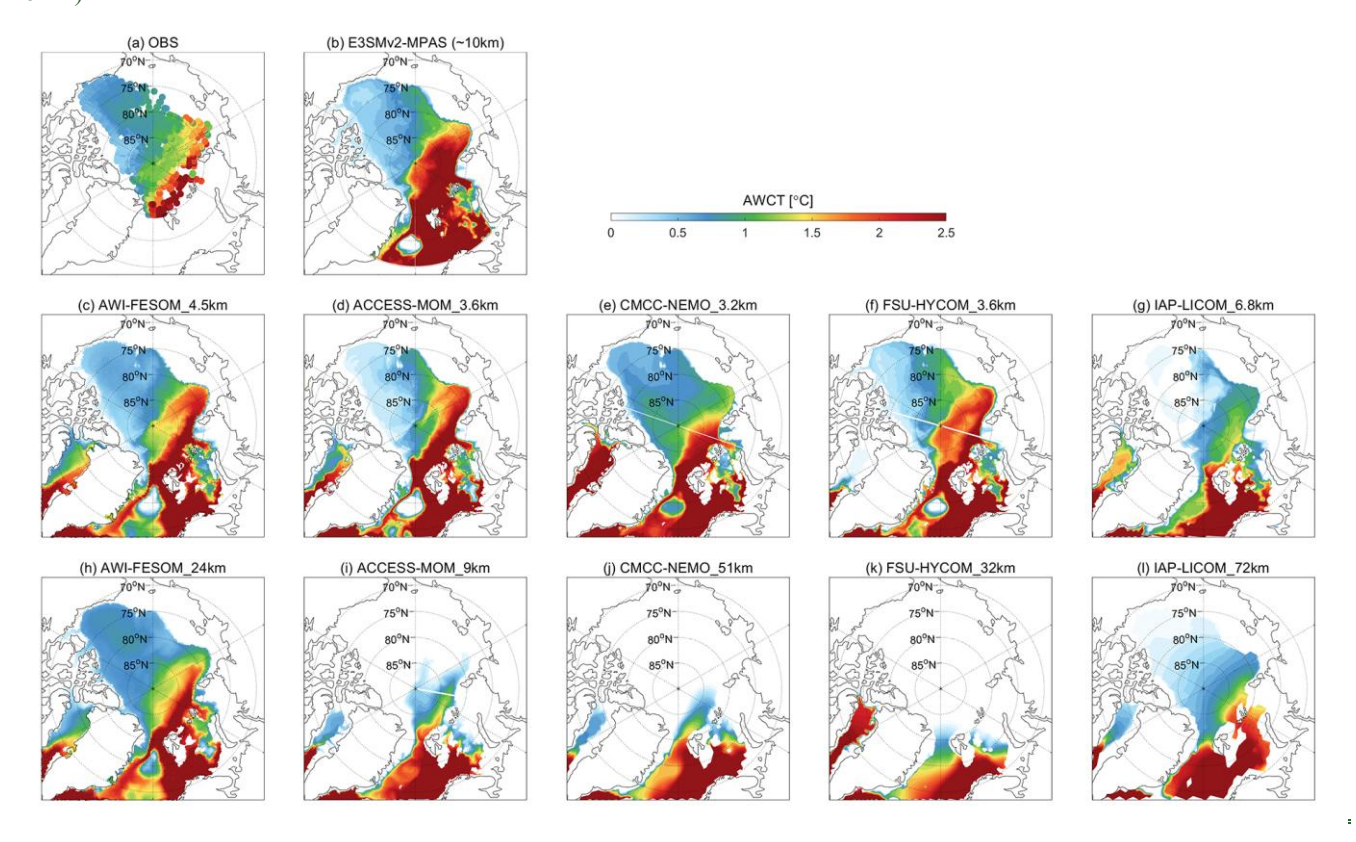


Figure 16. 1995-2018 climatological mean Atlantic Water Core Temperature (AWCT) spatial patterns from (a) observations (Richards et al., 2022), (b) E3SMv2-MPAS, and (c-l) OMIP2 models (Wang et al., 2024). Middle/bottom rows: High-resolution and corresponding low-resolution model pairs from OMIP2.

To address the systematic underestimation of Atlantification in model simulations (mentioned in Section 1), five key parameters are quantified: AWCT, AWCD, AW upper boundary (0°C isotherm; Meyer et al. (2017)), AW layer thickness (between 0°C isotherms), and AW heat content. By analyzing their spatiotemporal response characteristics, this study investigates the trans-decadal evolution of Atlantification.

The AW heat content is calculated as follows (Polyakov et al., 2017):

850

855

860

865

870

$$Q = \int_{z_{\star}}^{z_{2}} \rho_{w} c_{p} \left(\theta - \theta_{freezing}\right) dz, \tag{5}$$

where z_1/z_2 denote layer boundaries, ρ_w seawater density, c_p specific heat of seawater, and $\theta_{freezing}$ freezing temperature. Both basins exhibit coordinated changes during 1960s–1980s and 2000s–2020s: AWCT increases, AWCD decreases, AW upper boundary shallows, layer thickness expands, and heat content accumulates (Fig. 1817). Post-2000s acceleration of these trends shows tight coupling with enhanced Atlantic meridional heat transport under Arctic amplification. E3SMv2-MPAS captures the key thermodynamic signatures of Atlantification (the Eurasian Basin vs. the Amerasian Basins between 2000–2020), aligning closely with observationally derived mechanisms of AW Atlantic Water-intrusion and its climatic impacts (Polyakov et al., 2017): (1) A 1°C gradient in AWCT between the Eurasian and Amerasian Basins, consistent with zonal heat dissipation; (2) A 130-m shallower AWCD in the Eurasian Basin, reflecting intensified vertical mixing due to sea ice loss; (3) Synergistic changes in AW layer thickness and heat content (100 m thinner layer with +4000 MJ·m⁻² in the Eurasian Basin), confirming advective-diffusive redistribution.

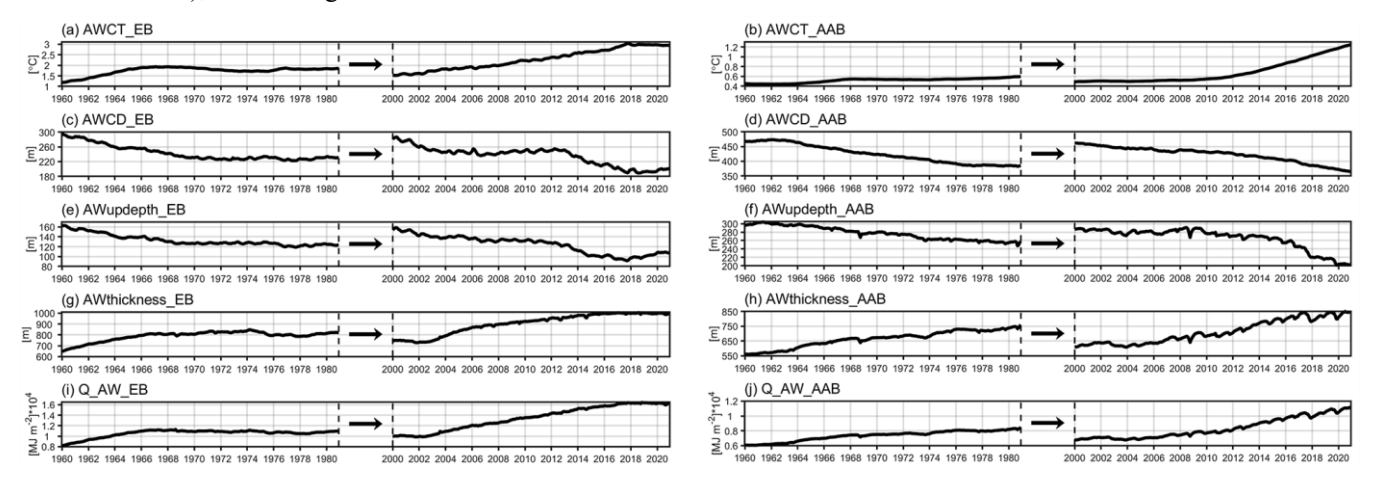


Figure 1817. (a-b) 1960-1980 vs. 2000-2020 climatological mean Atlantic Water Core Temperature (AWCT) in the (a) Eurasian basin (EB) and (b) Amerasian Basins (AAB). (c-j) The same as panels (a-b) but for Atlantic Water Core depth (AWCD; (c-d), Atlantic Water AW layer upper boundary depth (AWupdepth; e-f), thickness (AWthickness; g-h), and heat content (Q_AW; i-j).

This multi-scale validation confirms E3SMv2-MPAS's physical credibility in reproducing Atlantification mechanisms: cascading heat flux-stratification-heat content responses and inter-basin thermodynamic evolution. The model thus provides critical process fidelity for predicting Arctic oceanic thermal threshold transitions.

4.2 Coupling between the Atlantic Water and Surface layers Coupling

875

880

885

890

900

The AW layer constitutes the most critical oceanic heat reservoir in the Arctic Ocean (Carmack et al., 2015), containing sufficient thermal energy to melt all Arctic sea ice within several years (Tumer, 2010) and capable of dissolving 3–4 times the current ice volume (Carmack et al., 2015; Polyakov et al., 2020b)(Carmack et al., 2015a). A pronounced halocline characterized by rapidly increasing salinity with depth typically separates the cold, low-salinity surface waters from the warm, saline AW in the Eurasian and Amerasian Basins. This strong stratification effectively inhibits vertical water mass exchange (Peralta-Ferriz and Woodgate, 2015), isolating the AW layer from sea ice and mixed layer interactions (Aagaard et al., 1981; Richards et al., 2022). Under these physical constraints, vertical heat transport primarily occurs through molecular-scale processes involving internal wave breaking and double-diffusive mixing (Davis et al., 2016). However, since the 1970s, progressive weakening of the eastern Eurasian Basin halocline has been documented (Polyakov et al., 2010; Steele and Boyd, 1998), culminating in its complete failure as an effective thermal barrier for intermediate AW heat by the mid-2010s (Polyakov et al., 2020a). Stratification collapse has triggered a regime shift from double-diffusive dominance to shear-driven turbulent mixing, fundamentally altering vertical heat flux dynamics (Polyakov et al., 2020a).

The KPP scheme employed by E3SMv2-MPAS driven by Gradient Richardson Number (Ri) physics (Zhu et al., 2022). This study evaluates whether this parameterization scheme, combined with the model's unstructured mesh capability, adequately resolves Arctic vertical thermal coupling features, particularly in the Eurasian Basin. A diagnostic framework based on spatiotemporal correlation analysis is established to quantify the thermal linkage A thermal linkage framework is established between the upper (10 m) and intermediate (AW core layer, 400 m) ocean layers. to This analysis addresses two critical aspects: (1) spatiotemporal delay characteristics in vertical heat signal propagation relative to AW transport timescales, and (2) potential regime shifts in interlayer coupling mechanisms under climate warming. This diagnostic framework provides dynamic constraints for optimizing vertical mixing parameterizations while elucidating climate impacts of upper-ocean thermal variability.

During 1960–1980 baseline conditions (zero time lag), statistically significant positive correlations (p<0.05) between AW layer and surface temperatures are confined to the Norwegian Sea, indicating direct advective heat modulation (Fig. 1948a). Lagged correlation analysis reveals basin-scale inertial transport characteristics: localized positive correlations emerge in the Eurasian Basin at 24-month lag, expanding basin-wide by 36 months (Fig. 1948b—h). This spatiotemporal inertia is attributed to: (1) Basin-scale recirculation timescales required for AW mass circumpolar transport (e.g., 2-year lag between the Fram Strait and the eastern Eurasian Basin 250 m temperatures; Polyakov et al. (2020b)), and (2) efficiency limitations in subsurface mixing processes.

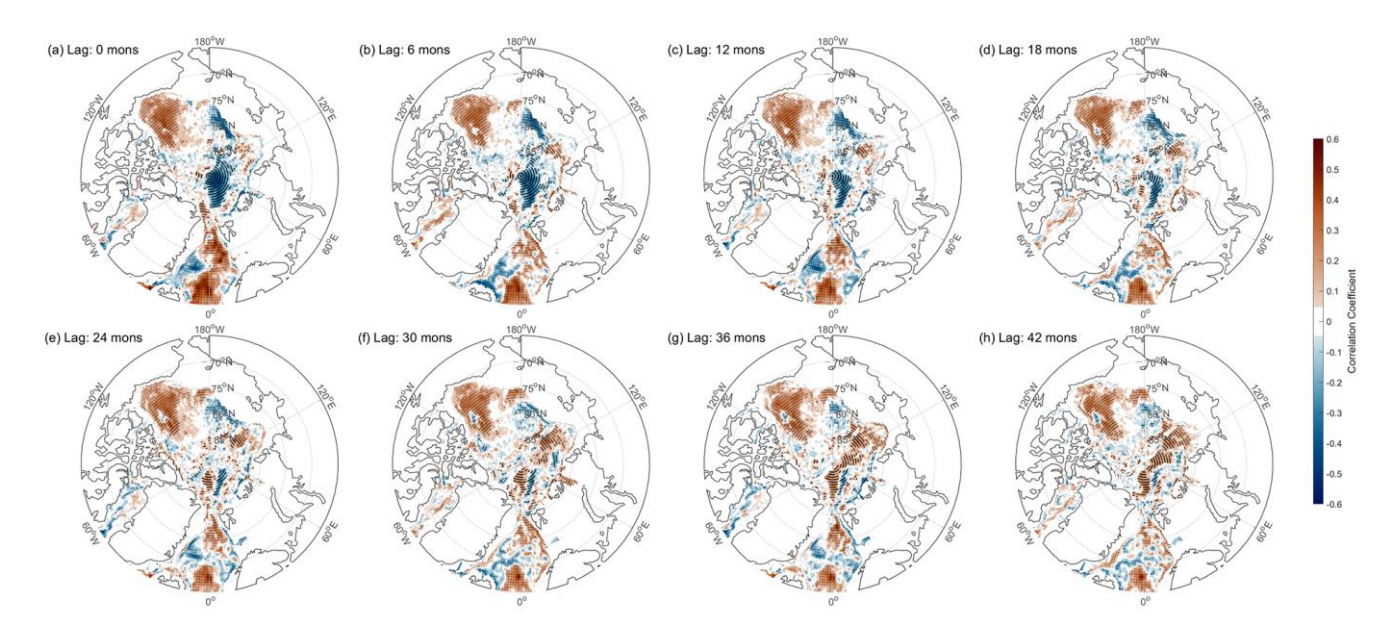


Figure 1918. (a) 1960–1980 climatological mean correlation between surface (5 m) and mid-depth (400 m) temperatures. (b-h) Lagged correlations at 6-month intervals (lag 6 mons to 42 mons). Black dots indicate significance (p<0.05).

The 1995–2020 period exhibits fundamental regime transition: immediate basin-wide positive correlations (p<0.05) emerge along AW pathways (from the Fram Strait to the Eurasian Basin) under zero-lag conditions, maintaining stable correlation strength through 42-month lags (Fig. 2019). This instantaneous response pattern reflects multiscale Arctic system changes: (1) Increased AWCT with decreased AWCD shortens vertical diffusion pathways, indicating intensified "Atlantification" (Polyakov et al., 2017); (2) Stratification weakening from sea ice loss enhances cross-layer turbulent mixing efficiency (Kwok, 2018; Onarheim et al., 2018; Polyakov et al., 2020a).

905

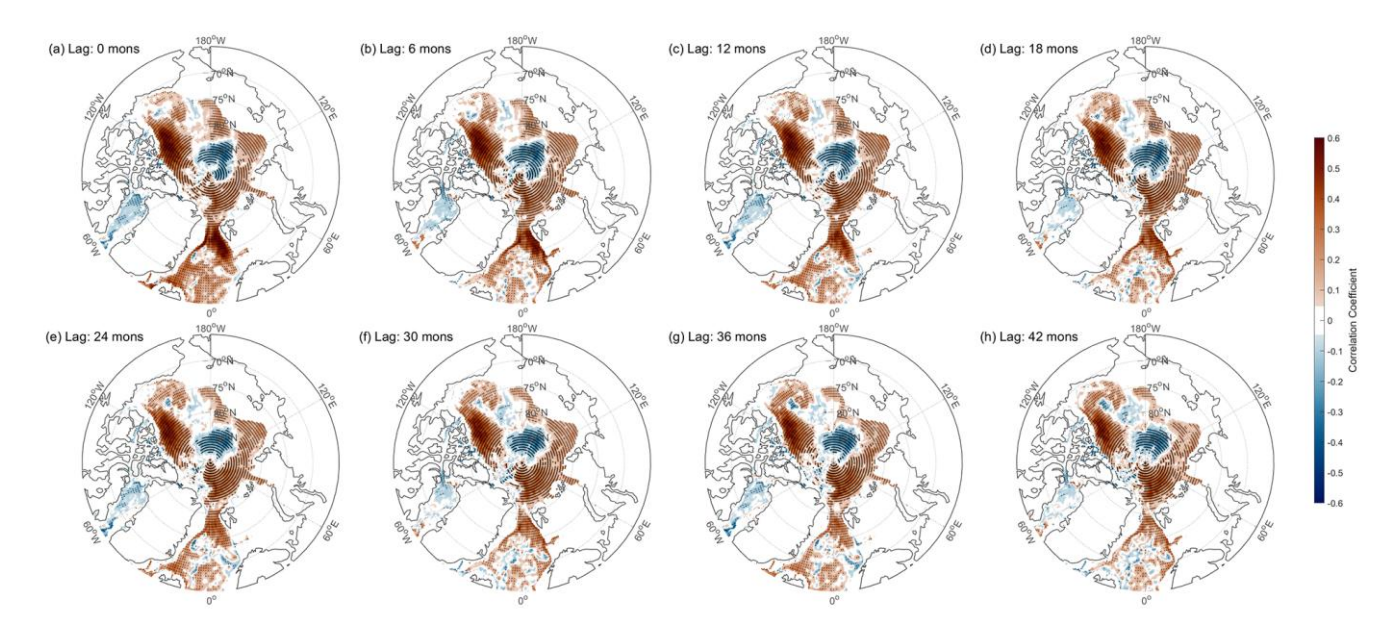


Figure 2019. The same as Fig. 1918, but for 1995-2020 period.

A fundamental regime shift in Arctic intermediate-to-surface thermal coupling mechanisms under climate warming is revealed through cross-temporal-scale lagged correlation diagnostics: transitioning from historical basin-scale inertial transport patterns to contemporary instantaneous response modes. This regime shift, driven by altered AW thermohaline properties and reduced stratification stability, enhances vertical heat leakage efficiency from intermediate layers. Model evaluation demonstrates that while the KPP scheme captures accelerated heat transport trends, systematic biases persist in nonlinear responses to shear mixing (Figs. 1948 and -2019). Future research directions emphasize developing scale-aware parameterizations incorporating high-resolution turbulence observations to improve model capabilities in predicting Arctic energy transport regime shifts.

5 Discussion

910

915

920

925

5.1 Comparison with OMIP2 models under diverse grid configurations and resolutions

Comprehensive analysis of higher resolution CMIP6 models reveals common thermohaline simulation biases (Fig. 8). To evaluate resolution sensitivity in Arctic Intermediate Water simulations, the assessment framework is extended to To evaluate the performance of different ocean-sea ice coupled models in simulating the three-dimensional themohaline structure, particularly that of the intermediate AW layer, we further discuss five resolution-matched model pairs from OMIP2 (Wang et al., 2024) (Wang et al., 2024; see Table 1). Thermohaline profile characteristics in the Eurasian and Amerasian Basins are systematically compared between high/low-resolution model pairs (solid/dashed lines), E3SMv2-

MPAS, and WOA23 data (Locarnini et al., 2024; Reagan et al., 2024) to elucidate ocean model grid configuration impacts (Fig. 921).

1930 Low-resolution models exhibit persistent CMIP6-systematic biases as follows: (1) Substantial underestimation of AWCT (e.g., <0°C in CMCC-NEMO 51km and FSU-HYCOM 32km), and (2) An inability to reproduce the characteristic vertical thermohaline structure, wherein temperatures decline with depth after AWCD. These challenges are particularly pronounced in the Eurasian Basin influenced by the Fram Strait branch (one of two primary AW inflow pathways) compared to the Amerasian Basin. In contrast, while their high-resolution counterparts (excluding IAP-LICOM-6.8km) demonstrate improved intermediate water core temperature AWCT and vertical structure simulations. High-resolution models successfully reproduce observed zonal gradients showing AWCT temperature maxima decreasing from the Eurasian Basin (1.3°C@250 m) to the Amerasian Basin (0.7°C@400 m), confirming resolution enhancement benefits for oceanic frontal processes.

In the Eurasian Basin where simulation biases are most pronounced, the majority of high-resolution models — with the exception of E3SMv2-MPAS (10 km) and FESOM variants (4.5/24 km) — continue to exhibit overestimated AW layer thickness (between 0°C isotherms). WOA23 observations indicate temperature decline to 0°C at 800 m depth, whereas most models (e.g., CMCC-NEMO 3.2km, FSU-HYCOM 3.6km and IAP-LICOM 6.8km) maintain ~0.5°C at the same depth 1000 m (Fig. 921a). This persistent discrepancy demonstrates that resolution enhancement alone remains insufficient to fully resolve key technical bottlenecks in Arctic Intermediate Water simulations. Notably, E3SMv2-MPAS and FESOM models exhibit strong breakthrough-performance (Table 3).

940

945

950

Despite comparable resolutions to other high resolution models (e.g., ACCESS MOM 9 km, FSU HYCOM 32 km), unstructured mesh configurations enable refined representation of key hydrographic gateways like the Fram Strait. Compared to tripolar grid models suffering numerical dissipation near complex coastlines, variable mesh designs achieve reduced the Eurasian Basin temperature errors under equivalent computational resources. Model grid type and computational efficiency exhibit nonlinear relationships. Unstructured meshes (FESOM/MPAS) permit dynamic optimization through localized refinement in critical regions (e.g., AW intrusion pathways). This targeted refinement strategy provides new technical approaches for Arctic ocean modeling, particularly under accelerating Atlantification processes.

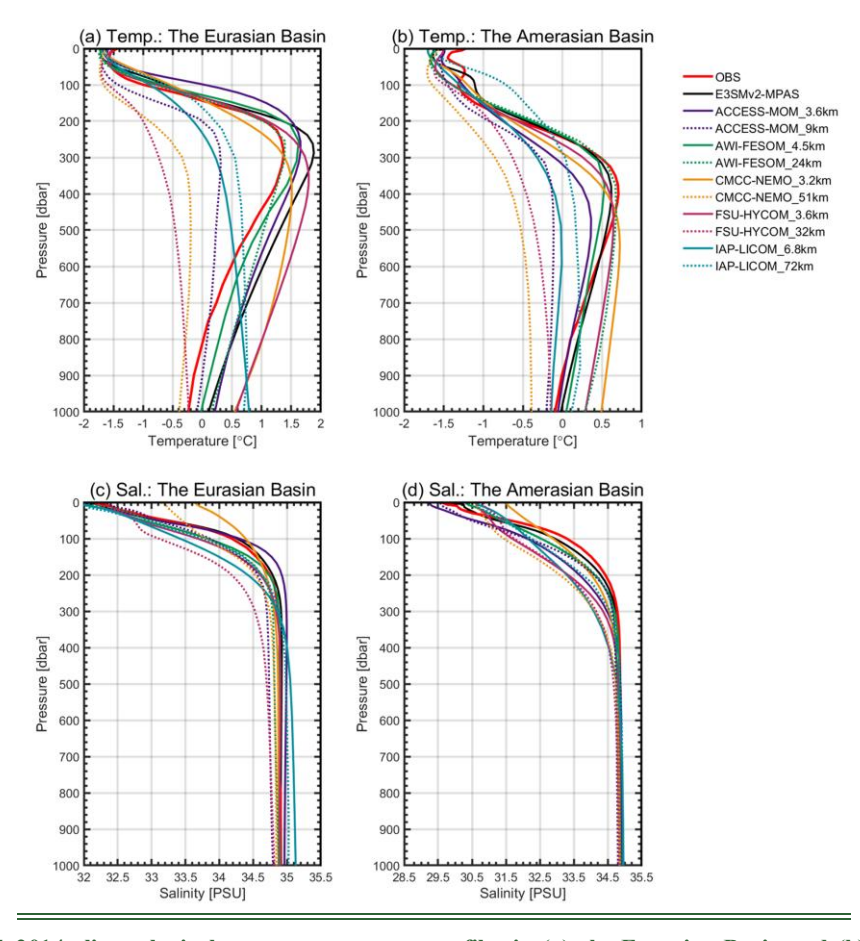


Figure 219. (a-b) 1995-2014 climatological mean temperature profiles in (a) the Eurasian Basin and (b) the Amerasian Basin:

Observations (WOA23; red), E3SMv2-MPAS (black), OMIP2 models (Wang et al., 2024; dashed: low-resolution, solid: high-resolution). (c-d) The same as panels (a-b) but for salinity profiles.

Table 3. Root mean square errors (RMSE) for temperature (Temp.; °C) and salinity (Sal.; PSU) in 0 1000 m vertical profiles from E3SMv2 MPAS and 5 OMIP2 model pairs (Wang et al., 2024), evaluated against WOA23 in the Eurasian Basin and the Amerasian Basin. Performance ranking: * indicates lowest RMSE per basin/variable, underlined values denote second lowest.

	<u>Eurasian Basin</u>		Amerasian Basin	
	Temp.	<u>Sal.</u>	Temp.	Sal.
E3SMv2-MPAS	0.223*	<u>0.130*</u>	<u>0.143*</u>	0.219*
ACCESS-MOM_3.6km	<u>0.437</u>	<u>0.202</u>	<u>0.217</u>	<u>0.663</u>
ACCESS-MOM 9km	<u>0.583</u>	<u>0.208</u>	<u>0.423</u>	<u>0.557</u>
AWI-FESOM 4.5km	<u>0.236</u>	<u>0.205</u>	<u>0.207</u>	<u>0.390</u>
AWI-FESOM_24km	<u>0.230</u>	<u>0.187</u>	<u>0.253</u>	<u>0.397</u>

CMCC-NEMO_3.2km	<u>0.453</u>	<u>0.762</u>	<u>0.276</u>	<u>1.055</u>
CMCC NEMO 51km	<u>0.869</u>	<u>0.600</u>	<u>0.558</u>	<u>0.875</u>
FSU-HYCOM 3.6km	<u>0.409</u>	<u>0.240</u>	<u>0.186</u>	<u>0.719</u>
FSU-HYCOM 32km	<u>1.012</u>	<u>0.442</u>	<u>0.485</u>	<u>0.797</u>
IAP-LICOM 6.8km	<u>0.716</u>	<u>0.457</u>	<u>0.346</u>	<u>0.882</u>
IAP-LICOM 72km	<u>0.435</u>	0.319	<u>0.456</u>	<u>0.716</u>

Following the evaluation of the three-dimensional thermohaline structure simulations in the OMIP2 models, we further examine their capability to reproduce the spatial distribution of AWCT. As indicated by Ccross-validation within under the OMIP2 framework, (Wang et al., 2024) reveals that among the five resolution-varied model groups, only FESOM 4.5km, MOM 3.6km, and HYCOM 3.6km demonstrate high AWCT spatial pattern simulation skills (Fig. 1622). FESOM 4.5km outperforms E3SMv2-MPAS (10 km) in representing the western Eurasian Basin shelf-basin gradients, but underperforms in the Amerasian Basin (Fig. 1622b-c). Low-resolution models exhibit a systematic underestimation of AWCT, with FESOM 24km being the exception, reaffirming unstructured meshes' polar ocean modeling advantages (Fig. 1622h-l).

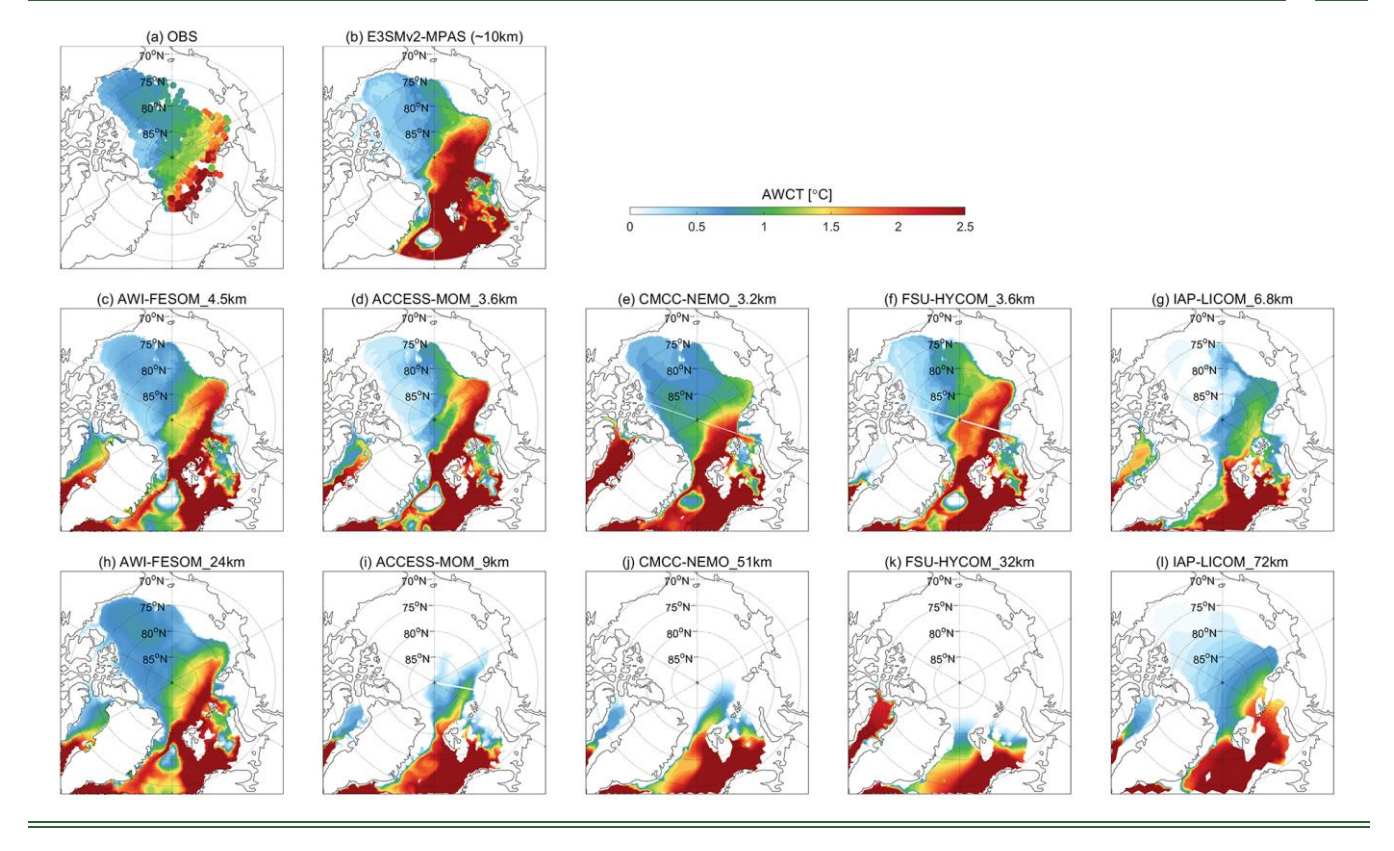


Figure 2216. 1995–2018 climatological mean Atlantic Water Core Temperature (AWCT) spatial patterns from (a) observations (Richards et al., 2022), (b) F3SMv2-MPAS, and (c-l) OMIP2 models (Wang et al., 2024). Middle/bottom rows: High-resolution and corresponding low-resolution model pairs from OMIP2.

Despite comparable resolutions to other high-resolution models (e.g., ACCESS-MOM 9 km, FSU-HYCOM 32 km), unstructured mesh configurations enable refined representation of key hydrographic gateways like the Fram Strait. Compared to tripolar grid models suffering numerical dissipation near complex coastlines, variable mesh designs achieve reduced the Eurasian Basin temperature errors under equivalent computational resources. Model grid type and computational efficiency exhibit nonlinear relationships. Unstructured meshes (FESOM/MPAS) permit dynamic optimization through localized refinement in critical regions (e.g., AW intrusion pathways). This targeted refinement strategy provides new technical approaches for Arctic ocean modeling, particularly under accelerating Atlantification processes.

5.2 Sources of systematic biases and trade-offs between resolution and parameterizations

980

985

990

995

1000

Analyses in Section 3 not only discussed the simulation biases of E3SMv2-MPAS but also traced their potential origins. For most biases, the primary causes can be attributed to inadequacies in physical parameterizations. First, the inadequate representation of eddy dynamics is a key source. For instance, the underestimation of freshening in the Amerasian Basin may result from the use of a fixed eddy diffusivity (κ=300 m² s¹ in the Arctic), which oversmooths salinity fronts. Similarly, the model's failure to capture the seasonal variability of the AW layer likely stems from the invariant κ in the GM scheme, which cannot respond to the seasonal cycle of sea ice retreat and associated changes in stratification. Second, limitations in vertical mixing parameterizations act as another key source. The coordinated biases in SST, SSS, and SIC in the Greenland and Barents Seas, for example, may arise from the inherent limitations of the KPP scheme's single Ri-based approach in defining turbulent states and mixing intensities within complex dynamic environments. Additionally, the misrepresentation of the warming layer in the Eurasian Basin could be linked to inappropriate background diffusion coefficients within the KPP framework.

Increasing model resolution presents an effective pathway to reduce reliance on empirical parameterizations by more directly resolving key physical processes, such as mesoscale eddies. Enhanced resolution can, to some extent, mitigate the inaccuracies of existing schemes. For instance, studies have shown that higher resolution improves the simulation of the AW layer's temperature, thickness, spatial distribution, and its decadal warming trends (Wang et al., 2024). However, the small Rossby radius of deformation (often ≤3 km) in the Arctic (Veneziani et al., 2022) implies that even with computationally feasible resolution increases, critical processes (e.g. mesoscale eddies, vertical mixing, and ice-ocean interactions) may remain under-resolved (Chassignet et al., 2020; Wang et al., 2018). Therefore, the development of more advanced physical parameterizations remains imperative. It is noteworthy that resolution increases have proven effective in improving the simulation of volume, heat, and freshwater transports through critical gateways such as the Fram Strait and Davis Strait (Wang et al., 2024). The Fram Strait, in particular, serves as a pivotal channel for Atlantic heat influx into the Arctic Ocean (Herbaut et al., 2022; Pnyushkov et al., 2021). In conclusion, we propose that a cost-effective strategy involves targetedly

increasing resolution in key gateway regions while concurrently refining parameterizations for mesoscale eddies and vertical mixing.

5.3 Limitations of the experimental design

1005

1010

1015

1030

Due to computational resource constraints, this study adopted a two-phase simulation strategy with non-consecutive time periods: first, the model was integrated from 1958 to 1981, and the final state of this period was used as the initial condition to directly start the simulation for the 1995–2020 period. Although this approach effectively reduced computational costs, and both previous studies and our model diagnostics indicate that key upper-ocean and sea ice variables had reached a quasi-equilibrium state by 1981, skipping the continuous integration of the 1982–1994 period may introduce certain limitations. For instance, the simulation of some medium- to long-term fluctuations or memory-dependent processes might be affected. Should computational resources allow in the future, we will perform a continuous simulation from 1958 to 2020 to more accurately reproduce the evolution of the climate system.

Furthermore, since only a single JRA55 forcing cycle was applied, the deep ocean and some physical quantities may not have fully departed from the influence of the initial PHC hydrographic fields or reached complete equilibrium. This could potentially affect the stability and initial-condition independence of the simulation results. In subsequent work, given sufficient resources, we plan to carry out at least three full JRA55 forcing cycles to promote more complete adjustment of the ocean state, reduce dependence on initial conditions, and thereby enable a more comprehensive and robust evaluation of the climate performance of the E3SMv2-MPAS.

5.4 Limitations from the atmospheric forcing: the JRA55 warm bias

The JRA55 reanalysis forcing data employed in E3SMv2-MPAS exhibits a known warm bias over the central Arctic deep basin (Batrak and Müller, 2019). This bias may systematically suppress sea ice growth and induce upper-ocean warming in the simulation by enhancing downward longwave radiation and reducing oceanic sensible heat loss. Therefore, the overestimated SST (Fig. 8c) and underestimated summer SIC (Fig. 4e–g) simulated in the central Arctic basin may be partially attributable to the inherent bias in the forcing data, rather than solely to inaccuracies in the model's physical processes.

The enhanced ice melt driven by this warm bias releases additional freshwater, leading to a stronger and shallower freshwater layer (a more pronounced halocline) in the surface ocean, which significantly strengthens the stratification stability of the upper ocean. This inhibits vertical mixing between layers and impedes the upward heat transfer from the warmer, saltier AW below. This bias may partly explain the overestimation of the intermediate AW layer temperature alongside the underestimation of the mixed-layer temperature (Fig. 12e). Future work will consider employing alternative reanalysis products or applying bias-correction methods to better constrain the impact of forcing uncertainties on simulation results.

65 Conclusions

This study systematically evaluates the Arctic ocean-sea ice simulation capabilities of E3SMv2-MPAS through multi-source observations (in situ profiles, satellite remote sensing, optimum interpolation dataesets); and reanalysis products (NSIDC, HadISST1, ERA5, PIOMAS, ORAS5) and model outputs (CMIP6, OMIP2), with focus on core parameters including sea ice (concentration/extent/thickness/volume; SIC/SIE/SIT/SIV), surface thermohaline properties (sea surface temperature/salinity; SST/SSS), three-dimensional thermohaline structures, freshwater content (FWC), gateway transports, Atlantic Water (AW) heat characteristics, and vertical thermal linkages. Spatial distribution patterns, seasonal-to-decadal variability, and three-dimensional evolutionary processes are comprehensively analyzed.

E3SMv2-MPAS demonstrates significant advantages in Arctic climatology simulations: (1) Accurate representation of spatial heterogeneity and temporal evolution trends in SIC, SIT, and SST (Figs. 3a-5g, 48a-c, 6a-e); (2) Realistic simulation of interannual and decadal variability in SIC, SIE, SIT, SIV and SST, along with a highly consistent reproduction of the Superior simulation accuracy for 1995–2020 SIC decline trends compared to NSIDC observation, outperforming Hadley and ERA5 reanalysis products (NSIDC-benchmarked; Fig. 37ah); (3) Enhanced SIT reliability in the Greenland Sea and the Canadian Archipelago versus PIOMAS (ICESat validated; Fig. 5); (34) Consistent SSS spatial patterns and seasonal evolution with leading reanalysis products including HYCOM and GLORYS12 (Fig. 97; Hall et al. (2021)); (4) Faithful reproduction of both the spatial distribution and long-term trend of Arctic FWC (Fig. 15); (5) Accurate simulation of volume, heat, and freshwater transports through key Arctic gateways, capturing their observed magnitudes and essential variability trends (Fig. 16).

E3SMv2-MPAS demonstrates exceptional capability in simulating the three-dimensional thermohaline structure and variability of the AW layer, accurately capturing its key thermodynamic and dynamic processes in the Arctic OccanE3SMv2 MPAS successfully addresses longstanding Arctic simulation biases through synergistic integration of high-resolution Arctic domains, flexible global unstructured meshes, and suitable mesoscale eddy parameterization: (1) Precise reproduction of AW layer thickness/depth and core temperatures (Figs. 10 and 178-10, 15-16), achieving minimal RMSE in three-dimensional thermohaline simulations across Arctic basins compared to CMIP6 and OMIP2 models (Tables 1-2); (2) Effective capture of AW warming trends including decadal-scale intermediate layer heating and vertical shoaling of warm cores (Figs. 11_and_5-13); (3) Realistic simulation of accelerated Atlantification processes, evidenced by post-2000 intensification in AW core temperature and heat content while reduced AW core depth, upper boundary and layer thickness, and instantaneous surface-intermediate heat transfer in the Eurasian Basin (Figs. 1817-2019). Additional breakthroughs include successful representation of solar-driven seasonal upper-ocean thermal cycles (Fig. 12) and inter-basin water mass gradient evolution from the Eurasian Basin to the Amerasian Basin (e.g., AW thermohaline attenuation, vertical stratification shifts, and surface freshwater transport effects; Fig. 14). These advancements establish critical numerical platforms for investigating Arctic stratification destabilization and cross-scale energy transfer mechanisms, particularly for quantifying mesoscale modulation of ocean-sea ice-atmosphere feedbacks.

Notwithstanding these achievements, key limitations persist: (1) Systematic overestimation of SIT in the Canadian Basin (0.5-1 m bias: Fig. 5), potentially linked to misrepresentation of Beaufort Gyre intensity enhancing ice convergence. requiring verification through eddy kinetic energy budget analysis; (2) Coordinated underestimation of SST/SSS and overestimation of SIC in the Greenland and Barent Seas (Figs. 3a-4g, 84a-c, 96a-c), attributable to underestimated efficiency of vertical mixing in intermediate-to-surface heat transfer, recommending implementation of shear turbulence elosure schemes or dynamic mixed layer penetration mechanisms; (3) Residual overestimation of AW core temperature (0– 1°C) and errors in seasonal Atlantification phase (Figs. 8–10 and, 123), reflecting constraints of mesoscale parameterization on water mass transformation, necessitating development of depth-dependent eddy energy dissipation parameterizations; (4) Asymmetries in regional decadal thermohaline evolution (e.g., underestimated upper-layer warming and overestimated deep warming in the Eurasian Basin, unresolved mid-layer warming and upper-layer freshening trends in the Amerasian Basin; Fig. 13), potentially arising from inadequate resolution of key gateways (e.g., Fram Strait) and oversimplified parameterizations of shelf-basin interactions, demanding optimization through nested grids or regional mesh refinement. This study confirms that E3SMv2-MPAS significantly enhances simulation capabilities for Arctic oceanic thermal structures and cross-layer coupling processes through integration of high-resolution unstructured meshes with optimized physical parameterization schemes, establishing crucial technical references for polar climate model development in the CMIP7 era. However, persistent biases highlight remaining challenges in mesoscale process representation and boundary flux constraints. Future priorities include: (1) Development of process oriented parameterizations enabling eddy mixingstratification feedback coupling; (2) Implementation of Arctic-focused data assimilation systems to reduce boundary forcing uncertainties: (3) Execution of perturbed parameter ensemble experiments to quantify sensitivity thresholds. Such improvements will enhance predictive capabilities for Arctic amplification and tipping point dynamics, ultimately supporting evidence-based climate governance.

1070

1075

1080

1085

1090 Code and data availability. The E3SM model code is publicly available via the https://github.com/E3SM-Project/E3SM/releases. Instructions on how to configure and execute E3SM are available at https://e3sm.org/model/running-e3sm/e3sm-quick-start/. All simulations detailed in Section 2.1 can be regenerated by executing the code hosted in this repository: https://doi.org/10.5281/zenodo.15493256 (Lv, 2025). Preprocessing of E3SMv2-MPAS outputs utilized nco-5.1.1, accessible through the https://nco.sourceforge.net/. The JRA55-v1.5 atmospheric forcing data driving the simulations were obtained from the https://aims2.llnl.gov/search/input4mips/. ETOPO 2022 bathymetry was derived from the https://www.ncei.noaa.gov/products/etopo-global-relief-model. Model evaluations employed the following observational and reanalysis products: Sea ice concentration: NSIDC (https://noaadata.apps.nsidc.org/NOAA/G02202_V4/north/aggregate/), Met Office Hadley Centre observational datasets (https://www.metoffice.gov.uk/hadobs/), and ERA5 monthly single-level data (https://cds.climate.copernicus.eu/datasets/reanalysis-era5-single-levels-monthly-means?tab=overview); Sea ice extent:

1100 NSIDC (https://doi.org/10.7265/N5K072F8); Sea ice thickness and sea ice volume: **PIOMAS** (http://psc.apl.uw.edu/research/projects/arctic-sea-ice-volume-anomaly/data/model grid), PIOMAS-20C reconstruction gridded (https://psc.apl.uw.edu/research/projects/piomas-20c/) and CS2SMOSICESat/ICESat-2 L4 products (https://data.meereisportal.de/data/cs2smos awi/v206/nhttps://nsidc.org/data/issitgr4/versions/1 https://nsidc.org/data/is2sitmogr4/versions/3); Sea surface properties: OISST (https://www.ncei.noaa.gov/products/optimum-1105 interpolation-sst) and OISSS (https://www.esr.org/data-products/oisss/overview/); Oceanographic profiles: WOA2023 (https://www.ncei.noaa.gov/products/world-ocean-atlas). EN.4.2.2 objective analyzes analyses surface (https://www.metoffice.gov.uk/hadobs/en4/);-Sea height: ORAS5 (https://cds.climate.copernicus.eu/datasets/reanalysis-oras5?tab=overview); Ocean heat content: **IAP** (http://www.ocean.iap.ac.cn/ftp/cheng/IAPv4.2 Ocean heat content 0 6000m/); Surface albedo: CLARA-A3 (https://doi.org/10.5676/EUM SAF CM/CLARA AVHRR/V003). In situ observational profiles from four key Arctic 1110 regions (the western/eastern Eurasian Basin, the Chukchi Sea, and the Beaufort Sea), vertical profiles from 13 CMIP6 models, thermohaline profiles and Atlantic Water core temperature outputs from five OMIP2 ensemble groups, along with E3SM Arctic OSI simulations and Atlantic Water core temperature and depth observational benchmarks, are described in the main text. Detailed metadata specifications and data access instructions for these datasets are provided in the 1115 corresponding references cited therein.

Author contributions. XL led the manuscript writing and paper analysis. XL, YC, and HD performed the installation, configuration, and execution of the E3SMv2-MPAS model. HW, KR, and YW were primarily responsible for the conceptualization of the study and manuscript revisions. All co-authors reviewed and commented on the final version of the manuscript.

Competing interests. No competing interests are present.

1125

Acknowledgments. The public availability of different observational data sets and reanalysis data used in this work is a great help for model development, so the efforts of respective working groups are appreciated. This work was supported by the National Key R&D Program of China (Grant No. 2021YFC3101503), the Science and Technology Innovation Program of Hunan Province (Grant No. 2022RC3070), the National Natural Science Foundation of China (Grant No. 42305176), the

Hunan Provincial Natural Science Foundation of China (Grant No. 2023JJ10053), the National Natural Science Foundation of China (Grant No. 42276205) and the Hunan Provincial Science and Technology Innovation Leading Talent Fund.

References

- Aagaard, K. and Carmack, E. C.: The role of sea ice and other fresh water in the Arctic circulation, J. Geophys. Res., 94, 14485–14498, https://doi.org/10.1029/JC094iC10p14485, 1989.
- Aagaard, K., Coachman, L. K., and Carmack, E.: On the halocline of the Arctic Ocean, Deep Sea Research Part A. Oceanographic Research Papers, 28, 529–545, https://doi.org/10.1016/0198-0149(81)90115-1, 1981.
 - Aksenov, Y., Karcher, M., Proshutinsky, A., Gerdes, R., De Cuevas, B., Golubeva, E., Kauker, F., Nguyen, A. T., Platov, G. A., Wadley, M., Watanabe, E., Coward, A. C., and Nurser, A. J. G.: Arctic pathways of P acific W ater: Arctic O cean M odel Intercomparison experiments, JGR Oceans, 121, 27–59, https://doi.org/10.1002/2015JC011299, 2016.
- Årthun, M., Eldevik, T., Smedsrud, L. H., Skagseth, Ø., and Ingvaldsen, R. B.: Quantifying the Influence of Atlantic Heat on Barents Sea Ice Variability and Retreat*, Journal of Climate, 25, 4736–4743, https://doi.org/10.1175/JCLI-D-11-00466.1, 2012.
 - Årthun, M., Eldevik, T., and Smedsrud, L. H.: The Role of Atlantic Heat Transport in Future Arctic Winter Sea Ice Loss, Journal of Climate, 32, 3327–3341, https://doi.org/10.1175/JCLI-D-18-0750.1, 2019.
- Arzel, O., Fichefet, T., Goosse, H., and Dufresne, J.-L.: Causes and impacts of changes in the Arctic freshwater budget during the twentieth and twenty-first centuries in an AOGCM, Clim Dyn, 30, 37–58, https://doi.org/10.1007/s00382-007-0258-5, 2007.
- Barton, B. I., Lenn, Y.-D., and Lique, C.: Observed Atlantification of the Barents Sea Causes the Polar Front to Limit the Expansion of Winter Sea Ice, Journal of Physical Oceanography, 48, 1849–1866, https://doi.org/10.1175/JPO-D-18-0003.1, 2018.
 - Batrak, Y. and Müller, M.: On the warm bias in atmospheric reanalyses induced by the missing snow over Arctic sea-ice, Nat Commun, 10, 4170, https://doi.org/10.1038/s41467-019-11975-3, 2019.
 - Calvin, K., Dasgupta, D., Krinner, G., Mukherji, A., Thome, P. W., Trisos, C., Romero, J., Aldunce, P., Barrett, K., Blanco, G., Cheung, W. W. L., Connors, S., Denton, F., Diongue-Niang, A., Dodman, D., Garschagen, M., Geden, O., Hayward, B., Jones, C., Jotzo, F., Krug, T., Lasco, R., Lee, Y.-Y., Masson-Delmotte, V., Meinshausen, M., Mintenbeck, K., Mokssit, A.,
- Jones, C., Jotzo, F., Krug, T., Lasco, R., Lee, Y.-Y., Masson-Delmotte, V., Meinshausen, M., Mintenbeck, K., Mokssit, A., Otto, F. E. L., Pathak, M., Pirani, A., Poloczanska, E., Pörtner, H.-O., Revi, A., Roberts, D. C., Roy, J., Ruane, A. C., Skea, J., Shukla, P. R., Slade, R., Slangen, A., Sokona, Y., Sörensson, A. A., Tignor, M., Van Vuuren, D., Wei, Y.-M., Winkler, H., Zhai, P., Zommers, Z., Hourcade, J.-C., Johnson, F. X., Pachauri, S., Simpson, N. P., Singh, C., Thomas, A., Totin, E., Arias, P., Bustamante, M., Elgizouli, I., Flato, G., Howden, M., Méndez-Vallejo, C., Pereira, J. J., Pichs-Madruga, R., Rose,
- S. K., Saheb, Y., Sánchez Rodríguez, R., Ürge-Vorsatz, D., Xiao, C., Yassaa, N., Alegría, A., Armour, K., Bednar-Friedl, B., Blok, K., Cissé, G., Dentener, F., Eriksen, S., Fischer, E., Garner, G., Guivarch, C., Haasnoot, M., Hansen, G., Hauser, M., Hawkins, E., Hermans, T., Kopp, R., Leprince-Ringuet, N., Lewis, J., Ley, D., Ludden, C., Niamir, L., Nicholls, Z., Some, S., Szopa, S., Trewin, B., Van Der Wijst, K.-I., Winter, G., Witting, M., Birt, A., Ha, M., et al.: IPCC, 2023: Climate Change 2023: Synthesis Report. Contribution of Working Groups I, II and III to the Sixth Assessment Report of the
- Intergovernmental Panel on Climate Change [Core Writing Team, H. Lee and J. Romero (eds.)]. IPCC, Geneva, Switzerland., Intergovernmental Panel on Climate Change (IPCC), https://doi.org/10.59327/IPCC/AR6-9789291691647, 2023.
 - Carmack, E., Polyakov, I., Padman, L., Fer, I., Hunke, E., Hutchings, J., Jackson, J., Kelley, D., Kwok, R., Layton, C., Melling, H., Perovich, D., Persson, O., Ruddick, B., Timmermans, M.-L., Toole, J., Ross, T., Vavrus, S., and Winsor, P.:
- Toward Quantifying the Increasing Role of Oceanic Heat in Sea Ice Loss in the New Arctic, Bulletin of the American Meteorological Society, 96, 2079–2105, https://doi.org/10.1175/BAMS-D-13-00177.1, 2015.

- Chassignet, E. P., Yeager, S. G., Fox-Kemper, B., Bozec, A., Castruccio, F., Danabasoglu, G., Horvat, C., Kim, W. M., Koldunov, N., Li, Y., Lin, P., Liu, H., Sein, D. V., Sidorenko, D., Wang, Q., and Xu, X.: Impact of horizontal resolution on global ocean—sea ice model simulations based on the experimental protocols of the Ocean Model Intercomparison Project phase 2 (OMIP-2), Geosci. Model Dev., 13, 4595–4637, https://doi.org/10.5194/gmd-13-4595-2020, 2020.
 - Chen, C., Gao, G., Zhang, Y., Beardsley, R. C., Lai, Z., Qi, J., and Lin, H.: Circulation in the Arctic Ocean: Results from a high-resolution coupled ice-sea nested Global-FVCOM and Arctic-FVCOM system, Progress in Oceanography, 141, 60–80, https://doi.org/10.1016/j.pocean.2015.12.002, 2016.
- Cheng, L., Trenberth, K. E., Fasullo, J., Boyer, T., Abraham, J., and Zhu, J.: Improved estimates of ocean heat content from 1960 to 2015, Sci. Adv., 3, e1601545, https://doi.org/10.1126/sciadv.1601545, 2017.
 - Cheng, L., Trenberth, K. E., Gruber, N., Abraham, J. P., Fasullo, J. T., Li, G., Mann, M. E., Zhao, X., and Zhu, J.: Improved Estimates of Changes in Upper Ocean Salinity and the Hydrological Cycle, Journal of Climate, 33, 10357–10381, https://doi.org/10.1175/JCLI-D-20-0366.1, 2020.
- Cheng, L., Pan, Y., Tan, Z., Zheng, H., Zhu, Y., Wei, W., Du, J., Yuan, H., Li, G., Ye, H., Gouretski, V., Li, Y., Trenberth, K. E., Abraham, J., Jin, Y., Reseghetti, F., Lin, X., Zhang, B., Chen, G., Mann, M. E., and Zhu, J.: IAPv4 ocean temperature and ocean heat content gridded dataset, Earth Syst. Sci. Data, 16, 3517–3546, https://doi.org/10.5194/essd-16-3517-2024, 2024.
- Curry, B., Lee, C. M., Petrie, B., Moritz, R. E., and Kwok, R.: Multiyear Volume, Liquid Freshwater, and Sea Ice Transports through Davis Strait, 2004–10*, Journal of Physical Oceanography, 44, 1244–1266, https://doi.org/10.1175/JPO-D-13-0177.1, 2014.
 - Danilov, S., Sidorenko, D., Wang, Q., and Jung, T.: The Finite-volumE Sea ice-Ocean Model (FESOM2), Geosci. Model Dev., 10, 765–789, https://doi.org/10.5194/gmd-10-765-2017, 2017.
 - D'Asaro, E. A.: The Energy Flux from the Wind to Near-Inertial Motions in the Surface Mixed Layer, 1985.
- Davis, P. E. D., Lique, C., Johnson, H. L., and Guthrie, J. D.: Competing Effects of Elevated Vertical Mixing and Increased Freshwater Input on the Stratification and Sea Ice Cover in a Changing Arctic Ocean, Journal of Physical Oceanography, 46, 1531–1553, https://doi.org/10.1175/JPO-D-15-0174.1, 2016.
 - Docquier, D. and Koenigk, T.: A review of interactions between ocean heat transport and Arctic sea ice, Environ. Res. Lett., 16, 123002, https://doi.org/10.1088/1748-9326/ac30be, 2021.
- Dörr, J., Årthun, M., Eldevik, T., and Madonna, E.: Mechanisms of Regional Winter Sea-Ice Variability in a Warming Arctic, Journal of Climate, 34, 8635–8653, https://doi.org/10.1175/JCLI-D-21-0149.1, 2021.
 - Fetterer, F.; K. K.; M. W.; S. M.; W. A.: Sea Ice Index, Version 3, https://doi.org/10.7265/N5K072F8, 2017.
 - Fu, C., Pennelly, C., Garcia-Quintana, Y., and Myers, P. G.: Pulses of Cold Atlantic Water in the Arctic Ocean From an Ocean Model Simulation, JGR Oceans, 128, e2023JC019663, https://doi.org/10.1029/2023JC019663, 2023.
- Gent, P. R. and Mcwilliams, J. C.: Isopycnal Mixing in Ocean Circulation Models, Journal of Physical Oceanography, 20, 150–155, https://doi.org/10.1175/1520-0485(1990)020%3C0150:IMIOCM%3E2.0.CO;2, 1990.
 - Golaz, J., Caldwell, P. M., Van Roekel, L. P., Petersen, M. R., Tang, Q., Wolfe, J. D., Abeshu, G., Anantharaj, V., Asay-Davis, X. S., Bader, D. C., Baldwin, S. A., Bisht, G., Bogenschutz, P. A., Branstetter, M., Brunke, M. A., Brus, S. R.,

- Burrows, S. M., Cameron-Smith, P. J., Donahue, A. S., Deakin, M., Easter, R. C., Evans, K. J., Feng, Y., Flanner, M., Foucar, J. G., Fyke, J. G., Griffin, B. M., Hannay, C., Harrop, B. E., Hoffman, M. J., Hunke, E. C., Jacob, R. L., Jacobsen,
- D. W., Jeffery, N., Jones, P. W., Keen, N. D., Klein, S. A., Larson, V. E., Leung, L. R., Li, H., Lin, W., Lipscomb, W. H., Ma, P., Mahajan, S., Maltrud, M. E., Mametjanov, A., McClean, J. L., McCoy, R. B., Neale, R. B., Price, S. F., Qian, Y., Rasch, P. J., Reeves Eyre, J. E. J., Riley, W. J., Ringler, T. D., Roberts, A. F., Roesler, E. L., Salinger, A. G., Shaheen, Z., Shi, X., Singh, B., Tang, J., Taylor, M. A., Thornton, P. E., Turner, A. K., Veneziani, M., Wan, H., Wang, H., Wang, S., Williams, D. N., Wolfram, P. J., Worley, P. H., Xie, S., Yang, Y., Yoon, J., Zelinka, M. D., Zender, C. S., Zeng, X., Zhang,
- 1220 C., Zhang, K., Zhang, Y., Zhou, T., and Zhu, Q.: The DOE E3SM Coupled Model Version 1: Overview and Evaluation at Standard Resolution, J Adv Model Earth Syst, 11, 2089–2129, https://doi.org/10.1029/2018MS001603, 2019.
 - Golaz, J., Van Roekel, L. P., Zheng, X., Roberts, A. F., Wolfe, J. D., Lin, W., Bradley, A. M., Tang, Q., Maltrud, M. E., Forsyth, R. M., Zhang, C., Zhou, T., Zhang, K., Zender, C. S., Wu, M., Wang, H., Turner, A. K., Singh, B., Richter, J. H., Qin, Y., Petersen, M. R., Mametjanov, A., Ma, P., Larson, V. E., Krishna, J., Keen, N. D., Jeffery, N., Hunke, E. C., Hannah,
- W. M., Guba, O., Griffin, B. M., Feng, Y., Engwirda, D., Di Vittorio, A. V., Dang, C., Conlon, L. M., Chen, C., Brunke, M. A., Bisht, G., Benedict, J. J., Asay-Davis, X. S., Zhang, Y., Zhang, M., Zeng, X., Xie, S., Wolfram, P. J., Vo, T., Veneziani, M., Tesfa, T. K., Sreepathi, S., Salinger, A. G., Reeves Eyre, J. E. J., Prather, M. J., Mahajan, S., Li, Q., Jones, P. W., Jacob, R. L., Huebler, G. W., Huang, X., Hillman, B. R., Harrop, B. E., Foucar, J. G., Fang, Y., Comeau, D. S., Caldwell, P. M., Bartoletti, T., Balaguru, K., Taylor, M. A., McCoy, R. B., Leung, L. R., and Bader, D. C.: The DOE E3SM Model Version
- 2: Overview of the Physical Model and Initial Model Evaluation, J Adv Model Earth Syst, 14, e2022MS003156, https://doi.org/10.1029/2022MS003156, 2022.
 - Good, S. A., Martin, M. J., and Rayner, N. A.: EN4: Quality controlled ocean temperature and salinity profiles and monthly objective analyses with uncertainty estimates, JGR Oceans, 118, 6704–6716, https://doi.org/10.1002/2013JC009067, 2013.
- Haine, T. W. N., Curry, B., Gerdes, R., Hansen, E., Karcher, M., Lee, C., Rudels, B., Spreen, G., De Steur, L., Stewart, K. D., and Woodgate, R.: Arctic freshwater export: Status, mechanisms, and prospects, Global and Planetary Change, 125, 13–35, https://doi.org/10.1016/j.gloplacha.2014.11.013, 2015.
 - Haine, T. W. N., Siddiqui, A. H., and Jiang, W.: Arctic freshwater impact on the Atlantic Meridional Overturning Circulation: status and prospects, Phil. Trans. R. Soc. A., 381, 20220185, https://doi.org/10.1098/rsta.2022.0185, 2023.
- Hall, S. B., Subrahmanyam, B., and Morison, J. H.: Intercomparison of Salinity Products in the Beaufort Gyre and Arctic Ocean, Remote Sensing, 14, 71, https://doi.org/10.3390/rs14010071, 2021.
 - Heidinger, A. K., Straka, W. C., Molling, C. C., Sullivan, J. T., and Wu, X.: Deriving an inter-sensor consistent calibration for the AVHRR solar reflectance data record, International Journal of Remote Sensing, 31, 6493–6517, https://doi.org/10.1080/01431161.2010.496472, 2010.
- Herbaut, C., Houssais, M., Blaizot, A., and Molines, J.: A Role for the Ocean in the Winter Sea Ice Distribution North of Svalbard, JGR Oceans, 127, e2021JC017852, https://doi.org/10.1029/2021JC017852, 2022.
 - Hersbach, H., Bell, B., Berrisford, P., Hirahara, S., Horányi, A., Muñoz-Sabater, J., Nicolas, J., Peubey, C., Radu, R., Schepers, D., Simmons, A., Soci, C., Abdalla, S., Abellan, X., Balsamo, G., Bechtold, P., Biavati, G., Bidlot, J., Bonavita, M., Chiara, G., Dahlgren, P., Dee, D., Diamantakis, M., Dragani, R., Flemming, J., Forbes, R., Fuentes, M., Geer, A., Haimberger, L., Healy, S., Hogan, R. J., Hólm, E., Janisková, M., Keeley, S., Laloyaux, P., Lopez, P., Lupu, C., Radnoti, G.,
- Rosnay, P., Rozum, I., Vamborg, F., Villaume, S., and Thépaut, J.: The ERA5 global reanalysis, Q.J.R. Meteorol. Soc., 146, 1999–2049, https://doi.org/10.1002/qj.3803, 2020.
 - Heuzé, C., Zanowski, H., Karam, S., and Muilwijk, M.: The Deep Arctic Ocean and Fram Strait in CMIP6 Models, Journal of Climate, 36, 2551–2584, https://doi.org/10.1175/JCLI-D-22-0194.1, 2023.

- Hinrichs, C., Wang, Q., Koldunov, N., Mu, L., Semmler, T., Sidorenko, D., and Jung, T.: Atmospheric Wind Biases: A Challenge for Simulating the Arctic Ocean in Coupled Models?, JGR Oceans, 126, e2021JC017565, https://doi.org/10.1029/2021JC017565, 2021.
 - Hoch, K. E., Petersen, M. R., Brus, S. R., Engwirda, D., Roberts, A. F., Rosa, K. L., and Wolfram, P. J.: MPAS-Ocean Simulation Quality for Variable-Resolution North American Coastal Meshes, J Adv Model Earth Syst, 12, e2019MS001848, https://doi.org/10.1029/2019MS001848, 2020.
- Holloway, G., Dupont, F., Golubeva, E., Häkkinen, S., Hunke, E., Jin, M., Karcher, M., Kauker, F., Maltrud, M., Morales Maqueda, M. A., Maslowski, W., Platov, G., Stark, D., Steele, M., Suzuki, T., Wang, J., and Zhang, J.: Water properties and circulation in Arctic Ocean models, J. Geophys. Res., 112, 2006JC003642, https://doi.org/10.1029/2006JC003642, 2007.
- Huang, B., Liu, C., Banzon, V., Freeman, E., Graham, G., Hankins, B., Smith, T., and Zhang, H.-M.: Improvements of the Daily Optimum Interpolation Sea Surface Temperature (DOISST) Version 2.1, Journal of Climate, 34, 2923–2939, https://doi.org/10.1175/JCLI-D-20-0166.1, 2021.
- Huo, Y., Wang, H., Veneziani, M., Comeau, D., Osinski, R., Hillman, B. R., Roesler, E. L., Maslowski, W., Rasch, P. J., Weijer, W., Baxter, I., Fu, Q., Garuba, O. A., Ma, W., Seefeldt, M. W., Sweeney, A. J., Wu, M., Zhang, J., Zhang, X., Zhang, Y., Asay-Davis, X. S., Craig, A., Lee, Y. J., and Zhang, S.: E3SM-Arctic: Regionally Refined Coupled Model for Advanced Understanding of Arctic Systems Interactions, https://doi.org/10.22541/essoar.172745745.54113167/v1, 27
- 1270 September 2024.
 - Ilicak, M., Drange, H., Wang, Q., Gerdes, R., Aksenov, Y., Bailey, D., Bentsen, M., Biastoch, A., Bozec, A., Böning, C., Cassou, C., Chassignet, E., Coward, A. C., Curry, B., Danabasoglu, G., Danilov, S., Fernandez, E., Fogli, P. G., Fujii, Y., Griffies, S. M., Iovino, D., Jahn, A., Jung, T., Large, W. G., Lee, C., Lique, C., Lu, J., Masina, S., George Nurser, A. J., Roth, C., Salas Y Mélia, D., Samuels, B. L., Spence, P., Tsujino, H., Valcke, S., Voldoire, A., Wang, X., and Yeager, S. G.:
- An assessment of the Arctic Ocean in a suite of interannual CORE-II simulations. Part III: Hydrography and fluxes, Ocean Modelling, 100, 141–161, https://doi.org/10.1016/j.ocemod.2016.02.004, 2016.
 - Karami, M. P., Myers, P. G., De Vernal, A., Tremblay, L. B., and Hu, X.: The role of Arctic gateways on sea ice and circulation in the Arctic and North Atlantic Oceans: a sensitivity study with an ocean-sea-ice model, Clim Dyn, 57, 2129–2151, https://doi.org/10.1007/s00382-021-05798-6, 2021.
- 1280 Karlsson, K.-G., Riihelä, A., Trentmann, J., Stengel, M., Solodovnik, I., Meirink, J. F., Devasthale, A., Jääskeläinen, E., Kallio-Myers, V., Eliasson, S., Benas, N., Johansson, E., Stein, D., Finkensieper, S., Håkansson, N., Akkermans, T., Clerbaux, N., Selbach, N., Marc, S., and Hollmann, R.: CLARA-A3: CM SAF cLoud, Albedo and surface RAdiation dataset from AVHRR data Edition 3 (3.0), https://doi.org/10.5676/EUM_SAF_CM/CLARA_AVHRR/V003, 2023.
- Karpouzoglou, T., De Steur, L., Smedsrud, L. H., and Sumata, H.: Observed Changes in the Arctic Freshwater Outflow in Fram Strait, JGR Oceans, 127, e2021JC018122, https://doi.org/10.1029/2021JC018122, 2022.
 - Kelly, S. J., Proshutinsky, A., Popova, E. K., Aksenov, Y. K., and Yool, A.: On the Origin of Water Masses in the Beaufort Gyre, JGR Oceans, 124, 4696–4709, https://doi.org/10.1029/2019JC015022, 2019.
- Khosravi, N., Wang, Q., Koldunov, N., Hinrichs, C., Semmler, T., Danilov, S., and Jung, T.: The Arctic Ocean in CMIP6 Models: Biases and Projected Changes in Temperature and Salinity, Earth's Future, 10, e2021EF002282, https://doi.org/10.1029/2021EF002282, 2022.
 - Kwok, R.: Arctic sea ice thickness, volume, and multiyear ice coverage: losses and coupled variability (1958–2018), Environ. Res. Lett., 13, 105005, https://doi.org/10.1088/1748-9326/aae3ec, 2018.

- Landrum, L. and Holland, M. M.: Extremes become routine in an emerging new Arctic, Nat. Clim. Chang., 10, 1108–1115, https://doi.org/10.1038/s41558-020-0892-z, 2020.
- Large, W. G., McWilliams, J. C., and Doney, S. C.: Oceanic vertical mixing: A review and a model with a nonlocal boundary layer parameterization, Reviews of Geophysics, 32, 363–403, https://doi.org/10.1029/94RG01872, 1994.
 - Laxon, S. W., Giles, K. A., Ridout, A. L., Wingham, D. J., Willatt, R., Cullen, R., Kwok, R., Schweiger, A., Zhang, J., Haas, C., Hendricks, S., Krishfield, R., Kurtz, N., Farrell, S., and Davidson, M.: CryoSat-2 estimates of Arctic sea ice thickness and volume, Geophysical Research Letters, 40, 732–737, https://doi.org/10.1002/grl.50193, 2013.
- Liang, X. and Losch, M.: On the Effects of Increased Vertical Mixing on the Arctic Ocean and Sea Ice, JGR Oceans, 123, 9266–9282, https://doi.org/10.1029/2018JC014303, 2018.
 - Lind, S., Ingvaldsen, R. B., and Furevik, T.: Arctic warming hotspot in the northern Barents Sea linked to declining sea-ice import, Nature Clim Change, 8, 634–639, https://doi.org/10.1038/s41558-018-0205-y, 2018.
- Lipscomb, W. H. and Ringler, T. D.: An Incremental Remapping Transport Scheme on a Spherical Geodesic Grid, Monthly Weather Review, 133, 2335–2350, https://doi.org/10.1175/MWR2983.1, 2005.
 - Liu, W., Liu, Y., and Zhao, S.: Global mode simulation results comparison between icosahedron spherical mesh and latitude-longitude mesh in China, Journal of Nanjing University of Information Science and Technology: Natural Science Edition, 8, 146–151, https://doi.org/10.13878/j.cnki.jnuist.2016.02.006, 2016.
- Locarnini, R. A., Mishonov, A. V., Baranova, O. K., Reagan, J. R., Boyer, T. P., Seidov, D., Wang, Z., Garcia, H. E., Bouchard, C., Cross, S. L., Paver, C. R., and Dukhovskoy, D.: World Ocean Atlas 2023, Volume 1: Temperature, https://doi.org/10.25923/54BH-1613, 2024.
 - Long, Z., Perrie, W., Zhang, M., and Liu, Y.: Responses of Atlantic Water Inflow Through Fram Strait to Arctic Storms, Geophysical Research Letters, 51, e2023GL107777, https://doi.org/10.1029/2023GL107777, 2024.
 - Lv, X. (2025). E3SMv2-MPAS. Zenodo. https://doi.org/10.5281/zenodo.15493256
- Meier, W., Fetterer, F., Windnagel, A., and Stewart, S.: NOAA/NSIDC Climate Data Record of Passive Microwave Sea Ice Concentration, Version 4, https://doi.org/10.7265/EFMZ-2T65, 2021.
 - Melnichenko, O., Hacker, P., Maximenko, N., Lagerloef, G., and Potemra, J.: Optimum interpolation analysis of A quarius sea surface salinity, JGR Oceans, 121, 602–616, https://doi.org/10.1002/2015JC011343, 2016.
- Meyer, A., Fer, I., Sundfjord, A., and Peterson, A. K.: Mixing rates and vertical heat fluxes north of Svalbard from Arctic winter to spring, Journal of Geophysical Research: Oceans, 122, 4569–4586, https://doi.org/10.1002/2016JC012441, 2017.
 - Muilwijk, M., Nummelin, A., Heuzé, C., Polyakov, I. V., Zanowski, H., and Smedsrud, L. H.: Divergence in Climate Model Projections of Future Arctic Atlantification, Journal of Climate, 36, 1727–1748, https://doi.org/10.1175/JCLI-D-22-0349.1, 2023.
- Onarheim, I. H., Eldevik, T., Smedsrud, L. H., and Stroeve, J. C.: Seasonal and Regional Manifestation of Arctic Sea Ice Loss, J. Climate, 31, 4917–4932, https://doi.org/10.1175/JCLI-D-17-0427.1, 2018.

- Pan, R., Shu, Q., Wang, Q., Wang, S., Song, Z., He, Y., and Qiao, F.: Future Arctic Climate Change in CMIP6 Strikingly Intensified by NEMO-Family Climate Models, Geophysical Research Letters, 50, e2022GL102077, https://doi.org/10.1029/2022GL102077, 2023.
- Peralta-Ferriz, C. and Woodgate, R. A.: Seasonal and interannual variability of pan-Arctic surface mixed layer properties from 1979 to 2012 from hydrographic data, and the dominance of stratification for multiyear mixed layer depth shoaling, Progress in Oceanography, 134, 19–53, https://doi.org/10.1016/j.pocean.2014.12.005, 2015.
- Petersen, M. R., Asay-Davis, X. S., Berres, A. S., Chen, Q., Feige, N., Hoffman, M. J., Jacobsen, D. W., Jones, P. W., Maltrud, M. E., Price, S. F., Ringler, T. D., Streletz, G. J., Turner, A. K., Van Roekel, L. P., Veneziani, M., Wolfe, J. D., Wolfram, P. J., and Woodring, J. L.: An Evaluation of the Ocean and Sea Ice Climate of E3SM Using MPAS and Interannual CORE-II Forcing, J Adv Model Earth Syst, 11, 1438–1458, https://doi.org/10.1029/2018MS001373, 2019.
 - Pnyushkov, A. V., Polyakov, I. V., Alekseev, G. V., Ashik, I. M., Baumann, T. M., Carmack, E. C., Ivanov, V. V., and Rember, R.: A Steady Regime of Volume and Heat Transports in the Eastern Arctic Ocean in the Early 21st Century, Front. Mar. Sci., 8, 705608, https://doi.org/10.3389/fmars.2021.705608, 2021.
- Polyakov, I. V., Beszczynska, A., Carmack, E. C., Dmitrenko, I. A., Fahrbach, E., Frolov, I. E., Gerdes, R., Hansen, E., Holfort, J., Ivanov, V. V., Johnson, M. A., Karcher, M., Kauker, F., Morison, J., Orvik, K. A., Schauer, U., Simmons, H. L., Skagseth, Ø., Sokolov, V. T., Steele, M., Timokhov, L. A., Walsh, D., and Walsh, J. E.: One more step toward a warmer Arctic, Geophysical Research Letters, 32, 2005GL023740, https://doi.org/10.1029/2005GL023740, 2005.
- Polyakov, I. V., Timokhov, L. A., Alexeev, V. A., Bacon, S., Dmitrenko, I. A., Fortier, L., Frolov, I. E., Gascard, J.-C., Hansen, E., Ivanov, V. V., Laxon, S., Mauritzen, C., Perovich, D., Shimada, K., Simmons, H. L., Sokolov, V. T., Steele, M., and Toole, J.: Arctic Ocean Warming Contributes to Reduced Polar Ice Cap, Journal of Physical Oceanography, 40, 2743–2756, https://doi.org/10.1175/2010JPO4339.1, 2010.
 - Polyakov, I. V., Bhatt, U. S., Walsh, J. E., Abrahamsen, E. P., Pnyushkov, A. V., and Wassmann, P. F.: Recent oceanic changes in the Arctic in the context of long-term observations, Ecological Applications, 23, 1745–1764, https://doi.org/10.1890/11-0902.1, 2013.
- Polyakov, I. V., Pnyushkov, A. V., Alkire, M. B., Ashik, I. M., Baumann, T. M., Carmack, E. C., Goszczko, I., Guthrie, J., Ivanov, V. V., Kanzow, T., Krishfield, R., Kwok, R., Sundfjord, A., Morison, J., Rember, R., and Yulin, A.: Greater role for Atlantic inflows on sea-ice loss in the Eurasian Basin of the Arctic Ocean, Science, 356, 285–291, https://doi.org/10.1126/science.aai8204, 2017.
- Polyakov, I. V., Alkire, M. B., Bluhm, B. A., Brown, K. A., Carmack, E. C., Chierici, M., Danielson, S. L., Ellingsen, I., 1355 Ershova, E. A., Gårdfeldt, K., Ingvaldsen, R. B., Pnyushkov, A. V., Slagstad, D., and Wassmann, P.: Borealization of the Arctic Ocean in Response to Anomalous Advection From Sub-Arctic Seas, Front. Mar. Sci., 7, 491, https://doi.org/10.3389/fmars.2020.00491, 2020a.
- Polyakov, I. V., Rippeth, T. P., Fer, I., Alkire, M. B., Baumann, T. M., Carmack, E. C., Ingvaldsen, R., Ivanov, V. V., Janout, M., Lind, S., Padman, L., Pnyushkov, A. V., and Rember, R.: Weakening of Cold Halocline Layer Exposes Sea Ice to Oceanic Heat in the Eastern Arctic Ocean, Journal of Climate, 33, 8107–8123, https://doi.org/10.1175/JCLI-D-19-0976.1, 2020b.
 - Polyakov, I. V., Mayer, M., Tietsche, S., and Karpechko, A. Yu.: Climate Change Fosters Competing Effects of Dynamics and Thermodynamics in Seasonal Predictability of Arctic Sea Ice, Journal of Climate, 35, 2849–2865, https://doi.org/10.1175/JCLI-D-21-0463.1, 2022.

- Polyakov, I. V., Pnyushkov, A. V., Charette, M., Cho, K.-H., Jung, J., Kipp, L., Muilwijk, M., Whitmore, L., Yang, E. J., and Yoo, J.: Atlantification advances into the Amerasian Basin of the Arctic Ocean, Science AdvAnceS, 2025.
- Proshutinsky, A., Krishfield, R., Toole, J. M., Timmermans, M. -L., Williams, W., Zimmermann, S., Yamamoto-Kawai, M., Armitage, T. W. K., Dukhovskoy, D., Golubeva, E., Manucharyan, G. E., Platov, G., Watanabe, E., Kikuchi, T., Nishino, S., Itoh, M., Kang, S. -H., Cho, K. -H., Tateyama, K., and Zhao, J.: Analysis of the Beaufort Gyre Freshwater Content in 2003–2018, JGR Oceans, 124, 9658–9689, https://doi.org/10.1029/2019JC015281, 2019.
 - Rantanen, M., Karpechko, A. Yu., Lipponen, A., Nordling, K., Hyvärinen, O., Ruosteenoja, K., Vihma, T., and Laaksonen, A.: The Arctic has warmed nearly four times faster than the globe since 1979, Commun Earth Environ, 3, 168, https://doi.org/10.1038/s43247-022-00498-3, 2022.
- Rayner, N. A., Parker, D. E., Horton, E. B., Folland, C. K., Alexander, L. V., Rowell, D. P., Kent, E. C., and Kaplan, A.: Global analyses of sea surface temperature, sea ice, and night marine air temperature since the late nineteenth century, J. Geophys. Res., 108, 2002JD002670, https://doi.org/10.1029/2002JD002670, 2003.
 - Reagan, J. R., Seidov, D., Wang, Z., Dukhovskoy, D., Boyer, T. P., Locarnini, R. A., Baranova, O. K., Mishonov, A. V., Garcia, H. E., Bouchard, C., Cross, S. L., and Paver, C. R.: World Ocean Atlas 2023, Volume 2: Salinity, https://doi.org/10.25923/70QT-9574, 2024.
- Richards, A. E., Johnson, H. L., and Lique, C.: Spatial and Temporal Variability of Atlantic Water in the Arctic From 40 Years of Observations, JGR Oceans, 127, e2021JC018358, https://doi.org/10.1029/2021JC018358, 2022.
 - Ricker, R., Hendricks, S., Kaleschke, L., Tian-Kunze, X., King, J., and Haas, C.: A weekly Arctic sea-ice thickness data record from merged CryoSat-2 and SMOS satellite data, The Cryosphere, 11, 1607–1623, https://doi.org/10.5194/tc-11-1607-2017, 2017.
- Rieke, O., Årthun, M., and Dörr, J. S.: Rapid sea ice changes in the future Barents Sea, The Cryosphere, 17, 1445–1456, https://doi.org/10.5194/tc-17-1445-2023, 2023.
 - Ringler, T., Petersen, M., Higdon, R. L., Jacobsen, D., Jones, P. W., and Maltrud, M.: A multi-resolution approach to global ocean modeling, Ocean Modelling, 69, 211–232, https://doi.org/10.1016/j.ocemod.2013.04.010, 2013.
- Schauer, U., Fahrbach, E., Osterhus, S., and Rohardt, G.: Arctic warming through the Fram Strait: Oceanic heat transport from 3 years of measurements, J. Geophys. Res., 109, 2003JC001823, https://doi.org/10.1029/2003JC001823, 2004.
 - Schauer, U., Beszczynska-Möller, A., Walczowski, W., Fahrbach, E., Piechura, J., and Hansen, E.: Variation of Measured Heat Flow Through the Fram Strait Between 1997 and 2006, in: Arctic-Subarctic Ocean Fluxes: Defining the Role of the Northern Seas in Climate, edited by: Dickson, R. R., Meincke, J., and Rhines, P., Springer Netherlands, Dordrecht, 65–85, https://doi.org/10.1007/978-1-4020-6774-7 4, 2008.
- Scholz, P., Sidorenko, D., Gurses, O., Danilov, S., Koldunov, N., Wang, Q., Sein, D., Smolentseva, M., Rakowsky, N., and Jung, T.: Assessment of the Finite-volumE Sea ice-Ocean Model (FESOM2.0) Part 1: Description of selected key model elements and comparison to its predecessor version, Geosci. Model Dev., 12, 4875–4899, https://doi.org/10.5194/gmd-12-4875-2019, 2019.
- Schweiger, A., Lindsay, R., Zhang, J., Steele, M., Stern, H., and Kwok, R.: Uncertainty in modeled Arctic sea ice volume, J. Geophys. Res., 116, C00D06, https://doi.org/10.1029/2011JC007084, 2011.

- Schweiger, A. J., Wood, K. R., and Zhang, J.: Arctic Sea Ice Volume Variability over 1901–2010: A Model-Based Reconstruction, Journal of Climate, 32, 4731–4752, https://doi.org/10.1175/JCLI-D-19-0008.1, 2019.
- Shu, Q., Wang, Q., Su, J., Li, X., and Qiao, F.: Assessment of the Atlantic water layer in the Arctic Ocean in CMIP5 climate models, Clim Dyn, 53, 5279–5291, https://doi.org/10.1007/s00382-019-04870-6, 2019.
- Shu, Q., Wang, Q., Årthun, M., Wang, S., Song, Z., Zhang, M., and Qiao, F.: Arctic Ocean Amplification in a warming climate in CMIP6 models, Sci. Adv., 8, eabn9755, https://doi.org/10.1126/sciadv.abn9755, 2022.
 - Smedsrud, L. H., Esau, I., Ingvaldsen, R. B., Eldevik, T., Haugan, P. M., Li, C., Lien, V. S., Olsen, A., Omar, A. M., Otterå, O. H., Risebrobakken, B., Sandø, A. B., Semenov, V. A., and Sorokina, S. A.: THE ROLE OF THE BARENTS SEA IN THE ARCTIC CLIMATE SYSTEM, Reviews of Geophysics, 51, 415–449, https://doi.org/10.1002/rog.20017, 2013.
- Steele, M. and Boyd, T.: Retreat of the cold halocline layer in the Arctic Ocean, J. Geophys. Res., 103, 10419–10435, https://doi.org/10.1029/98JC00580, 1998.
 - Steele, M., Morley, R., and Ermold, W.: PHC: A Global Ocean Hydrography with a High-Quality Arctic Ocean, J. Climate, 14, 2079–2087, https://doi.org/10.1175/1520-0442(2001)014<2079:PAGOHW>2.0.CO;2, 2001.
- Stroeve, J., Barrett, A., Serreze, M., and Schweiger, A.: Using records from submarine, aircraft and satellites to evaluate climate model simulations of Arctic sea ice thickness, The Cryosphere, 8, 1839–1854, https://doi.org/10.5194/tc-8-1839-2014, 2014.
 - Tsubouchi, T., Von Appen, W.-J., Kanzow, T., and De Steur, L.: Temporal Variability of the Overtuming Circulation in the Arctic Ocean and the Associated Heat and Freshwater Transports during 2004–10, Journal of Physical Oceanography, 54, 81–94, https://doi.org/10.1175/JPO-D-23-0056.1, 2024.
- Tsujino, H., Urakawa, S., Nakano, H., Small, R. J., Kim, W. M., Yeager, S. G., Danabasoglu, G., Suzuki, T., Bamber, J. L., Bentsen, M., Böning, C. W., Bozec, A., Chassignet, E. P., Curchitser, E., Boeira Dias, F., Durack, P. J., Griffies, S. M., Harada, Y., Ilicak, M., Josey, S. A., Kobayashi, C., Kobayashi, S., Komuro, Y., Large, W. G., Le Sommer, J., Marsland, S. J., Masina, S., Scheinert, M., Tomita, H., Valdivieso, M., and Yamazaki, D.: JRA-55 based surface dataset for driving ocean–sea-ice models (JRA55-do), Ocean Modelling, 130, 79–139, https://doi.org/10.1016/j.ocemod.2018.07.002, 2018.
- Turner, A. K., Lipscomb, W. H., Hunke, E. C., Jacobsen, D. W., Jeffery, N., Engwirda, D., Ringler, T. D., and Wolfe, J. D.: MPAS-Seaice (v1.0.0): sea-ice dynamics on unstructured Voronoi meshes, Geosci. Model Dev., 15, 3721–3751, https://doi.org/10.5194/gmd-15-3721-2022, 2022.
 - Turner, J. S.: The Melting of Ice in the Arctic Ocean: The Influence of Double-Diffusive Transport of Heat from Below, Journal of Physical Oceanography, 40, 249–256, https://doi.org/10.1175/2009JPO4279.1, 2010.
- Veneziani, M., Maslowski, W., Lee, Y. J., D'Angelo, G., Osinski, R., Petersen, M. R., Weijer, W., Craig, A. P., Wolfe, J. D., Comeau, D., and Turner, A. K.: An evaluation of the E3SMv1 Arctic ocean and sea-ice regionally refined model, Geosci. Model Dev., 15, 3133–3160, https://doi.org/10.5194/gmd-15-3133-2022, 2022.
 - Von Schuckmann, K., Cheng, L., Palmer, M. D., Hansen, J., Tassone, C., Aich, V., Adusumilli, S., Beltrami, H., Boyer, T., Cuesta-Valero, F. J., Desbruyères, D., Domingues, C., García-García, A., Gentine, P., Gilson, J., Gorfer, M., Haimberger, L.,
- Ishii, M., Johnson, G. C., Killick, R., King, B. A., Kirchengast, G., Kolodziejczyk, N., Lyman, J., Marzeion, B., Mayer, M., Monier, M., Monselesan, D. P., Purkey, S., Roemmich, D., Schweiger, A., Seneviratne, S. I., Shepherd, A., Slater, D. A., Steiner, A. K., Straneo, F., Timmermans, M.-L., and Wijffels, S. E.: Heat stored in the Earth system: where does the energy go?, Earth Syst. Sci. Data, 12, 2013–2041, https://doi.org/10.5194/essd-12-2013-2020, 2020.

- Wang, Q., Wekerle, C., Danilov, S., Wang, X., and Jung, T.: A 4.5 km resolution Arctic Ocean simulation with the global multi-resolution model FESOM 1.4, Geosci. Model Dev., 11, 1229–1255, https://doi.org/10.5194/gmd-11-1229-2018, 2018.
 - Wang, Q., Wekerle, C., Danilov, S., Sidorenko, D., Koldunov, N., Sein, D., Rabe, B., and Jung, T.: Recent Sea Ice Decline Did Not Significantly Increase the Total Liquid Freshwater Content of the Arctic Ocean, Journal of Climate, 32, 15–32, https://doi.org/10.1175/JCLI-D-18-0237.1, 2019.
- Wang, Q., Shu, Q., Danilov, S., and Sidorenko, D.: An extreme event of enhanced Arctic Ocean export west of Greenland caused by the pronounced dynamic sea level drop in the North Atlantic subpolar gyre in the mid-to-late 2010s, Environ. Res. Lett., 17, 044046, https://doi.org/10.1088/1748-9326/ac5562, 2022.
- Wang, Q., Shu, Q., Wang, S., Beszczynska-Moeller, A., Danilov, S., Steur, L., Haine, T. W. N., Karcher, M., Lee, C. M., Myers, P. G., Polyakov, I. V., Provost, C., Skagseth, Ø., Spreen, G., and Woodgate, R.: A Review of Arctic–Subarctic Ocean Linkages: Past Changes, Mechanisms, and Future Projections, Ocean-Land-Atmos Res, 2, 0013, https://doi.org/10.34133/olar.0013, 2023.
 - Wang, Q., Shu, Q., Bozec, A., Chassignet, E. P., Fogli, P. G., Fox-Kemper, B., Hogg, A. McC., Iovino, D., Kiss, A. E., Koldunov, N., Le Sommer, J., Li, Y., Lin, P., Liu, H., Polyakov, I., Scholz, P., Sidorenko, D., Wang, S., and Xu, X.: Impact of increased resolution on Arctic Ocean simulations in Ocean Model Intercomparison Project phase 2 (OMIP-2), Geosci. Model Dev., 17, 347–379, https://doi.org/10.5194/gmd-17-347-2024, 2024.
- Wassmann, P., Kosobokova, K. N., Slagstad, D., Drinkwater, K. F., Hopcroft, R. R., Moore, S. E., Ellingsen, I., Nelson, R. J., Carmack, E., Popova, E., and Berge, J.: The contiguous domains of Arctic Ocean advection: Trails of life and death, Progress in Oceanography, 139, 42–65, https://doi.org/10.1016/j.pocean.2015.06.011, 2015.
- Wekerle, C., Wang, Q., Danilov, S., Jung, T., and Schröter, J.: The Canadian Arctic Archipelago throughflow in a multiresolution global model: Model assessment and the driving mechanism of interannual variability, JGR Oceans, 118, 4525–4541, https://doi.org/10.1002/jgrc.20330, 2013.
 - Woodgate, R. A.: Increases in the Pacific inflow to the Arctic from 1990 to 2015, and insights into seasonal trends and driving mechanisms from year-round Bering Strait mooring data, Progress in Oceanography, 160, 124–154, https://doi.org/10.1016/j.pocean.2017.12.007, 2018.
- Woodgate, R. A. and Peralta-Ferriz, C.: Warming and Freshening of the Pacific Inflow to the Arctic From 1990-2019 Implying Dramatic Shoaling in Pacific Winter Water Ventilation of the Arctic Water Column, Geophysical Research Letters, 48, e2021GL092528, https://doi.org/10.1029/2021GL092528, 2021.
 - Zhang, J. and Rothrock, D. A.: Modeling Global Sea Ice with a Thickness and Enthalpy Distribution Model in Generalized Curvilinear Coordinates, Mon. Wea. Rev., 131, 845–861, https://doi.org/10.1175/1520-0493(2003)131<0845:MGSIWA>2.0.CO;2, 2003.
- Zhang, Y., Chen, C., Beardsley, R. C., Gao, G., Qi, J., and Lin, H.: Seasonal and interannual variability of the Arctic sea ice: A comparison between AO-FVCOM and observations: NUMERICAL STUDY ON THE ARCTIC SEA ICE, J. Geophys. Res. Oceans, 121, 8320–8350, https://doi.org/10.1002/2016JC011841, 2016.
- Zhu, Y., Zhang, R.-H., Moum, J. N., Wang, F., Li, X., and Li, D.: Physics-informed deep-learning parameterization of ocean vertical mixing improves climate simulations, National Science Review, 9, nwac044, https://doi.org/10.1093/nsr/nwac044, 2022.

Zuo, H., Balmaseda, M. A., Tietsche, S., Mogensen, K., and Mayer, M.: The ECMWF operational ensemble reanalysis-analysis system for ocean and sea-ice: a description of the system and assessment, https://doi.org/10.5194/os-2018-154, 8 January 2019.